Master's Thesis

Hierarchical Porous Metal-Organic Frameworks *via* Solvent Assisted Interpenetration and Linker Extraction

Jeongin Park

Department of Molecular Sciences

Graduate School of UNIST

2016

Hierarchical Porous Metal-Organic Frameworks *via* Solvent Assisted Interpenetration and Linker Extraction

Jeongin Park

Department of Molecular Sciences
Graduate School of UNIST

Hierarchical Porous Metal-Organic Frameworks *via* Solvent Assisted Interpenetration and Linker Extraction

A thesis/dissertation
submitted to the Graduate School of UNIST
in partial fulfillment of the
requirements for the degree of
Master of Science

Jeongin Park

02/ 23/ 2016
Approved by

_____

Advisor
Myoung-soo Lah

Hierarchical Porous Metal-Organic Frameworks *via* Solvent Assisted Interpenetration and Linker Extraction

Jeongin Park

This certifies that the thesis/dissertation of Jeongin Park is approved.

02/ 23/ 2016

Signature

_____

Advisor: Myoung soo Lah

Signature

_____

Hoi ri Moon

Signature

_____

Wonyoung Choe

Abstract

Two different pillaring linkers, 4,4'- azopyridine (azopy) and bis(4-pyridyl) acetylene (bpa), were introduced to two dimensional sheets of [Ni(HBTC)$(DMF)_2$] (where H_3BTC = benzene-1,3,5-tricarboxylic acid and DMF = *N*,*N*-dimethylformamide) to form two isoreticular hms topological MOFs. Azopy was used to improve CO2 capturing ability since the interaction between the azo group and CO_2 molecules had a potential for the amount of CO_2 uptake. Bpa was selected to increase the stability of the structure due to the rigid alkyne group in the linker. Although **bpa-hms** [Ni(HBTC)(bpa)] had a larger porosity, **azo-hms** [Ni(HBTC)(azopy)] had a greater CO_2 adsorption amount at the room temperature because of the amino group, interacting with CO_2.

For the pore size control, the **hms** structures were heated so to form interpenetrated structures (**hms-c**). Under the solvent-assisted environment, the neutral ligands were easily detached and then attached to the sheets. It was the first time to demonstrate the interpenetration in the complicated topology, besides **pcu**-net, through the post-synthetic heat treatment. After the interpenetration, thereby it was possible to tune the pore size, and enhance the stability of the frameworks. The reduced pore size also increased the interaction between the guest molecules and the frameworks.

Meanwhile, to compensate the extremely reduced porosity of interpenetrated MOFs, the defect-engineering strategy was implemented. The neutral pillars in **hms** MOFs were able to be removed systematically under the thermal vacuum condition. The vacant sites formed the mesopores, and they deserved additional porosity. They can be utilized as active sites for chemical reactions and accelerating the mass transportation of guest molecules. Therefore, these hierarchical interpenetrated MOFs (**hms-d**) may be effectively applied to catalytic performance.

Contents

List of Figures

Figure 3-21. (a) Sorption behavior of **azo-hms-d**; (b) Pore size distribution of **azo-hms-d.**

Figure 3-22. (a) Sorption behavior of **bpa-hms-d**; (b) Pore size distribution of **bpa-hms-d.**

Figure S1. $V_m(P-P_0)$ vs P/P_0 for hms-MOFs. Only the range below dot point of P/P_0 in respective graphs satisfies the first consistency criterion for applying the BET theory. (Left) And the comparison of $P/(V_m(1-(P-P_0))$ calculated from the standard range, BET linear fit calculated from the range identified through the consistency criteria. (Right); (a) **azo-hms**; (b) **bpa-hms**; (c) **azo-hms-c**; (d) **bpa-hms-c**.

Figure S2. The virial-type expression of experimental CO_2 pressure in hms-MOFs at 0 ºC and 25 ºC, and corresponding virial fitting. (a) **azo-hms**; (b) **bpa-hms**; (c) **azo-hms-c**; (d) **bpa-hms-c.**

Figure S3. (a-c) ^{1}H NMR spectra of crystals digested in DCl/D_2O. The ratios of resident linker azopy and BTC in the resulting extraction of neutral linkers are determined using the integrations of the peaks; (a) **azo-hms-d1**; (b) **azo-hms-d3**; (c) **azo-hms-d24**; (d) The plot demonstrates the increasing incorporation of fragment into the crystals as aging time is increased under the thermal vacuum condition.

Figure S4. (a-e) ^{1}H NMR spectra of crystals digested in DCl/DMSO-d_6. The ratios of resident linker bpa and BTC in the resulting extraction of neutral linkers are determined using the integrations of the peaks; (a) **bpa-hms-d1**; (b) **bpa-hms-d2**; (c) **bpa-hms-d3**; (d) **bpa-hms-d9**; (e) **bpa-hms-d24**; (f) The plot demonstrates the increasing incorporation of fragment into the crystals as aging time is increased under the thermal vacuum condition.

Figure S5. Experimental N_2 adsorption data in **azo-hms-d** at 77 K, and corresponding NLDFT theoretical isotherms fits in pore of different diameters depending on the aging time under the thermal vacuum condition; (a) **azo-hms-c**; (b) **azo-hms-d1**; (c) **azo-hms-d3**; (d) **azo-hms-d24.**

Figure S6. Experimental N_2 adsorption data in **bpa-hms-d** at 77 K, and corresponding NLDFT theoretical isotherms fits in pore of different diameters depending on the aging time under the thermal vacuum condition; (a) **bpa-hms-c**; (b) **bpa-hms-d3**; (c) **bpa-hms-d9**; (d) **bpa-hms-d24**.

List of Tables

Nomenclatures

MOF	Metal-Organic Framework
SBU	Secondary Building Unit
PSM	Post-Synthetic Modification
CUS	Coordinatively Unsaturated Site
DEMOF	Defect Engineered Metal-Organic Framework
BTC	Benzene 1,3,5-tricarboxylic acid
azo, azopy	4,4'-azopyridine
bpa	bis(4-pyridyl) acetylene
bipy	4,4'-bipyridine
EtOH	Ethyl Alcohol
PXRD	Powder X-Ray Diffraction
VT-PXRD	Variable Temperature Powder X-Ray Diffraction
TGA	Thermogravimetric analysis
NMR	Nuclear Mass Resolution
EA	Elemental Analysis
IR	Infrared
BET	Brauner-Emmett-Teller
DMF	*N*,*N*-Dimethyl Formamide
DEF	*N*,*N*-Diethyl Formamide
MC	Methylene Chloride
hms-c	Catenated **hms** structure
hms-d	Defect engineered interpenetrated **hms** structure
N_2	Nitrogen

CO_2	Carbon dioxide
NLDFT	Nonlocal Density Functional Theory
DCl	Deuterium Chloride
DMSO	Dimethyl Sulfoxide
PSD	Pore Size Distribution

I. Introduction

Recently, porous solids are of scientific and technological interest because of their exceptionally large surface areas [1] and ability to interact with atom, ions and molecules. They are extremely high impact on industrial applications as adsorbents (for separation and storage), ion exchangers, drug delivery and catalysts.[2] The number of these benefits from the high order that can be achieved in solids such as purely inorganic zeolites, purely organic porous polymers, and organic inorganic hybrid, metal-organic frameworks (MOFs) (Figure 1-1). In addition, the distribution of sizes, shapes and volumes of the void spaces in porous materials directly relates to their ability to perform the desired function in a particular application. Therefore, the need to create uniformity within the pore size, shape and volume has steadily increased over recent year because it can lead to superior applications properties.

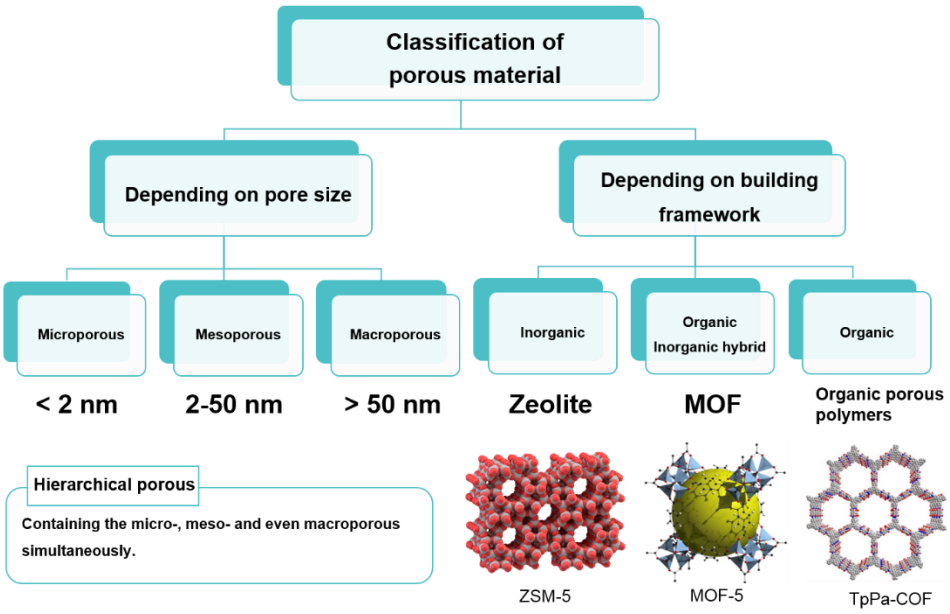

Figure 1-1. Classification of porous materials depending on pore size and building framework.[3]

The pores of solids are classified according to size: pore sizes in the range of 2 nm and below are called micropores, those in the range of 2 nm to 50 nm are denoted mesopores, and those above 50 nm are macropores (Figure 1-1). Moreover, development of porous structures diversely by creating additional porosity, hierarchically structured porous materials containing both micro- and mesoporosity also rise. Tremendous efforts have been made to control the size of pores in porous materials, as the properties and functions of porous solids are significantly dictated by the size and shape of pores in them. For example, a material with uniform micropores, such as a zeolite, can separate molecules on the basis of their size by selectively adsorbing a small molecule from a mixture

containing molecules too large to enter its pores. Meanwhile in the case of microporous material, ETS-10, the role of pore size as well as pore shape affects the separation of molecules. As illustrated schematically in Figure 1-2, the pore shape of this material is crucial to discriminate between unsymmetrical N_2 and symmetrical CH_4. This principle, which has led to separation devices that are now commercially available, might be extendable to materials with larger pores and the separation of larger molecules.[4]

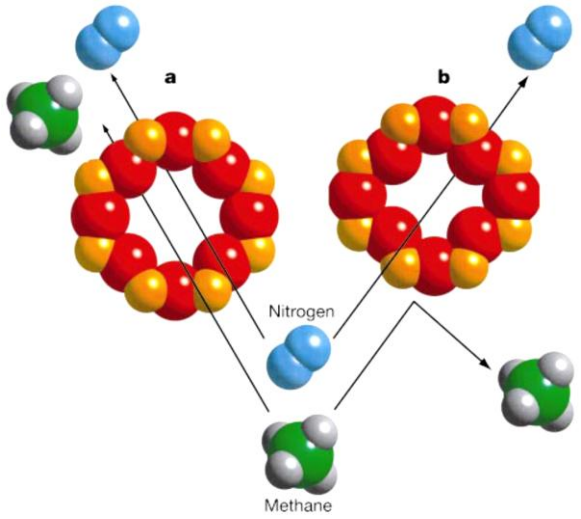

Figure 1-2. Pore size and shape of ETS-10.[4] **a**, Circular pore shape does not discriminate between nitrogen and methane. **b**, Elliptical shape of pore, obtained upon heat treatment, allows nitrogen adsorption only.

In 1988, the first crystalline microporous material with uniform pores larger than 1.0 nm reported[5] synthesizing well-ordered mesoporous materials.[6] Moreover, zeolites and later on zeotypes have been well known for more than 20 years, a remarkable boom in the preparation of new types of molecular sieves started at the beginning of 1990s.[7] Traditional microporous molecular sieves, such as zeolites Y, ZSM-5 have excellent properties related to intrinsic acidity and uniform micropores.[8] Also, Much synthetic effort has been devoted in several years in particular to the enlargement of the size of zeolite channels in order to allow larger molecules to reach the active sites. The increase in the accessibility of acid sites located inside the channel systems of zeolite-base molecular sieves would result in an increase in the number of reactions catalyzed by catalysts in fine chemical and petroleum refining However despite their promise for advanced materials applications, the claim of largest surface area of an ordered structure was that of zeolite Y, recorded at 904 m^2 g^{-1}.[9] That results in the difficult gas transport of reactants to the active sites in the channels or back-diffusion of products.[10] On the other hands, with the introduction of MOFs, this has been exceeded, with the range from 1000

to 10,000 m^2 g^{-1}. To date, MOFs with permanent porosity are more extensive in their variety and multiplicity than any other class of porous materials; zeolites and carbons (Figure 1-3).

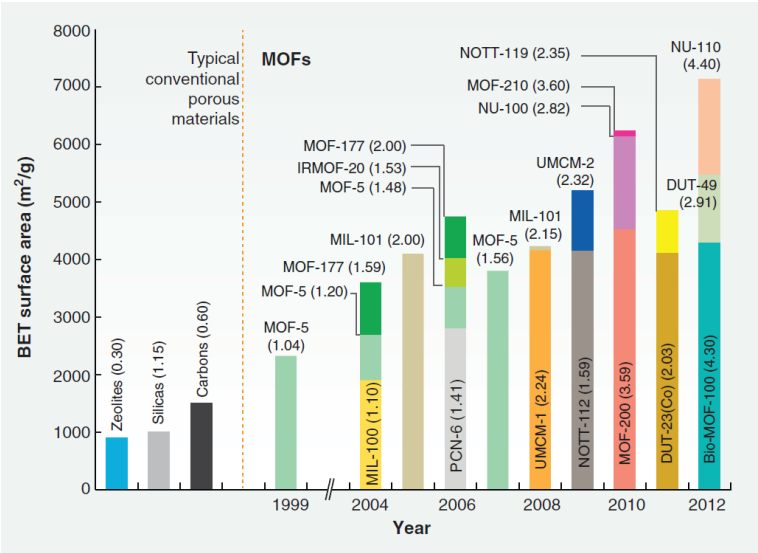

Figure 1-3. Progress in the synthesis of ultrahigh-porosity MOFs. BET surface areas of MOFs and typical conventional materials were estimated from gas adsorption measurements. The values in parentheses the pore volume (cm^3/g) of these materials.[11]

I.1. Porous MOFs

A different approach to preparing microporous solids involves the coordination of metal ions to organic linker, thus yielding framework structures. The frameworks comprising metal-organic units gained renewed interest in the 1990s, but the inability of theses solids to maintain permanent porosity and avoid structural rearrangements upon guest removal or guest exchange has been an obvious shortcoming which is leading to collapse of the framework. However, through improved scientific knowledge, MOFs that exhibit permanent porosity have now been prepared. [12]

MOFs generally constructed from metal ions / metal clusters (also known as secondary building units, or SBUs) and organic ligands. There are extraordinarily possible combinations of two components of MOFs, the organic linkers and inorganic components. Also, the MOF crystals are produced by a process of self-assembly, which allows for the spontaneous formation of ordered lattice under the proper conditions (Figure 1-4).[13] Due to their structural tunability and enormous internal surface area, the field of MOFs has become one of the fastest growing areas in chemistry. The ever-escalating number of structures, publications, and citations demonstrates the expansion of MOFs potential (Figure 1-5).[14]

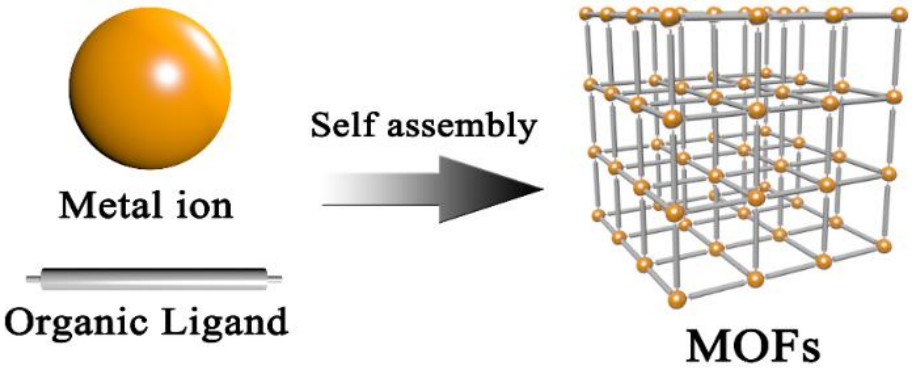

Figure 1-4. Scheme of MOFs.

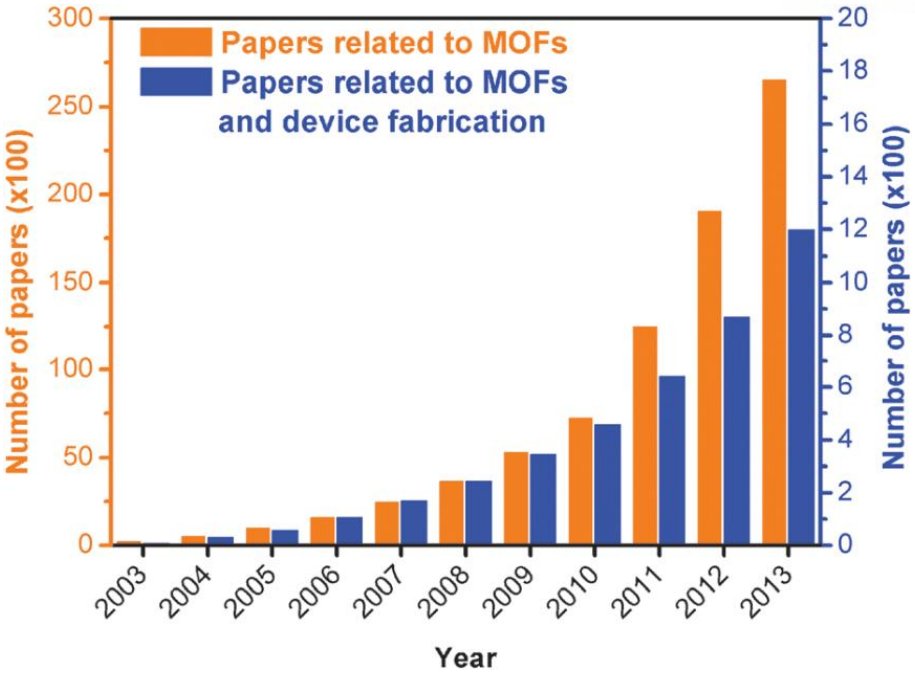

Figure 1-5. Evolution of the cumulative number of papers related to MOFs (orange), and to MOFs and device fabrication (blue), in 2003-2013 period. Source: ISI Web of Science.[14]

Porous MOFs are unlikely to compete with zeolites and other oxide-based porous materials in high-temperature applications owing to their limited long-term stability under such conditions and high cost. But the ability to prepare such solids, including frameworks with extra-large pores and high pore volumes, is nevertheless likely to open up many application possibilities. The functionalization of the organic component of the framework, or incorporation of functional organic groups directly into the framework, may yield porous solids that contain different groups capable of binding guests and/or catalyzing chemical reactions involving adsorbed guests.

Therefore, the MOFs have attracted a lot of attention from not only researchers but also others in different fields for potential applications because of their high surface area and tunable porosities (Table 1-1). The remarkable capabilities in green chemistry with the accessible surface area in the pores is a critical feature, such as in storage media[15] for gases, typically hydrogen and methane and the selective materials[16] as high-capacity adsorbents to satisfy versatile gas separation needs. Besides, the several applications have been proposed for catalytic reactions in organic and electrochemistry.[17] More recently, they have been shown the splendid potentials for various other applications, including sensing[18], pollutant sequestration[19], drug-delivery and release[20]

Table 1-1. Typical properties and applications of MOFs. MOFs exhibiting the lowest and highest values for the indicated property, and those reported first for selected applications, are shown.[1]

Property or application	Compound	Achieved value or year of report
Lowest reported value		
Density	MOF-399	0.126 g/cm^3
Highest reported value		
Pore aperture	IRMOF-74-XI	98 Å
Number of organic linkers	MTV-MOF-5	8
Degrees of interpenetration	$Ag_6(OH)_2(H_2O)_4(TIPA)_5$	54
BET surface area	NU-110	7140 m^2/g
Pore volume	NU-110	4.40 cm^3/g
Excess hydrogen uptake (77 K, 56 bar)	NU-100	9.0 wt%
Excess methane uptake (290 K, 35 bar)	PCN-14	212 mg/g
Excess carbon dioxide uptake (298 K, 50 bar)	MOF-200	2347 mg/g
Proton conductivity (98% relative humidity, 25°C)	$(NH_4)_2(ADP)[Zn_2(oxalate)_3]\cdot 3H_2O$	8×10^{-3} S/cm
Charge mobility	Zn_2(TTFTB)	0.2 cm^2/V·s
Lithium storage capacity (after 60 cycles)	$Zn_3(HCOO)_6$	560 mAh/g
Earliest report		
Catalysis by a MOF	$Cd(BPy)_2(NO_3)_2$	1994
Gas adsorption isotherm and permanent porosity	MOF-2	1998
Asymmetric catalysis with a homochiral MOF	POST-1	2000
Production of open metal site	MOF-11	2000
PSM on the organic linker	POST-1	2000
Use of a MOF for magnetic resonance imaging	MOF-73	2008

I. 1. 1 Tuning the structures via combination of starting building blocks

As mentioned earlier, in the porous MOFs, the size, shape, and arrangement of the porous crystals affect the properties and functions of crystals. Thus, in order to design a target structure, (i) the starting building blocks should have the relevant attributes necessary to assemble the skeleton of the desired structure; (ii) the synthesis must be adaptable to the use of derivatives of those building blocks to produce structures with various functionalities and dimensions. Based on understanding of starting building blocks; underlying nets of SBU and organic linker design, the size and shape pore in MOFs can be predictable. Overall, it is the combination of both SBUs and organic linkers that determines the final framework-topology.[21]

The successful utilization of underlying nets of SBUs in the formation of certain predicted structures and their impact on identifying networks with optimal porosity are evident. The symmetrical metal-cluster SBUs are shown and similarly abstracted as regular geometrical shapes formed by their points of extension. In MOFs, they are linked by organic linkers such as carboxylates and their shape is generally a polygon, polyhedron, or a rod. Representatively, a diamondoid net can be construct from 4-connected tetrahedral clusters and ditopic linear linkers, [22] and a cubic net can be formed from 6-connected octahedral clusters and ditopic linear linkers (Figure 1-6).[12a] Furthermore, based on the flexibility of design of organic SBUs, it is important to identify all the branching points (vertices) and individual links (edges) rather than just identifying the envelope (points of extension).

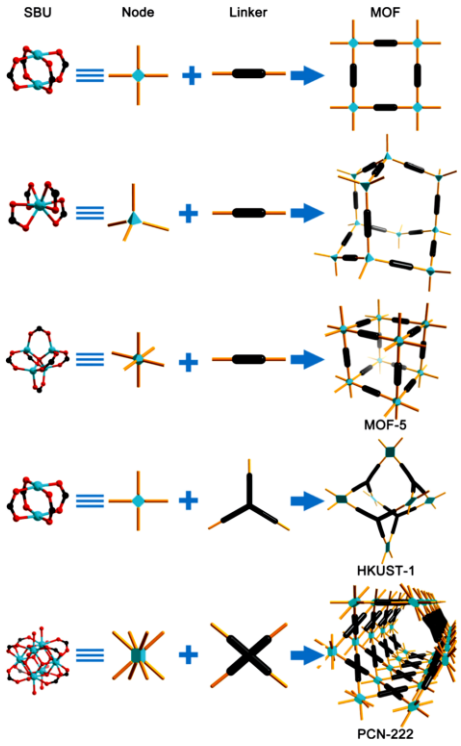

Figure 1-6. Graphical illustration of the construction of some representative coordination polymers/MOFs from SBUs and rigid linkers. MOF-5[12a], HKUST-1[23], PCN-222.[24]

In addition, the synthesis of MOFs through linker design with specific concentrates on tuning the topology and functionality for different application. The representative MOF with systematic design of pore size and functionality in isoreticular frameworks is MOF-5 (IRMOF-1) which consists zinc acetate and terephthalate with ditopic carboxylate.[25] O'Keeffe and Yaghi *et. al.* produce a variety of materials with the same network topology using same SBU and ditopic carboxylate linkers with different lengths. A strategy is reticulating metal clusters and organic linkers into extended networks.[26] As a result, a new class of porous materials isoreticular to MOF-5 were constructed from the octahedral $Zn_4O(CO_2)_6$ clusters and the rigid ditopic linkers, demonstrating a 3-D porous system has expanded pore size with the long molecular structures and can be functionalized with organic groups. The homogeneous periodic pores can be incrementally varied from 3.8 to 28.8 Å (Figure 1-7).[12c, 27]

After then, many reticular MOF series were prepared utilizing diverse connectivity metal clusters. The isoreticular MOF-74 structure shows large capacity, high selectivity, and fast kinetics of this material for adsorbing CO_2 from dry gas mixtures with N_2 and O_2 make it an attractive adsorbent for applications in which zeolites and inorganic bases are currently used, including the removal of CO_2 from air.[30]] A series of Mg-MOF-74 isoreticular structures with stepwise expansion depending on the length of linkers have pore range broadly from 14 to 98 Å; 98 Å is the largest pore aperture reported

in crystalline materials to date. The extremely stable MOFs, the UiO-66 (UiO = University of Oslo) with 12 connected inorganic brick reported in 2008 consists $ZrCl_4$ and terephthalate with ditopic carboxylate.[32] It was demonstrated that the regular octahedral cage can be easily expanded with increasing length of the linkers. As the length of longer linker increases, the surface area of the materials also increases from 1187 m^2/g to 4170 m^2/g (Figure 1-9). The new structure shows stability towards atmospheric moisture, high heat resistance, large void, and a broad variability of substituents at the linkers, including functional groups ready for post-synthetic modification.[33]

The ability to vary the size and properties of MOF structures without changing their underlying topology gave rise to the isoreticular principle and its application in making MOFs with the largest pore aperture (98 Å) and lowest density (0.13 g/cm^3). This has allowed for the selective inclusion of large molecules (e.g., vitamin B_{12}) and proteins (e.g., green fluorescent protein) and the exploitation of the pores as reaction vessels.[11] Along these lines, the thermal and chemical stability of many MOFs has made them amendable to post-synthetic covalent organic and metal-complex functionalization. These capabilities enable substantial enhancement of gas storage in MOFs and have led to their extensive study in the catalysis of organic reactions, activation of small molecules, gas separation, biomedical imaging, and proton, electron, and ion conduction.

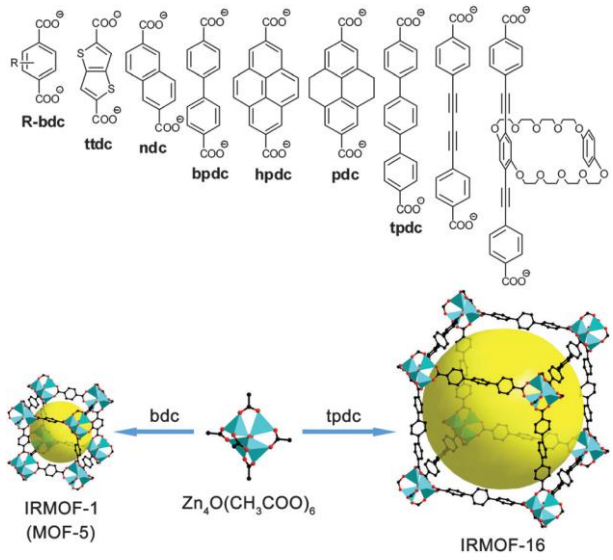

Figure 1-7. Some representative ditopic carboxylate linkers and illustration of formation of extended

I.1.2 Post-synthetic modification

Post-synthetic modification (PSM) is an alternative way to tune the pore shape or size and improve the properties of MOFs, depending on desired applications *via* introducing functional groups into

MOFs.[34] The method has been used to achieve the chemical modification of organic and inorganic materials where the type of chemical bonds are formed or broken during the post-synthetic approach such as (i) building block replacement; (ii) building block or functional group insertion; (iii) desolvating the guest molecules in pores of MOFs; (iv) self-assembly as a template (v) partially collapse *via* hydrolysis or acid treatment; (vi) heat treatment with/without intermediate and so on.

The first very simple example of PSM was with the Cu paddlewheel carboxylate MOF-11.[35] As-prepared Cu atoms are bonded to four carboxylate O atoms, and the coordination shell is completed typically with coordinated water (Figure 1-6). Subsequent removal of the water from the immobilized Cu atom leaves a coordinatively unsaturated site (CUS). Many other MOFs with such sites have now been generated and have proved to be exceptionally favorable for selective gas uptake and catalysis.[36] The first demonstration of PSM on the organic link of a MOF was reported in 2000 for a homochiral MOF, POST-1.[37] It involved N-alkylation of dangling pyridyl functionalities with iodomethane and 1-iodohexane to produce *N*-alkylated pyridinium ions exposed to the pore cavity.

Moreover, the isoreticular MOFs which are hard to prepare by conventional method were obtained via organic linker and/or metal ion exchange. The MOFs with **hms** topology prepared the isoreticular series by soaking as-synthesized MOFs in linker solution under appropriate condition.[38] The series of isoreticular shows outstanding CO_2 capture ability at low pressure and ambient temperature resulted from the attraction between framework and gas molecules. Also the MOFs embedded defects have been explored and investigated diversely on the potential properties and applications. By the hydrolytic PSM was used as preparing mesopores in POST-66 (Y) which have the intended defects (Figure 1-9).[39] Hierarchical MOFs consisting micro- and mesopores can be utilized to immobilize large guest molecules such as proteins and enzymes.

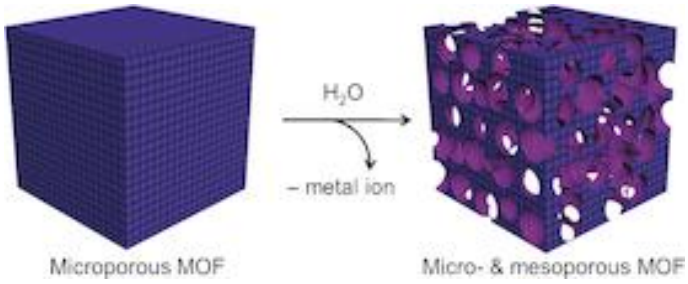

Figure 1-9. The scheme of hydrolytic post-synthetic transformation in a MOF, resulting in larger pores by partial removal of constituents.[39]

More recently, the important concept of "heterogeneity within order"[40] was forwarded and has led to increasing levels of MOF complexity[41], as exemplified by multivariate MOFs.[41c] Additional levels of MOF complexity have also been achieved through implementation of a core-shell strategy[42]

where one MOF with one set of unique properties is encased within a second MOF with a different set of unique properties. Rosi *et al.* successfully designed and synthesized a cobalt-adeninate core-shell structure with a porous mixed ligand core and a water stable bio-MOF-14 shell. They demonstrated that the water stable shell protects the water-sensitive core and how the shell can affect the N_2 and CO_2 adsorption behavior, creating a new material that has an internal capacity for CO_2 yet excludes N_2 (Figure 1-10).[43]

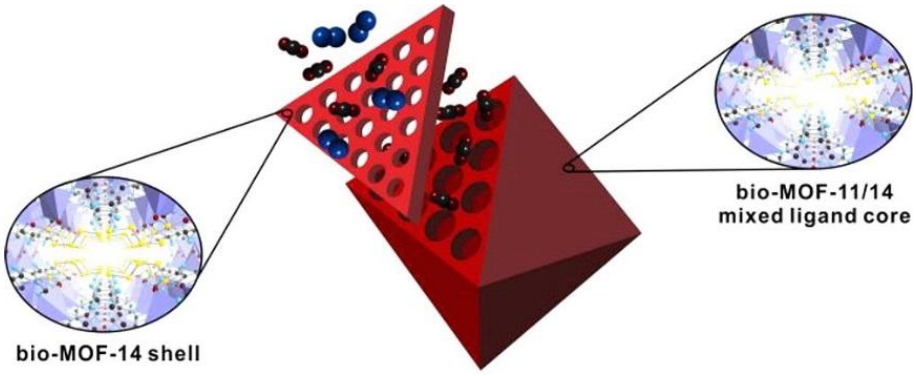

Figure 1-10. The scheme of core-shell MOFs comprising a porous bio-MOF-11/14 mixed core and a less porous bio-MOF-14 shell.[43]

I.1.3 Post-synthetic heat treatment

The post-synthetic heat treatment is basic but well-considered modification method of MOFs. Although the networks of MOFs are constructed with coordination bond between the metal ion or cluster and organic linkers, by post-synthetic heat treatment below its framework decomposition temperature, the annealed MOF crystals show structural change and/or the local vacancy sites due to partial decomposition. In the case of heat treatment above decomposition temperature, the porous metal oxide structure based on MOFs can be prepared.

Recently, Guo *et al.* suggested a simple and versatile method of achieving highly enhanced CO_2 uptake and binding by simply annealing the MOF structure at a temperature close but not exceeding selectively its framework decomposition temperature based on MOF-5.[44] This annealing treatment generates vacancy defect induced active sites at the framework linker and CUS as strong adsorption binding sites for many guest molecules. Also the retention of the framework structure with a high specific surface area and micropore volume synergistically promote the molecular adsorption.

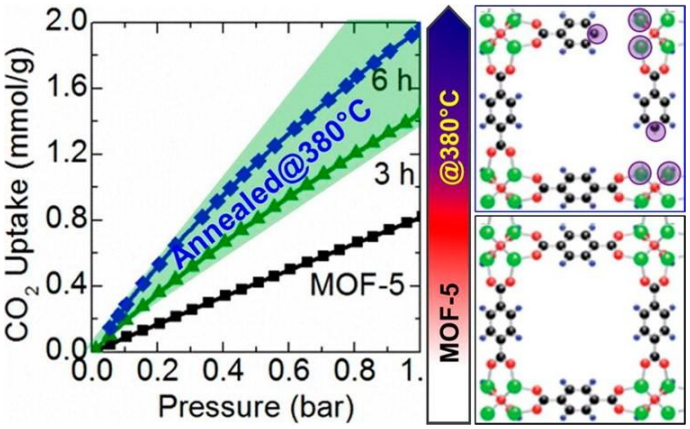

Figure 1-11. CO_2 uptake characteristic of the annealed samples with respect to the reference MOF 5. Schematic showing a MOF-5, annealing induced vacancies in framework structures; color code: C-black, H-gray, O-red, Zn-green.

The interpenetration of MOF is a way to tune the porosity drastically by changing structure via heat treatment. The interpenetration is generally considered undesirable because of the extremely low porosity.[45] On the contrary, many advantageous properties also arise when MOFs are interpenetrated, such as selective guest capture[45a], stepwise gas adsorption[46], enhanced framework robustness[47], photoluminescence control[48], and guest-responsive porosity[49]. The interpenetrated MOFs *via* post-synthetic heat treatment were prepared in Jaheon Kim's group.[50] Based on the MOF-123, they prepared a doubly interpenetrating form, MOF-246 whose crystal structure is identical to the backbone of MOF-123 by transformation. The optical microscopy of MOF-246 morphology reduced about 50 % in its thickness from 180 μm to 94 μm.

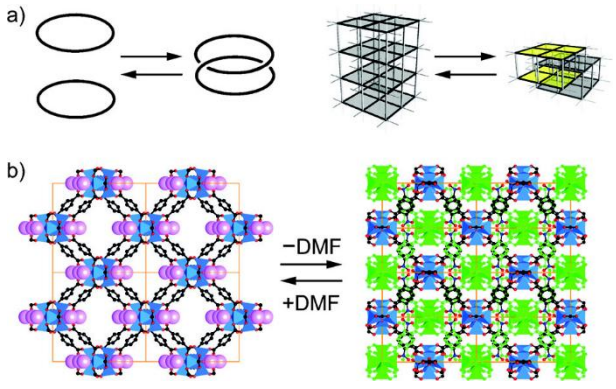

Figure 1-12. (a) catenation and decatenation processes in molecules (left) are observed in three-dimensional MOFs (right), which can be termed interpenetration and deinterpenetration. (b) MOF-123 is converted into the interpenetrating crystals of MOF-246 by the removal of coordinated *N*,*N*-dimethylformamide (DMF) (large pink spheres). C: black, N: blue, O: red, Zn: blue polyhedral. The interpenetrated framework is shown in green.

The nanoparticles (NP) and MOFs composite materials show enhanced properties comparing to the pure materials due to such synergistic effects, while more simple preparation methods are required for widespread use. Therefore recently, Hiroshi Kitagawa *et al.* implemented post-synthetic heat treatment by partial thermal decomposition of a MOF to generate metal NPs with tunable size within the MOF.[51] In order to generate partial decomposition, they heated the prepared Ni-MOF-74 to temperatures near decomposition range of the MOFs under vacuum and obtained hybrid materials (NPs@MOF) (Figure 1-12). This method was effective for fabricating the metal NP@MOF composites, and by tuning the temperature conditions the size of the metal NP was controlled. As a result, these hybrid material have the potential to form effective catalysts with high activity and selectivity, resulting from the synergistic effects of the several nanometer-scale Ni catalyst and porous properties of the MOFs.

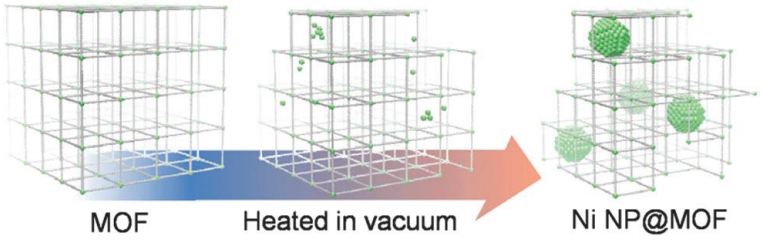

Figure 1-12. Scheme of the synthesis of Ni NPs@MOF.

Moreover, the post-synthetic heat treatment in MOFs above decomposition temperature transforms the metal ions in the MOFs to metallic or metal oxide nanoparticles, and the organic ligands into carbonaceous structures. This method provide successful preparation of nanoporous carbons derived from MOFs with controlled surface areas and porosities.[52] Moon group recently investigated this method using aliphatic carboxylate ligand-based MOFs (*aph*-MOF) and formed the nanoporous (*np*) metal oxides through control of the retention time and the evaporation rate of the organic moieties in the frameworks (Figure 1-13).[53] The hierarchical porous metal oxide showed superior performance at mass transport and recyclability. Furthermore, large population of surface defect sites on the *np*-metal oxide would affords a definite advantage for practical application.

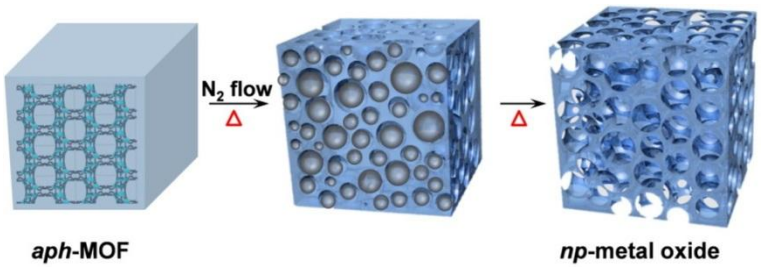

Figure 1-13. Schematic view of the direct conversion form *aph*-MOF to *np*-Metal oxide by heat treatment under nitrogen atmosphere.

I.2 Hierarchical Porous material

Hierarchical porous materials possessing ordered pores on the micro-, meso- and even macroscale[54] have been developed. In general, hierarchical porous structured materials provide large surface areas for reaction, superior mass transport of reactants, or dispersion of active sites at different length scales of pores and shorten diffusion paths or reduce diffusion effects.[55] However, many hierarchical supports contain disordered pore networks, or unintentionally alter the nature of active catalytic site incorporated either during synthesizing hierarchical structures. Typical synthetic strategies are classed as templating methodologies, self-assembly or post-synthetic treatment. The hierarchical porous structure is expected to open new application opportunities.[56]

Interest in hierarchical porous structures has burgeoned over the past decade. The hierarchical structured materials are expected to open a variety of application opportunity based on their various characteristics. The first hierarchical macroporous-mesoporous material was report in 1998 by Yang *et al*.,[57] although only recently has their application in catalytic processes been exploited. Surprisingly, the use of theses meso-macro materials as catalyst has been the subject of several reviews.[58] Besides, the first zeolite-based hierarchical porous films were reported by the early 1990s. Zeolite thin films and layers are of interest for use as membranes in separations devices and membrane reactors .They can also serve as chemical sensors and hosts for guest species, which in turn impart the material with optical, electrical or magnetic properties.[59] In the case of porous carbons, they can provide electrically conductive phases as well as intercalations sites. In recent year, hierarchically structured porous materials also provide more efficient energy conversion and storage; rechargeable batteries, catalytic electrodes for fuel cell, photovoltaic cells (Figure 1-14).[55]

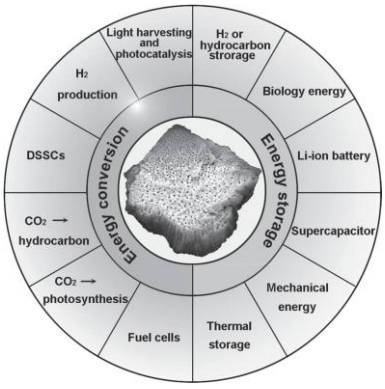

Figure 1-14. Illustration of the potential application on energy conversion and storage of the hierarchically porous materials.[55]

The design and tunability of pore structures and properties are one of the most attractive strength of MOFs. Therefore, many researches demonstrated various approaches for preparing MOFs. Among them, the 'pillared-layer' strategy is reported as not only one of the systematic methods in modifying porosity of MOFs but also control the chemical functionality. This is the way to construct 3-dimensional structures *via* connection of durable 2-dimensional layers by pillaring linkers.[60]

The MOFs of **hcb** topology could be one of the representative durable 2-D structures. The topology looks like a honeycomb built of an infinite hexagon (Figure 1-15a). 3-D Frameworks of **hms** and **gra** topologies are the networks derived from **hcb** topology, where the 2-D sheets are interconnected with 'pillared-layer' strategy along the crystallographic *ab*-plane to form a microporous 3-D structures. The neighboring 2-D sheets and metal nodes in **hms** net are connected in a line along the crystallographic *c*-axis to form an 1-D channel with pillaring linker (Figure 1-15 (c) and (e)). The 2-D sheets in **gra** net are stacked alternatively like A-B-A-B, and the neighboring metal nodes are connected to form a three-dimensional microporous structure with pillaring linker (Figure 1-15 (d) and (f)).

Sun Group reported MOFs of **hms** topology with Ni (II) metal as 'pillared-layer' 3-dimensitional structures.[61] In the infinite extended sheet layer of $[Ni(HBTC)(DMF)_2]\cdot$(guest), **1**, the nickel (II) is coordinated with three H_3BTC units. They also successfully obtained a 3-D network $[Ni(HBTC)(bipy)]\cdot 3DMF$, **2,** with the neutral pillaring linkers placed in between stacked 2-D layers, such as 4,4'-bipyridine (bipy) binding nickel centers.

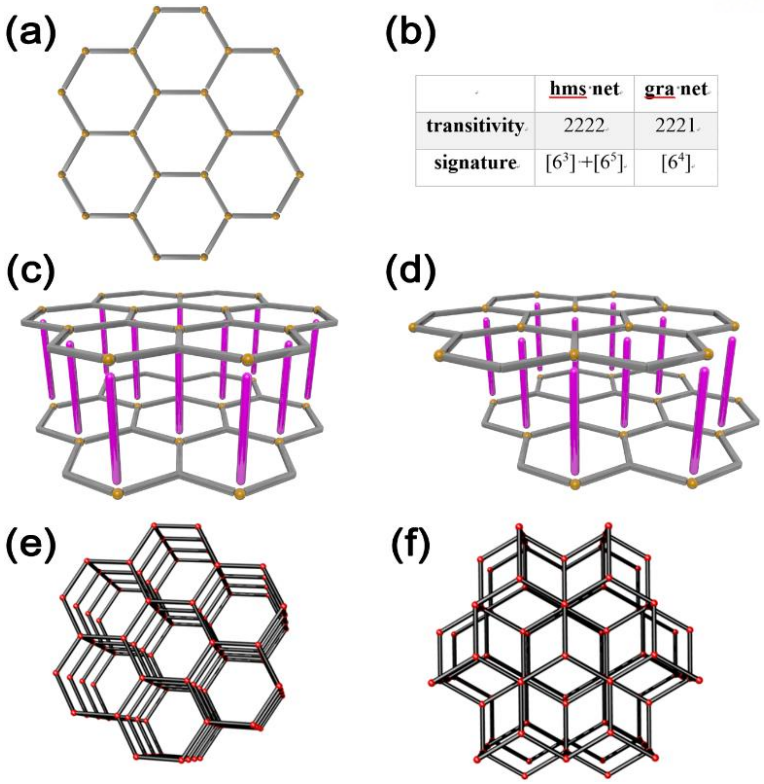

	hms net	gra net
transitivity	2222	2221
signature	$[6^3]+[6^5]$	$[6^4]$

Figure 1-15. (a) **hcb** topology; (b) the table of the transivity and signature of **hms** net and **gra** net; (c) connectivity of **hms** topology; (d) connectivity of **gra** topology; (e) stacked 3-D structure of **hms** topology; (f) stacked 3-D structure of **gra** topology.

The coordination environment of the metal center for **1** is presented in Figure 1-16a, where the nickel (II) center is bounded by three BTC units. Also the propagation of alternate nickel centers and BTC linkers leads to infinite extended sheets along the *ab*-plane (Figure 1-16c). The sheets stack along the *c*-axis to give the 3D structure with an approximate distance of 7 Å between adjacent layers. The synthesis of compound **2** was based on introducing the bipy ligand under similar condition to **1**. The single X-ray diffraction revealed that the honeycomb grid layers, constructed by Ni (II) ions and BTC groups as in **1**, are linked by bipy pillars to form a 3D highly porous framework with **hms** topology (Figure 1-16b).

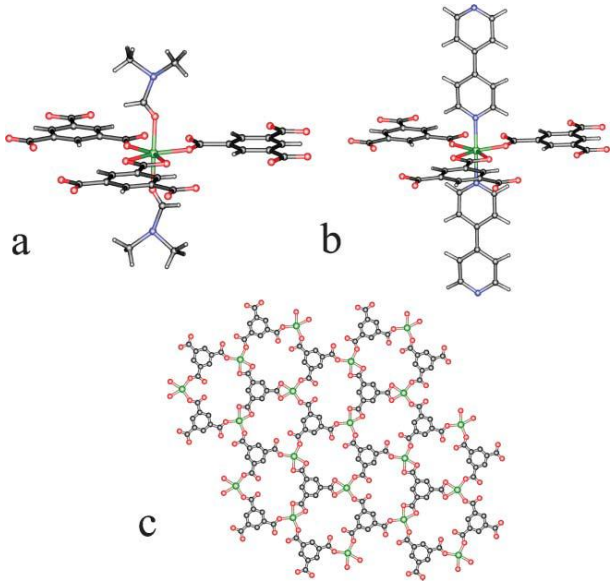

Figure1-16. Coordination environments of Ni (II) ions in the asymmetric units of (a) **hcb** 2-dimensional layer and (b) **hms** 3-dimensional structure pillared with **bipy**, and a fragment of the 2D layer (c) included both in **hcb** and **hms** structures.

Lah group also reported a series of isoreticular structures of **hms** and **gra** topologies, respectively, with different neutral ligands, bipy, dabco (1,4-diazabicyclo[2.2.2]octane) and pz (pyrazine), in order to control the pore dimensions and properties (Figure 1-17).[38] The **hms** MOFs pillared with dabco (**dabco-hms**) and pz (**pz-hms**) were prepared *via* post-synthetic ligand exchange from the **hms** bipy-MOFs because they were not capable to be synthesized by conventional solvothermal reaction (Figure 1-18). The MOFs of **gra** topology were also prepared with bipy (**bipy-gra**) and pz (**pz-gra**) *via* post-synthetic ligand insertion from the 2-D sheet **hcb** MOF, [Ni(HBTC)$(DMF)_2$(guest)]. Indeed, the structures with **hms** and **gra** topology are polymorphic MOFs of the same [Ni(HBTC)(L)] (L = bipy or pz) formula, and the same 3,5-connection, but different net topologies. In both of the **hms** and **gra** structures, the Ni (II) ions in the 2-D sheet, [Ni(HBTC)], of an **hcb** topology are interconnected to the Ni (II) ions of the next neighboring 2-D sheets *via* pillaring neutral linkers to form the 3,5-c network. On the other hand, the polymorphic framework of the **hms** topology produces a different kind of the cage-like pores being aligned along the crystallographic *c*-axis to form a 1-D channel.[38]

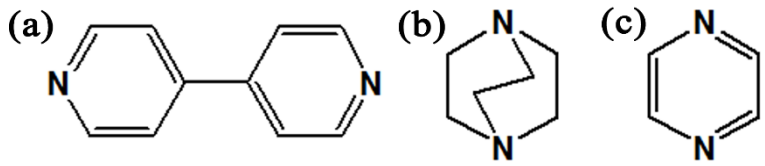

Figure 1-17. The scheme of neutral pillaring ligands (a) bipy; (b) dabco; (c) pz

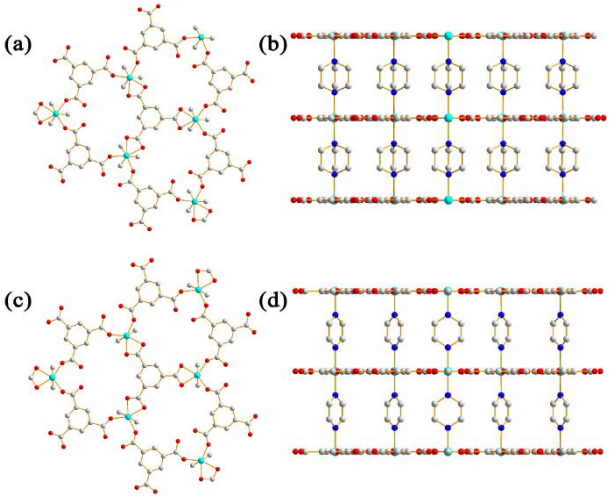

Figure 1-18. The structure of **dabco-hms** (a) top view, (b) side view and **pz-hms** (c) top view, (d) side view.

The porosity of hms-MOFs was modified by exchanging the pillaring linker ligand and the topology of the MOFs was controlled either *via* direct solvothermal reactions with the appropriate pillaring ligands or *via* pillar insertions the between 2-D sheets. The interesting result for the smaller pore MOFs is shown in the CO_2 adsorption and CH_4 adsorption at ambient temperature. The amount of gas adsorption is greater in the shorter pillared MOFs than it in the bipy pillared MOFs (Figure 1-19 (a) and (b)). The interaction between framework and guest molecules at room temperature effects significantly on the amount of gas uptake; therefore, the frameworks pillared with smaller linkers are more beneficial for attraction and capturing the gas molecules. The high adsorption enthalpies of frameworks also support the results (Figure 1-19c).

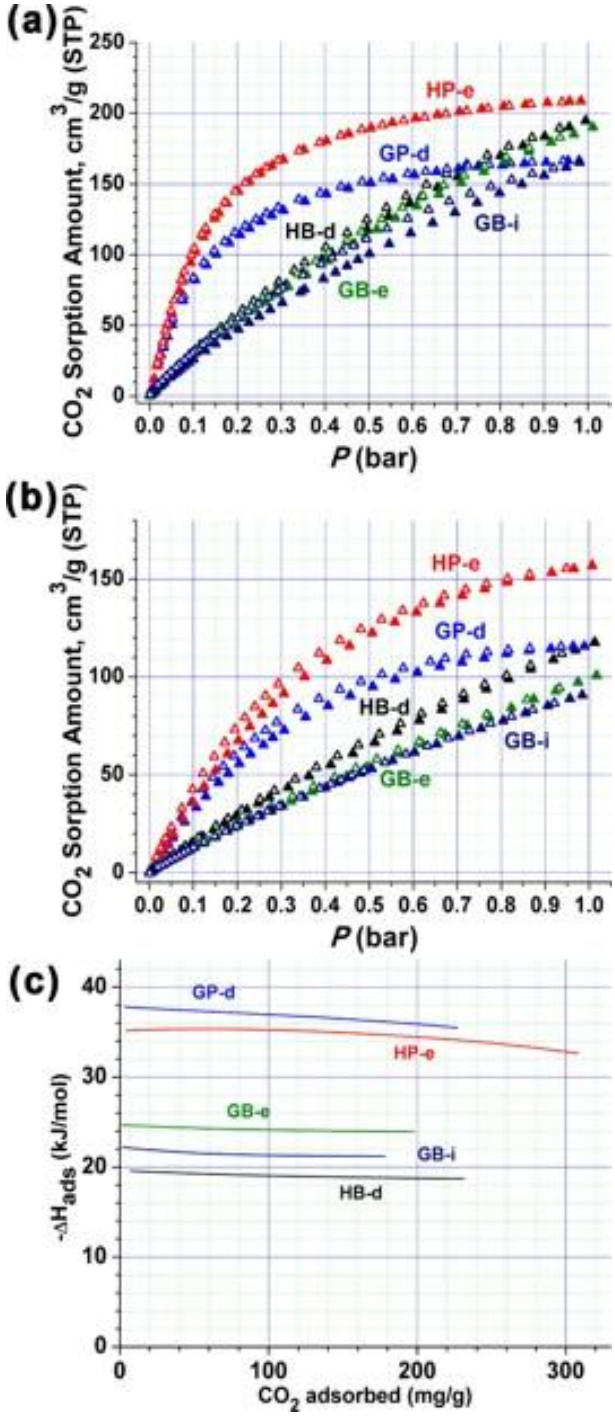

Figure 1-19. CO_2 sorption isotherms on **bp-hms** (HB-d), **bp-gra** (GB-e and GB-i), **pz-hms** (HP-e), and **pz-gra** at (a) 273 K and (b) 298 K and (c) the adsorption enthalpies.

The interpenetration is alternative way to tune the porosity of MOFs. Jaheon Kim's group reported the change of the interpenetration degree using a MOF with **pcu** topology via post synthetic heat treatment. They synthesized a non-interpenetrated 3-D MOF, $[Zn_7O_2(NBD)_5(DMF)_2]$ (MOF-123; NBD = 2-nitrobenzene-1,4-dicarboxylate) by solvothermal reaction and triggered the transformation of non-interpenetrated MOF-123 to a doubly interpenetrated form, MOF-246, $[Zn_7O_2(NBD)_5$. The DMF addition into doubly interpenetrated MOF-246 resulted in the reverse transformation to give non-interpenetrated MOF-123 (Figure 1-20b).[22]

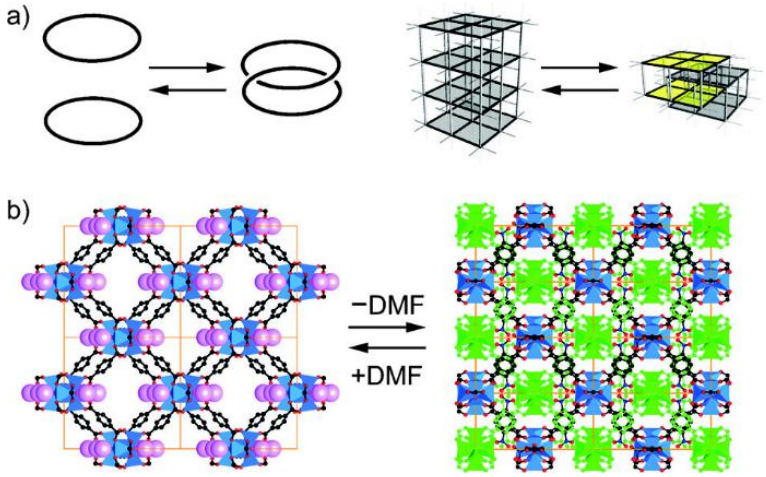

Figure 1-20. (a) Catenation and decatenation processes in molecules (left) are observed in three-dimensional MOFs (right), which can be termed interpenetration and deinterpenetration. (b) MOF-123 is converted into the interpenetrating crystals of MOF-246 by the removal of coordinated DMF (large pink spheres). C black, N blue, O red, Zn blue polyhedral. The interpenetrated framework is shown in green.[22]

According to the variable temperature powder X-ray diffraction (VT-PXRD) patterns, the MOF-123 undergoes structural changes to produce a new phase *via* intermediates. And the profile of the PXRD patterns indicates the completion of the transformation into a new phase, MOF-246, the structure of which is drastically different from the starting component, MOF-123 (Figure 1-21a). As the gradual interpenetration requires changes in the porosity of MOF-123, gas adsorption measurements were performed to probe the porosity features related to the forward and reverse transformation in bulk samples (Figure 1-21b).

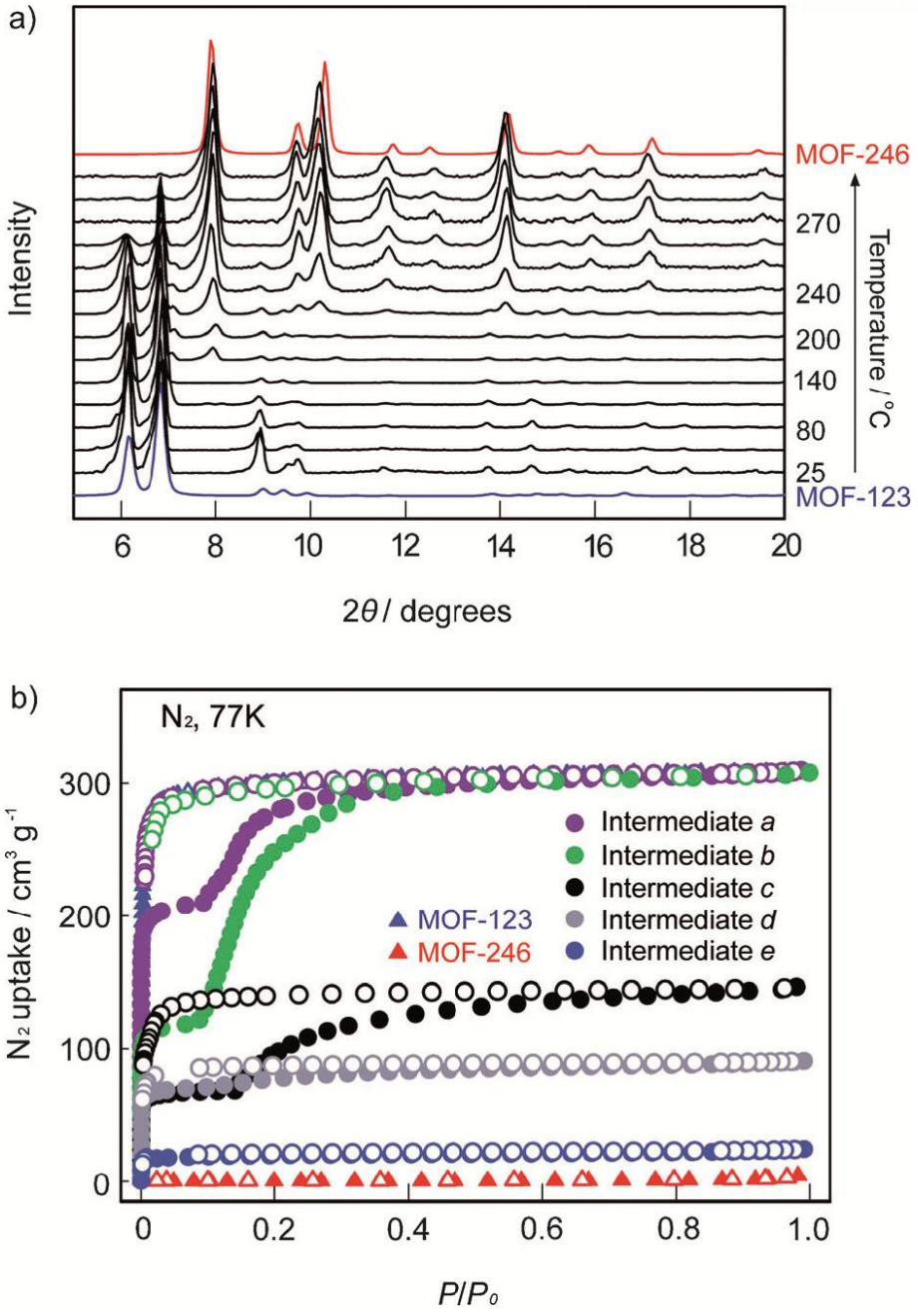

Figure 1-21. (a) PXRD patterns for the interpenetration along with the heating temperatures. (b) N2 adsorption isotherms measured at 77 K for the sample, MOF-123, intermediates (a to e), and MOF-246. The sample have been prepared by heating MOF-123 at (a) 70 ºC, (b) 90 ºC, (c) 140 ºC, (d) 180 ºC, (e) 220 ºC, and 260 ºC under vacuum.[22]

Defect-engineering in MOFs is an interesting concept for tailoring material properties. In fact, the defects strongly affect the physical and chemical properties of structures, such as reduced network rigidity and structural "imperfection". In attractive approaches, the defects could give rise to useful material properties and functions. One of the good consequences is boosting the porosity of the MOF materials, which suggests a potential method to increase the MOF pore volume and surface area in MOFs. They often serve as active sites for adsorption and subsequent reactive transformation in heterogeneous catalysis. Therefore, a variety of strategies have been reported for manipulating the crystal quality and specific properties desired in materials by judicious control over the defect structure, that is, "defect engineering" (Figure 1-22).[15]

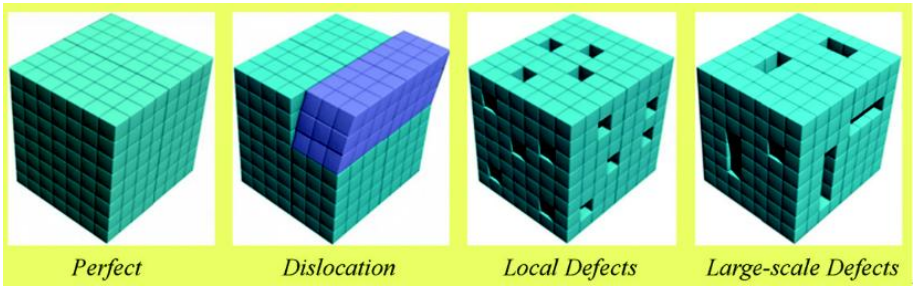

Figure 1-22. The definition of defects: the missing incorrectly located atoms generate vacancies and dislocations in materials.

By means of a simple and effective method of post-synthetic heat treatment below the framework decomposition temperature, structural vacancies could be created in the MOFs, which has important implications for additional porosity and molecular binding. Guo *et al.* generated the MOF-5 with very active local vacant sites by partial decomposition of the bridging carboxylates of the framework linker.[44] The carboxylate group, which is coordinating the Zn_4O tetrahedra, is the weakest bond in 1,4-benzenedicarboxylic acid.[62] Thus, the weakly bonded carboxylates start to decompose primarily at mild annealing temperatures.[63] At high annealing temperatures, the increased mass-loss represents a further decomposition of the benzene rings in 1,4-benzenedicarboxylic acid (Figure 1-23).

The annealed MOF-5 structure show higher total pore volumes than the initial MOF-5. The increase of the high pore volume of MOF-5 is in line with a vacant defect-induced enhancement. Furthermore, the MOF-5 structure with the ligand vacant sites showed highly enhanced CO_2 uptake and binding. This annealing treatment generates defects, introducing active sites to the frameworks as strong adsorption binding sites for many guest molecules. Also the retention of the framework structure with a high specific surface area and micropore volume synergistically promote the molecular adsorption.

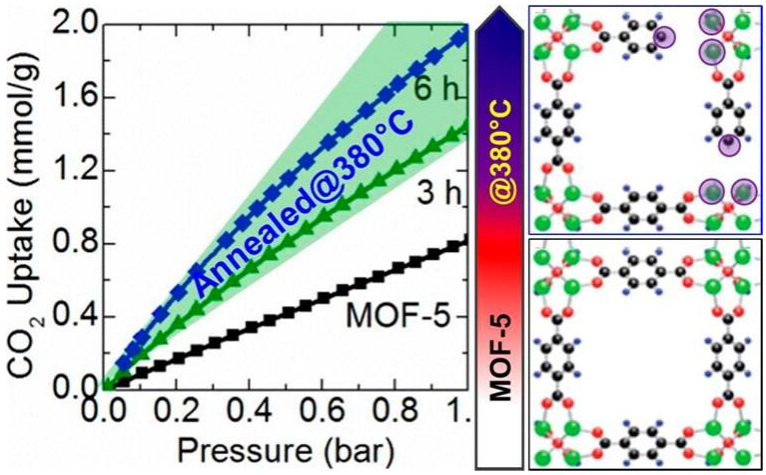

Figure 1-23. CO_2 uptake characteristic of the annealed samples with respect to the reference MOF 5. Schematic showing a MOF-5, annealing induced vacancies in framework structures; color code: C-black, H-gray, O-red, Zn-green.[44]

Based on the previous researches on the MOFs with **hms** topology, herein, we prepared a series of isoreticular hms-MOFs using longer linkers than bipy because controlling porosity toward the MOFs with smaller pore size than bipy has been reported while the MOFs with larger pore size than that with bipy were not explored. It would prove that hms-MOFs were useful for tuning porosity systematically based on lengths of pillaring linkers. Therefore, the longer neutral linkers, 4,4-azopyridine (azopy) and bis(4-pyridyl)acetylene (bpa) were adopted for synthesizing new porous 3-D frameworks between 2-D sheets. The linker azopy with N-N double bond could have superior CO_2 capture ability than bipy linker because of the stronger Lewis basicity of the N-N double bond. On the other hand, the linker bpa with triple bond is rigid and longer than bipy. The linkers were long enough to control porosity of MOFs with **hms** topology.

In the MOF with **hms** topology, the neutral 2-D sheets are pillared by neutral pillaring linker (azopy or bpa) through Ni-N coordinated bonds. According to the structural nature, this layer-pillared frameworks allow the occurrence of interpenetration. Moreover, upon the increasing length of the organic spacers, the occurrence of interpenetration appears to be easier, which usually induces the tight structure or microporous frameworks.[64] Since the interpenetrated structure reported before through post-synthetic heat treatment was only **pcu** net, we desired to design another interpenetrated MOFs with complex topology *via* post-synthetic thermal treatment. The hms-MOFs pillared by longer neutral linker are expected to derive the interpenetration approach *via* post-synthetic heat treatment under the coordinative solvent condition.

According to the several reported results, interpenetrated structures were able to enhance the stability and tune the pore size drastically. On the other hands, the interpenetrated MOFs are not suitable for commercialization due to their extremely low porosity and surface area. To compensate the weakness of interpenetrated MOFs, the defect-engineering strategy is implemented to generate the intended defects in MOFs before interpenetrating process. Since the MOFs with **hms** topology are constructed with neutral 2-D sheets and pillaring neutral linkers, the selective removal of a neutral ligand can be achieved by a soft thermal treatment under vacuum conditions.[65] This approach creates the additional porosity by linker vacancies, also it can moderate the concentration of vacancy systematically depending on various thermal conditions. Moreover, the removal of linkers from the ideal structure generates CUS which can possibly show Lewis acid features which appears catalytic performance.

In final, through combining the defect engineering method and interpenetration strategy by post-synthetic heat treatment, the hms-MOF can be modified with diverse pore size distribution as hierarchical porous frameworks which are consisted with micro- and mesopores. The hierarchical

porous MOFs are expected for potential application such as selectivity for molecules and catalysts because they can contain lager amount of guest molecules and have benefits for mass transportation.

II. Experimental Section

General Procedures

All reagents were purchased from commercial sources and used without further purification. Elemental analyses (EA) (for C, H, and N) were conducted on an elemental analyzer, Flash 2000, at the Ulsan National Institute of Science and Technology, Korea. Fourier Transform–Infrared (FT–IR) spectra were recorded as ATR with a NIICOLET iS 10 FT–IR spectrophotometer (3600–400 cm^{-1}). PXRD data were recorded using a Bruker D2 Phaser automated diffractometer at room temperature with a step size of 0.02° in 2θ angle. Simulated PXRD patterns were calculated with the Material Studio program[66] using single-crystal structures. Thermogravimetric analyses (TGA) was performed under flowing nitrogen gas at a scan rate of 5 ºC min^{-1}, using Q-600 series from TA instruments. Nuclear magnetic resonance (NMR) spectra were obtained on a 400-MR DD_2 NMR spectrometer.

Syntheses

Preparation of MOFs via conventional solvothermal reaction. A series of isostructural MOFs, [Ni(HBTC)(L)] (L = azopy and bpa), were prepared via solvothermal reactions that were slightly modified from the reported synthetic procedures.[7]

Synthesis of [Ni(HBTC)(azopy)], azo-hms. A solid mixture of $Ni(NO_3)_2{\cdot}6H_2O$ (0.035 g, 0.12 mmol), H_3BTC (0.02 g, 0.1 mmol) and azopy (0.018 g, 0.10 mmol) was dissolved in mixed solvent of 10 mL DMF and 5 mL MeOH in a 30 mL glass vial. The solution was then heated in an isotherm oven at 60 ºC for 3 days, resulting in reddish green hexagonal crystals, which were collected by filtration and washed with fresh DMF. The activated sample was prepared by soaking the crystals of **azo-hms** in fresh DMF for 2-3 days and in methylene chloride (MC) for 1 day and then vacuum-drying at 120 ºC for 3 hours. The elemental analysis (EA) was performed using the activated sample exposed in air for a couple of hours before the analysis. Yield = 45.3 % (24.6 mg). Elemental analysis calc. for $NiC_{19}H_{24}N_4O_{11}$: C, 40.79; H, 3.25; N, 9.51 %. Found: C, 41.21; H, 3.2; N, 10.19 %. IR of the activated sample (ATR, cm^{-1}): 3195.31 (w, b), 3099.43 (w, b), 1694.02 (w), 1660.03 (m), 1605.68 (s), 1538.30 (s), 1494.00 (w), 1434.18 (s), 1417.05 (m), 1360.62 (s), 1225.56 (m), 1100.94 (m), 1050.74 (m), 1020.56 (m), 932.18 (w), 838.94 (s), 757.97 (w), 742.04 (w), 714.63 (m), 680.10 (w)

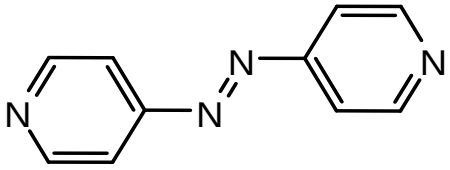

Figure 2-1. azopy

Synthesis of [Ni(HBTC)(bpa)], bpa-hms. A solid mixture of $Ni(NO_3)_2 \cdot 6H_2O$ (0.035 g, 0.12 mmol), H_3BTC (0.02 g, 0.1 mmol), and bis(4-pyridyl)acetylene (bpa) (0.0361 g, 0.200 mmol) was dissolved in a mix solvent of 10 mL *N*,*N*-diethyl formamide (DEF) and 5 mL EtOH in a 30 mL glass vial. The solution was then heated in an isotherm oven at 70 ºC for 3 days, resulting in light green hexagonal crystals being formed, which were collected by filteration and washed with fresh DMF. The activated sample was prepared by soaking the crystals of **bpa-hms** in fresh DMF for 2-3 days and in MC for 1 day and then vacuum-drying at 120 ºC for 3 hours. The elemental analysis (EA) was performed using the activated sample exposed in air for a couple of hours before the analysis. Yield = 77.6 % (41.7mg). Elemental analysis calc. for $NiC_{21.8}H_{17.5}N_2O_{8.5}Cl_{1.5}$: C, 47.15; H, 3.18 N, 5.04 %. Found: C, 46.31; H, 3.21; N, 5.10 %. IR of the activated sample (ATR, cm^{-1}): 3709.23 (w, b), 1662.80 (m), 1608.80 (s), 1545.82 (m), 1442.95 (m), 1369.05 (s), 1256.84 (w), 1215.06 (m), 1099.51 (m), 1065.13 (m), 1020.63 (m), 987.86 (w), 932.06 (w), 865.21 (m), 828.24 (s), 759.92 (m), 743.28 (m), 716.48 (m)

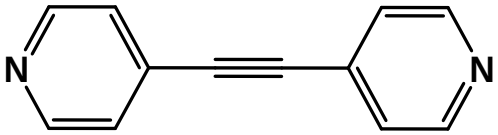

Figure 2-2. bpa

Preparation of MOFs via post-synthetic heat treatment. Before the heat treatment of MOFs, the as-synthesized single crystals were washed with fresh DMF several times and soaked in DMF for a couple of days to remove any remaining reactants and side products present in the solvent cavities. After the solvent had been decanted, the crystals were air-dried at ambient temperature for a couple of hours.

Synthesis of [Ni(HBTC)(azopy)], azo-hms-c. The crystals of **azo-hms** presoaked in DMF was heated from ambient temperature to 250 ºC, with increasing 5 ºC /min and aging at 250 ºC for 2 hours for a complete interpenetration process. The heat treatment changed the color of crystals from reddish green to brown. Elemental analysis calc. for $NiC_{19}H_{13}N_4O_7$: C, 48.76; H, 2.80; N, 11.97 %. Found: C, 47.97; H, 2.81; N, 12.22 %. IR of the activated sample (ATR, cm^{-1}): 3232.75 (w, b), 3067.61 (w),

1661.80 (s), 1604.33 (s), 1567.86 (m), 1538.58 (s), 1489.03 (m), 1446.49 (s), 1418.48 (w), 1383.41 (s), 1226.01 (m), 1195.59 (w), 1097.61 (m), 1056.45 (m), 1019.73 (m), 939.34 (w), 839.43 (s), 736.97 (m), 741.66 (s), 719.05 (s)

Synthesis of [Ni(HBTC)(bap)], bpa-hms-c. The crystals of **bpa-hms** presoaked in DMF was heated from ambient temperature to 300 ºC, with increasing 10 ºC /min and aging at 300 ºC for an hour for a complete interpenetration process. The heat treatment changed the color of crystals from light green to dark green. Elemental analysis calc. for $NiC_{21}H_{15}N_2O_8$: C, 52.32; H, 3.14; N, 5.81 %. Found: C, 52.08; H, 2.92; N, 5.82 %. IR of the activated sample (ATR, cm^{-1}): 3074.92 (w,b), 1663.30 (s), 1609.76 (s), 1546.30 (s), 1504.94 (m), 1447.01 (s), 1383.75 (s), 1324.86 (w), 1256.16 (w), 1212.62 (m), 1098.06 (m), 1066.69 (m), 1018.37 (m), 941.97 (w), 867.72 (m), 832.05 (s), 760.86 (m), 741.67 (m), 718.77 (m)

Crystallographic data collection and refinement of the structures

Crystals of **azo-hms**, **bpa-hms**, **azo-hms-c** and **bpa-hms-c** were coated with Paratone oil and the diffraction data were measured at 100 K or 173 K using synchrotron (PAL-2D beamline) or Mo Kα radiation equipped with incident beam monochromator. The set of ADSC Q210 ADX program[67] and HKL3000sm[68] or the Rapid Auto software package[69] was used for each data collection and processing. All structures were determined using direct methods employing SHELXS. The structures were refined using full-matrix least-squares calculations employing the SHELXL of the SHELX program package.[70]

All non-hydrogen atoms in structures were refined anisotropically; the hydrogen atoms were assigned isotropic displacement coefficients U (H) = 1.2U (C), their coordinates were allowed to ride on their respective atoms. The least-squares refinement of the structural model was performed under geometry restraints and displacement parameter restraint such as DANG, DELU, DFIX, FLAT, ISOR and SIMU.

[Ni(HBTC)(azo)], azo-hms. Two different kinds of nickel atoms, connecting to BTC ligands and azopy molecules, respectively (one is on a general position and the other is on a mirror plane) were observed as an asymmetric unit. The final refinement was performed with the modification of the structure factors for the electron densities of the disordered solvents (3885.7 $Å^3$ (64.2% of the total unit cell volume); 786 electrons correspond to ~ 14 DEF molecules per unit cell) using the SQUEEZE option of PLATON.[71] Refinement of the structure converged at a final $R1$ = 0.0425 and $wR2$ = 0.1256 for 5426 reflections with $I > 2\sigma(I)$; $R1$ = 0.0629 and $wR2$ = 0.1369 for all 7565 reflections. The largest difference peak and hole were 0.503 and –0.395 $e \cdot Å^{-3}$, respectively.

[Ni(HBTC)(bpa)], bpa-hms. One nickel atom, a half ligand totally, and one quarter bpa molecule are observed as an asymmetric unit. The final refinement was performed with the modification of the structure factors for the electron densities of the disordered solvents (2188.5 $Å^3$ (66.5% of the total unit cell volume); 386 electrons correspond to ~ 9.7 DMF molecules per unit cell) using the SQUEEZE option of PLATON.[71] Refinement of the structure converges at a final *R1* = 0.0981, *wR2* = 0.2332 for 1404 reflection with $I > 2\sigma(I)$; *R1* = 0.1168, *wR2* = 0.2518 for all 1921 reflections. The largest difference peak and hole were 1.165 and -0.435 $e \cdot Å^{-3}$, respectively.

[Ni(HBTC)(azo)], azo-hms-c. One nickel atom, two different coordinated ligands with disorder placed on crystallographic *mm*2 site symmetry and disordered half pyrazine are observed as an asymmetric unit. The final refinement was performed with the modification of the structure factors for the electron densities of the disordered solvents (518.4 $Å^3$ (16.4% of the total unit cell volume); 141 electrons correspond to ~ 3.5 water molecules per unit cell) using the SQUEEZE option of PLATON.[71] Refinement converged at a final *R*1 = 0.1364 and *wR*2 = 0.3774 for 2192 reflections with $I > 2\sigma(I)$; *R*1 = 0.1898 and *wR*2 = 0.4123 for all 3954 reflections. The largest difference peak and hole were 1.383 and –0.929 $e \cdot Å^{-3}$, respectively.

[Ni(HBTC)(bpa)], bpa-hms-c. One nickel atom with crystallographic *m2m* site symmetry, two different coordinated ligands with disorder placed on crystallographic *-62m* and *-6* site symmetry and bpa molecule with crystallographic *m2m* site symmetry are observed as an asymmetric unit. The final refinement was performed with the modification of the structure factors for the electron densities of the disordered solvents (904.4 $Å^3$ (28.1% of the total unit cell volume); 30 electrons correspond to ~ 0.75 water molecules per unit cell) using the SQUEEZE option of PLATON.[71] Refinement converged at a final *R*1 = 0.3209 and *wR*2 = 0.6236 for 643 reflections with $I > 2\sigma(I)$; *R*1 = 0.3567 and *wR*2 = 0.6388 for all 945 reflections. The largest difference peak and hole were 2.173 and –-1.335 $e \cdot Å^{-3}$, respectively.

A summary of the crystal data for **azo-hms**, **bpa-hms**, **azo-hms-c** and **bpa-hms-c** is given in Tables 3-1 and 3-2.

Activation of MOFs. The following procedure was used for the activation of all the MOFs. The as-synthesized crystals were soaked in MC for 1 d: MC was refreshed two times during the soaking process. The resulting MC-soaked samples were transferred as a suspension in a BET-sample-cell and the solvent was decanted. Then, the crystals in BET-sample-cell is evacuated and dried for a day.

Gas Sorption Measurements. All of the gas sorption isotherms were measured using a BELSORP-max (BEL Japan, Inc.) sorption system employing a standard volumetric technique up to saturation

pressure. The N_2 (purity of 99.9999%) sorption isotherms were monitored at 77 K. The adsorption data in the pressure range of < 0.1 P/P_0 were fit to the Brunauer-Emmett-Teller (BET) equation to determine the BET surface area. The entire set of adsorption data was used to obtain the Langmuir specific surface area. The CO_2 (purity of 99.9999%) sorption isotherms were measured at 195, 273 and 298 K, respectively.

Table 2-1. X-ray crystallographic data of **azo-hms** and **bpa-hms**

compound	**azo-hms**	**bpa-hms**
Formula	$C_{57}H_{36}NO_{18}Ni_3$	$C_{21}H_{12}N_2O_6Ni$
F.w.	1353.11	447.04
Temperature (K)	173(2)	173(2)
Wavelength (λ, Å)	0.71073	0.71073
Crystal system	Monoclinic	Hexagonal
Space group	*Cm*	*P*-62*m*
***a*, Å**	16.384(3)	16.624(2)
***b*, Å**	28.376(6)	16.624(2)
***c*, Å**	13.079(3)	13.752(3)
***α*, deg**	90	90
***β*, deg**	95.57(3)	90
***γ*, deg**	90	120
V, Å ^{3}	6052(2)	3291.4(9)
Z	2	3
Density (g/cm^{-3})	0.743	0.677
Absorption coefficient (μ, mm^{-1})	0.503	0.461
***F*(000)**	1380	684
Crystal size (mm^3)	0.30 x 0.29 x 0.10	0.23 x 0.20 x 0.11
Theta range for data collection(º)	3.005 to 24.000	3.194 to 23.994
Index ranges	$-18 \le h \le 18$, $-32 \le k \le 32$, $-14 \le l \le 14$	$-17 \le h \le 19$, $-19 \le k \le 19$, $-15 \le l \le 15$
Reflections collected	18603	21708
Independent reflections	8954 [R(int) = 0.2263]	1921 [R(int) = 0.2087]
Completeness to theta = 24.000º (%)	99.3	99.3
Absorption correction	Semi-empirical from equivalents	Semi-empirical from equivalents
Max. and min. transmission	0.951 and 0.864	0.951 and 0.901
Refinement method	Full-matrix least-squares on F^2	Full-matrix least-squares on F^2
Data / restraints / parameters	8954 / 542 / 386	1921 / 49 / 90
Goodness-of-fit (F^2)	1.016	1.036
Final R indices [I>2sigma(I)]	$R_1 = 0.1322$,[a] $wR_2 = 0.3130$[b]	$R_1 = 0.0981$,[a] $wR_2 = 0.2332$[b]
R indices (all data)	$R_1 = 0.2243$,[a] $wR_2 = 0.3923$[c]	$R_1 = 0.1168$,[a] $wR_2 = 0.2518$[c]
Largest diff. peak and hole (e Å $^{-3}$)	1.221 and -0.977	1.165 and -0.435

Table 2-2. X-ray crystallographic data of **azo-hms-c** and **bpa-hms-c.**

compound	**azo-hms-c**	**bpa-hms-c**
Formula	$C_9H_{12}N_4O_6Ni$	$C_{21}H_{11}O_6Ni$
F.w.	451.04	446.03
Temperature (K)	173(2)	173(2)
Wavelength (λ, Å)	0.670	0.71073
Crystal system	Trigonal	Hexagonal
Space group	*P-3*	$P6_3/mcm$
***a*, Å**	16.621(2)	16.500(2)
***b*, Å**	16.621(2)	16.500(2)
***c*, Å**	13.117(3)	13.665(3)
***α*, deg**	90	90
***β*, deg**	90	90
***γ*, deg**	120	120
V, Å ^{3}	3138.1(11)	3221.9(11)
Z	6	6
Density (g/cm^{-3})	1.432	1.379
Absorption coefficient (μ, mm^{-1})	0.823	0.941
***F*(000)**	1380	1362
Crystal size (mm^3)	0.040 x 0.040 x 0.008	0.280 x 0.180 x 0.060
Theta range for data collection(º)	2.310 to 23.991	3.305 to 23.994
Index ranges	$-20 \le h \le 20$, $-20 \le k \le 20$, $-15 \le l \le 15$	$-18 \le h \le 18$, $-18 \le k \le 18$, $-15 \le l \le 15$
Reflections collected	21415	19970
Independent reflections	3916 [R(int) = 0.1121]	945 [R(int) = 0.6546]
Completeness to theta = 24.000º (%)	99.7	99.5
Absorption correction	Semi-empirical from equivalents	Simi-empirical from equivalents
Max. and min. transmission	0.993 and 0.968	0.946 and 0.779
Refinement method	Full-matrix least-squares on F^2	Full-matrix least-square on F^2
Data / restraints / parameters	3916 / 240 / 350	945 / 164 / 89
Goodness-of-fit (F^2)	1.524	2.139
Final R indices [I>2sigma(I)]	$R_1 = 0.1508$,[a] $wR_2 = 0.4058$[b]	$R_1 = 0.3209$,[a] $wR_2 = 0.6236$[b]
R indices (all data)	$R_1 = 0.2024$,[a] $wR_2 = 0.4361$[c]	$R_1 = 0.3567$,[a] $wR_2 = 0.6388$[c]
Largest diff. peak and hole (e Å $^{-3}$)	0.952 and -0.943	2.173 and -1.335

III. Results and discussion

III.1. *De-novo* Synthesis of MOF

The azopy and bpa were used as pillaring linkers in **hms** structures. According to the precedent researches, certain ligands of MOFs including nitrogen exhibit a good property for capture CO_2 gas due to the attraction ability comparing to similar structures which are not including nitrogen.[72] The ligand, azopy contains two amine sites for improving the attraction between the structure and CO_2 gas. In the case of bpa, which contains a rigid triple bond, is longer than bipy. Therefore it is expected to build MOFs with large pore and surface area systematically.

The **azo-hms** and **bpa-hms** are prepared *via* conventional solvothermal reaction with modification of solvents and precursor ratio from the reported synthetic procedures.[38] Both of two crystals have the same stacked 2-dimensional layers consisted with nickel (II) metal and BTC ligand with 3,5-connect **hms** topology. The difference between two structures is the lengths of azo ligand and bpa ligand coordinated to metals, which are 13.079 Å and 13.764 Å, respectively. Therefore, the structures of **azo-hms** and **bpa-hms** have similar solvent accessible porosity, 64.2 % and 66.5 %, respectively. They possess larger porosity than **hms** topology pillared with bipy does, 49 %. Moreover, the noticeable structural difference between two **hms** structures is the alignment of metal place which is related with a shape of pillaring linker. Azopy ligand does not align in a line due to the tilted two amine functional groups and flexibility (Figure 3-1). According to the PXRD patterns, as-synthesized crystals were confirmed with simulated PXRD patterns from the corresponding single-crystal models. (Figure 3-2) Also the proton nuclear magnetic resonance (NMR) was used to assign the ligand ratio consisting the frameworks. Each crystals were decomposed in 0.6 mL deuterium chloride solution; DCl, and then the **azo-hms** crystal was dissolved in deuterium oxide; D_2O and the **bpa-hms** was dissolved in dimethyl sulfoxide-d6; DMSO. As shown in figure 3-3, the ligand ratio was determined as 1 to 1 by the proton ratio as BTC (3) : pillaring linker (4).

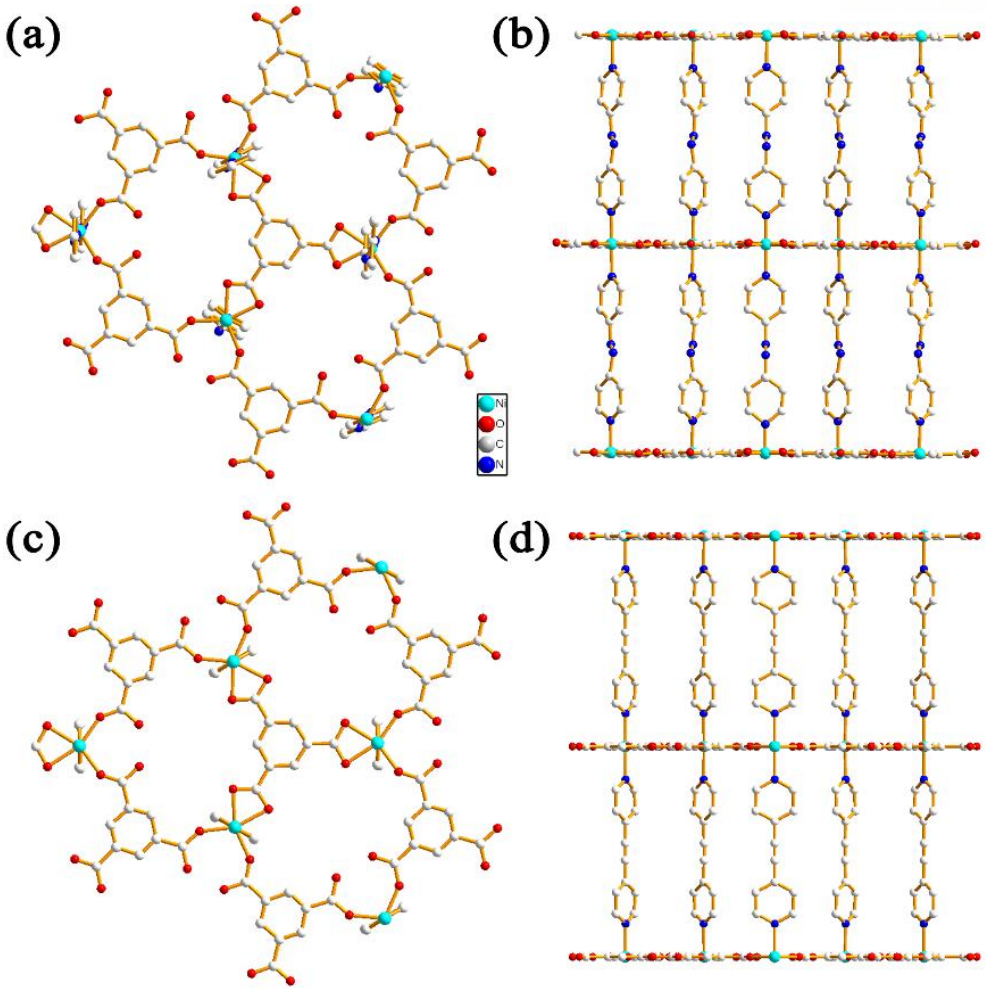

Figure 3-1. Crystal structures of **azo-hms**: (a) top view of the structure as a ball-and-stick diagram, (b) side view of the structure as a ball-and-stick diagram and **bpa-hms:** (c) top view of the structure as a ball-and-stick diagram, (d) side view of the structure as a ball-and-stick diagram. Color scheme: C, gray; O, red; N, blue; and Ni, cyan.

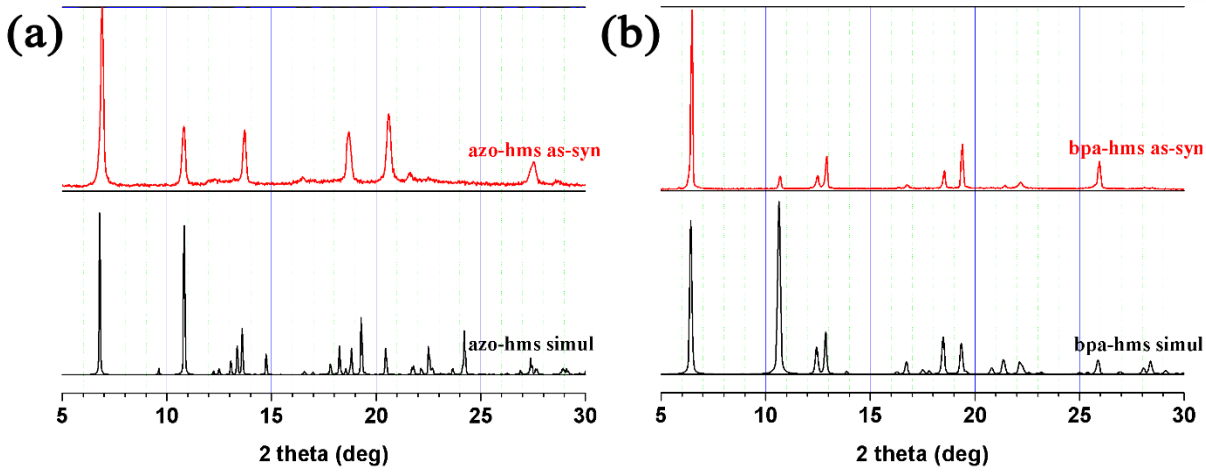

Figure 3-2. PXRD patterns of (a) as-synthesized **azo-hms** (red) and its simulated PXRD patterns from the corresponding single-crystal structure model (black) and (b) as synthesized **bpa-hms** (red) and their simulated PXRD patterns from the corresponding single-crystal structure model (black).

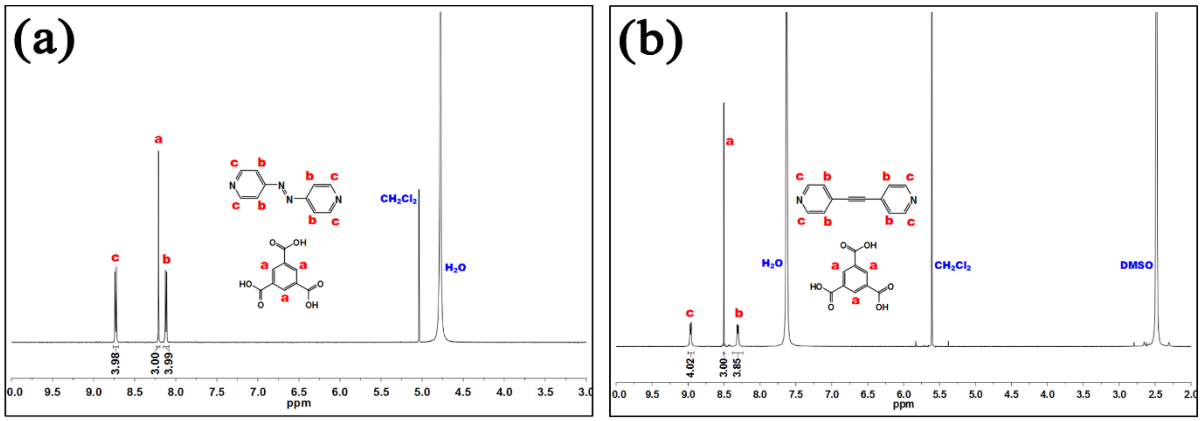

Figure 3-3. NMR analysis of (a) **azo-hms** and (b) **bpa-hms**

To evaluate the thermal stability of **azo-hms** and **bpa-hms**, a TGA apparatus was used. The solvent of synthesized crystals were exchanged from DMF to MC completely. After then, the crystals dried under the air atmosphere for an hour and N_2 for 10 minutes. Figure 3-4 shows the thermogram of the **azo-hms** and **bpa-hms** measured at a heating rate of 5 ºC min^{-1}. The **azo-hms** indicates that free guest molecules are removed below 150 ºC and a weight loss of 20 % was observed from ambient temperature to 300 ºC in the TG analysis, corresponding to solvent accessible pores (Figure 4-4. black). In a case of the **bpa-hms**, a weight loss of 24 % was observed, which indicates the free guest molecules removed completely below 150 ºC and no further weight loss was observed up to 320 ºC in the TG analysis (Figure 4-4. red). The weight loss results of **azo-hms** and **bpa-hms** were corresponding to the solvent accessible pores due to the lengths of pillaring linkers.

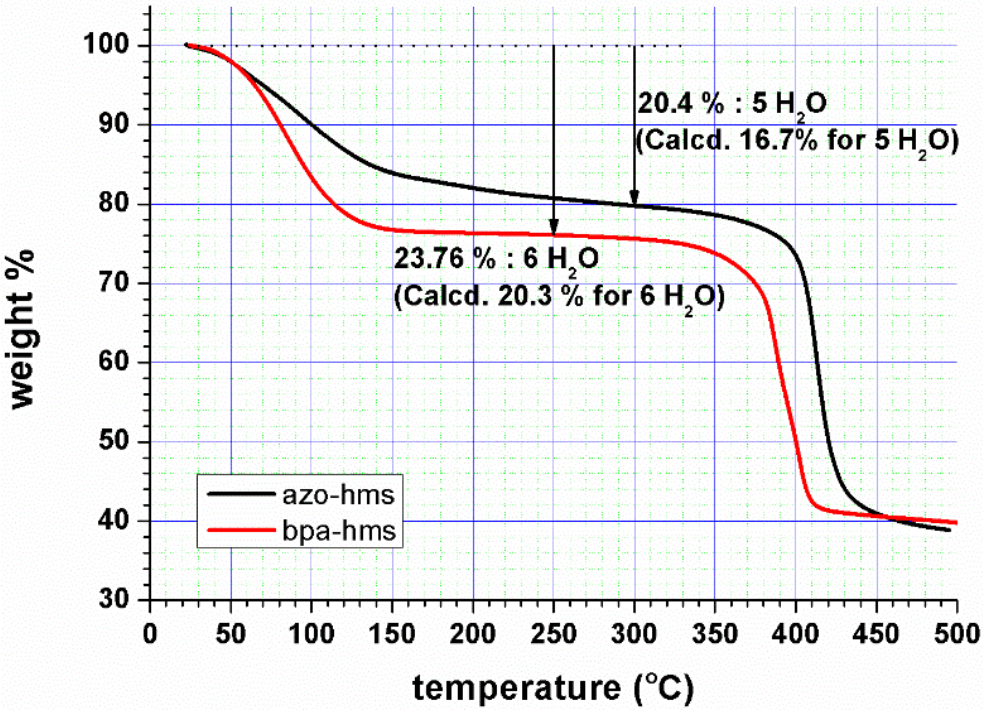

Figure 3-4. TGA traces of **azo-hms** (black) and **bpa-hms** (red).

Furthermore, we measured the N_2 sorption behavior of **azo-hms** and **bpa-hms** to determine the porosity (Figure 3-5). As the introduced linkers in the new **hms** frameworks were longer than **bipy-hms** which uptakes about 500 cm^3/g, the amount of N_2 gas adsorption of **azo-hms** is 510 cm^3/g and that of **bpa-hms** is 639 cm^3/g. The BET surface area of **azo-hms** is 1910.2 m^2/g and that of **bpa-hms** is 2460.9 m^2/g. Meanwhile as shown in figure 3-6, in the cases of CO_2 gas sorption at 273 K and 298 K, the **azo-hms** uptakes more gases than the **bpa-hms** structure regardless of the limitation of the porosity in the frameworks. The **azo-hms** uptakes CO_2 gas 136 cm^3/g and **bpa-hms** uptakes 86 cm^3/g at 273 K. In the cased of CO_2 adsorption at 298 K, the **azo-hms** and **bpa-hms** uptake 71 cm^3/g and 46 cm^3/g, respectively. These interesting results are derived from the interaction between frameworks and gas molecules, because the adsorption amount of CO_2 gas is significantly related with the attraction of polarization and the pore size of frameworks than absolute porosity at ambient condition. The reason why **azo-hms** seems more efficient for CO_2 capture ability than **bpa-hms** is the azo functional groups in pillaring linkers. However two hms-MOFs have similar adsorption enthalpy at these experimental results by virial theory (Figure 3-7).

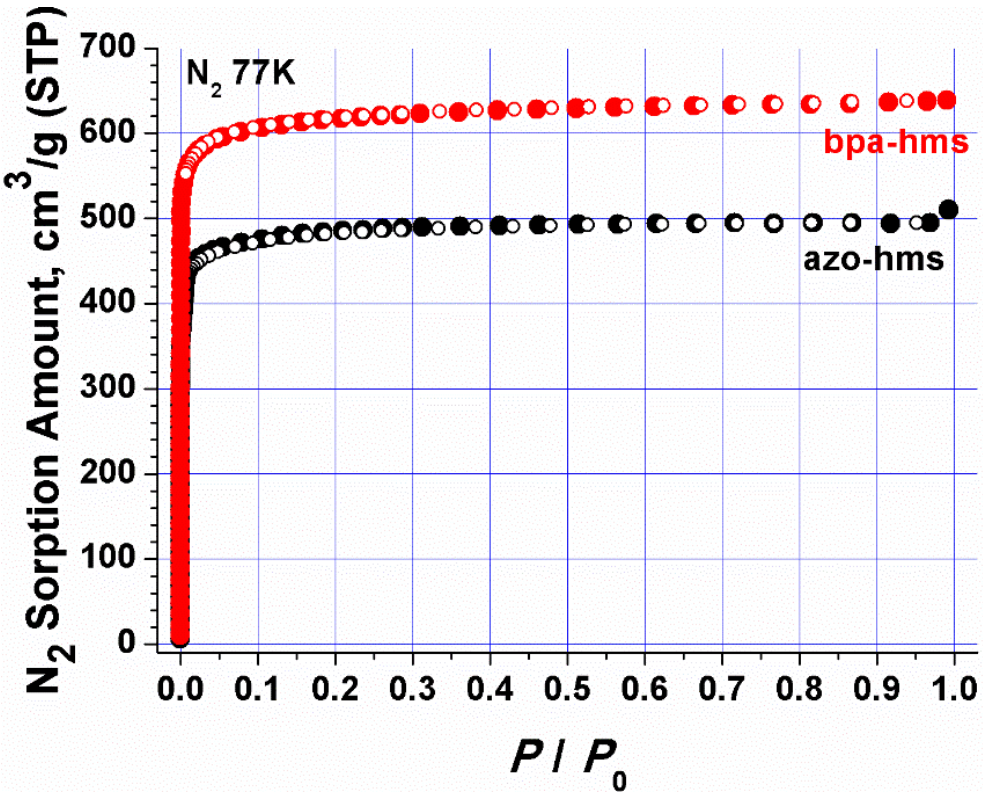

Figure 3-5. N_2 sorption behavior (77K) of **azo-hms** (black) and **bpa-hms** (red).

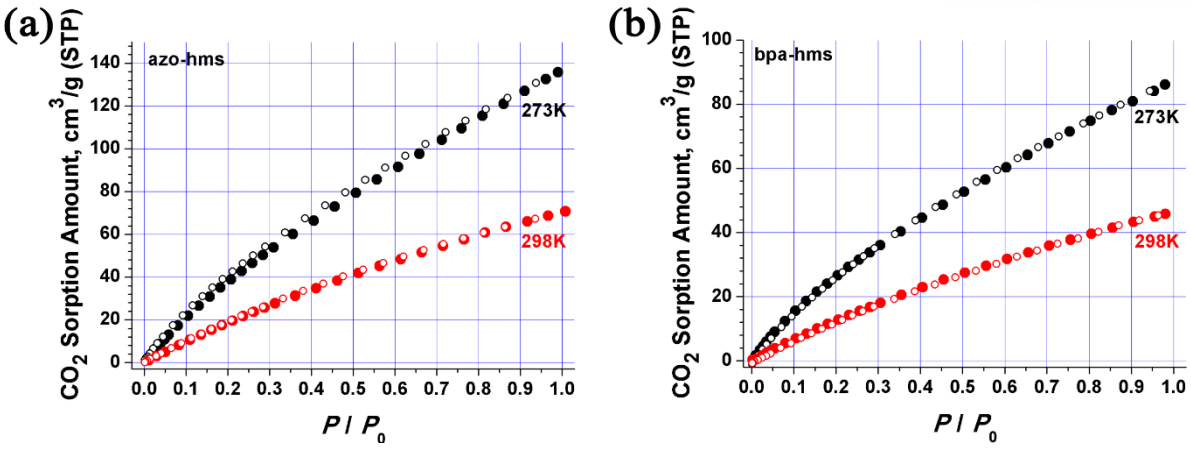

Figure 3-6. CO_2 sorption behavior of (a) **azo-hms** at 273 K (black) and 298 K (red) and (b) **bpa-hms** at 273 K (black) and 298 K (red).

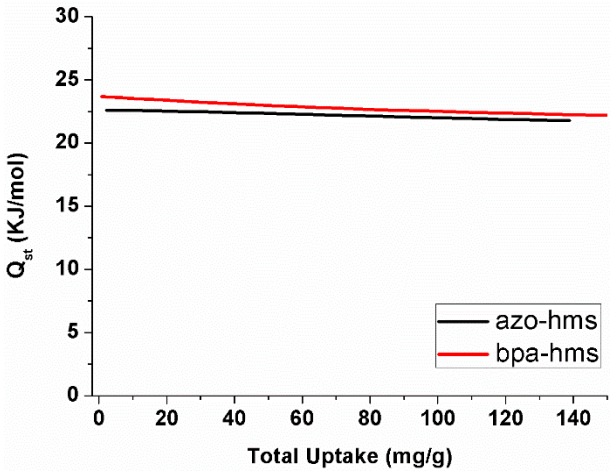

Figure 3-7. Adsorption enthalpy of **azo-hms** (black) and **bpa-hms** (red).

Thermal Analysis and Powder X-ray Diffraction

The crystallinities at elevating temperature was measured, with aging for an hour. The VT-PXRD seemed that both of the **azo-hms** and **bpa-hms** crystals undergo structural changes. As shown in figure 3-8b, **bpa-hms**, the (*002*) and (*004*) peaks are broaden at 50 ~ 100 ºC *via* intermediates, after then, going to be sharpen. According to the figure 3-8, the PXRD peaks, such as (*001*), (*002*), (*003*), and (*004*) meaning *c*-axis, change significantly than any other peaks. The peaks indicating (*001*) and (*003*) are going to disappear and the peaks (*002*) and (*004*) are going to strengthen as temperature increase up to 300 ºC. Based on these experimental phenomena, we hypothesized the contraction of 2-dimensional layers, not simply desolvation of solvents in pores. Therefore, we focused on heated MOFs in depth continuously and more additional characterization was operated.

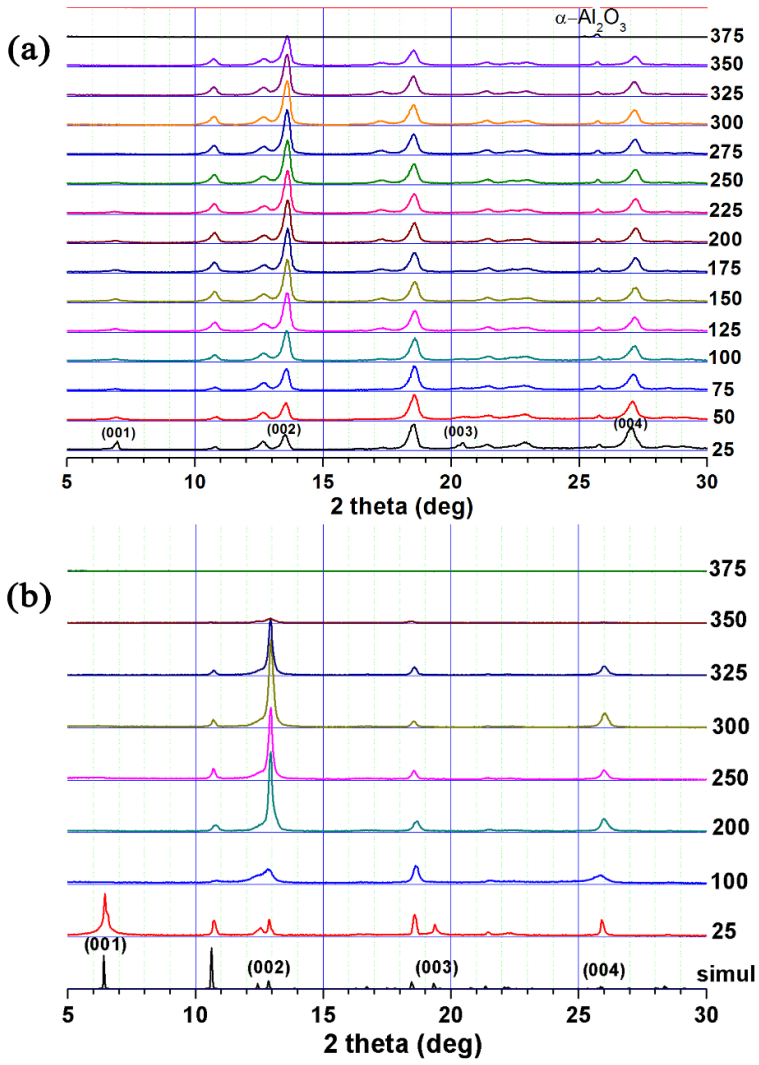

Figure 3-8. VT-PXRD patterns at elevating temperatures (a) as-synthesized **azo-hms** and (b) as-synthesized **bpa-hms**.

III.2. Solvent-Assisted Interpenetrated MOFs

In MOFs prepared by conventional methods, the frameworks are built by coordination bonds between metal nodes and organic ligands. In certain crystal cases, the coordinative solvents also participate to bind with metal nodes *via* coordination bonds, as well. The MOFs with **hms** topology of [Ni(HBTC)(L)] do not bind directly with solvent; however, the metal nodes in networks attract free solvents at axial direction. Therefore, the free solvents can participate the network-binding system in the way to assist to modify the construction, since the free solvents play a role as a bridge between metal nodes and neutral pillaring linkers reducing a binding activation energy. For these reasons, the **hms** MOFs with coordinative solvents environment can transform into 2-fold catenated **hms** MOFs (**hms-c**) in the particular thermal condition (Figure 3-9A).

Meanwhile, the **hms** MOFs with non-coordinative solvents environment cannot modify an activation energy of bindings between metal nodes and pillaring linkers. Therefore, the **hms** MOFs with non-coordinative solvents environment generate defects in the structures at the same thermal condition, because neutral pillaring linkers placing at axial sites of metal ions are evaporated from the metal nodes, keeping the 2D **hcb** sheets which is built with charges. Consequentially, we obtained defect generated **hms** MOFs (Figure 3-9B).

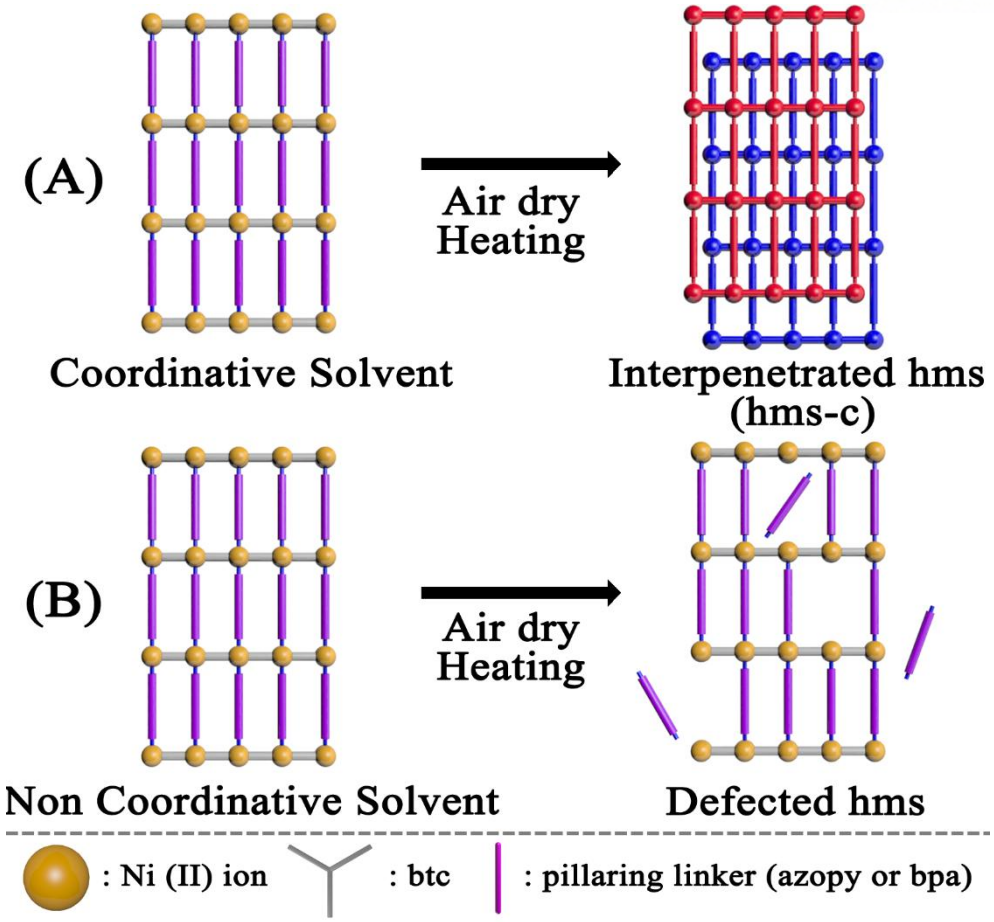

Figure 3-9. Scheme of solvent assist interpenetration. A case of **hms** crystals with coordinative solvent (A) and a case of **hms** crystals with non-coordinative solvent (B).

To catenate the structures from **hms** topology to **hms-c**, it is important to adjust the thermal temperature regarding different neutral linkers. To optimize the temperature, the TGA results of two crystals were considered. At first, **azo-hms** decomposes from 280 ºC; it means neutral azopy between 2-dimensional sheets is not durable at high temperature above 300 ºC. Therefore, the moderated thermal condition for interpenetration is 250 ºC for two hours under N_2 atmosphere (**azo-hms-c**). In the case of harsh condition, the unexpected defects are generated in **azo-hms-c** frameworks as a result of the evaporated neutral pillaring linker; azopy. Meanwhile, according to the TG analysis, **bpa-hms** keeps the crystallinities at 320 ºC. Therefore, the heat treatment for **bpa-hms** was at 300 ºC for an hour under N_2 condition to form a catenated structure (**bpa-hms-c**) with any pillaring linker missing.

Description of catenated structure (hms-c)

Most of all, the X-ray studies reveal that **hms-c** MOFs had 3-dimensional two independent frameworks interpenetrated while their backbone connectivity is identical to that of **hms** MOFs. The thicknesses of **azo-hms-c** and **bpa-hms-c** contracted to 6.60 Å and 6.85 Å from 13.08 Å and 13.75 Å, respectively. The distances are well-fitted with the half of distances from original **hms** MOFs. Also the structures of **azo-hms-c** and **bpa-hms-c** have different solvent accessible porosity as 16.4 % and 28.1 %, respectively. The porosities are lower than expected halves of the porosity of original **hms** MOFs because of the ligand flexibility and their functional groups (Figure 3-10). Moreover the powder X-ray diffraction patterns of **hms-c** MOFs prepared by the heat treatment match to their simulated patterns from the single-crystal structure models (Figure 3-11 (a) and (b)).

To investigate the solvent accessibility in interpenetrated frameworks, the TGA apparatus was performed on the each **hms-c** MOFs. Before the analysis, the crystals were soaked in DMF solvents for a day and then dried under ambient atmosphere for an hour. As shown in figure 3-11 (c) and (d), the interpenetrated **hms-c** MOFs have very little accessible solvent molecules in the pores comparing **hms** MOF, ~ 4 % and ~ 6 %, respectively considered as excess DMF and H_2O.

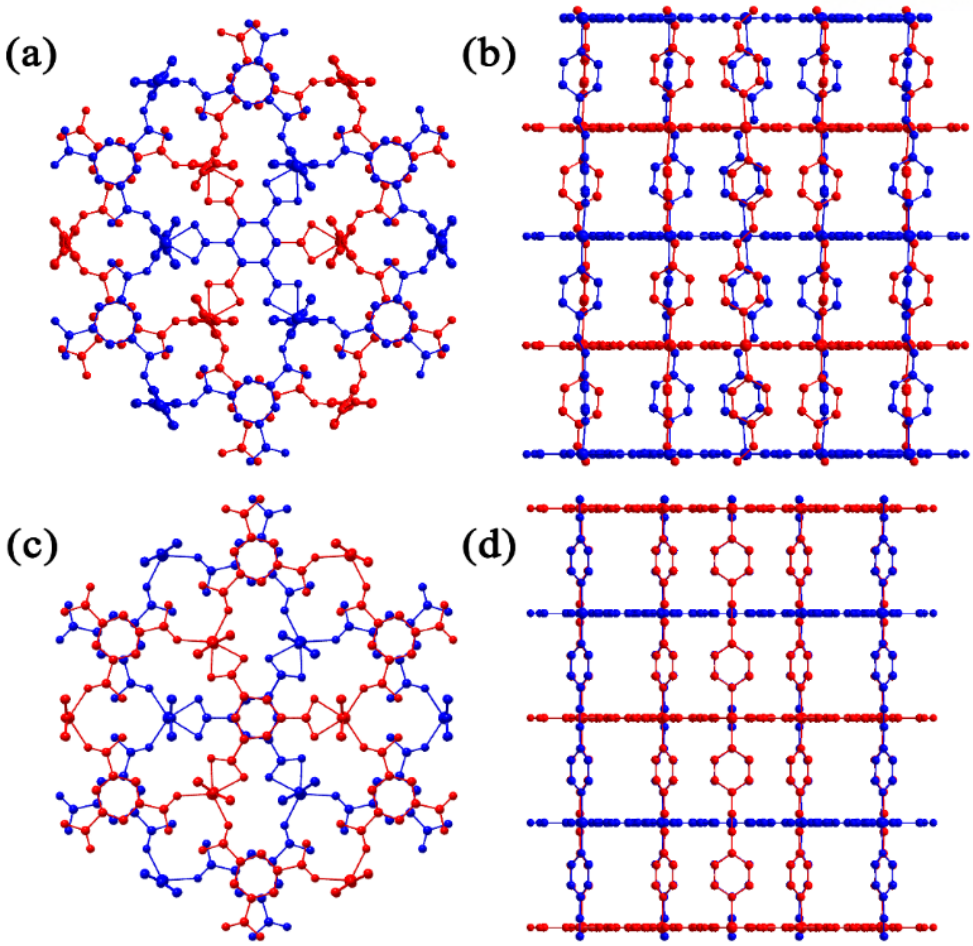

Figure 3-10. The structure of **azo-hms-c** (a) top view, (b) side view and **bpa-hms-c** (c) top view, (d) side view.

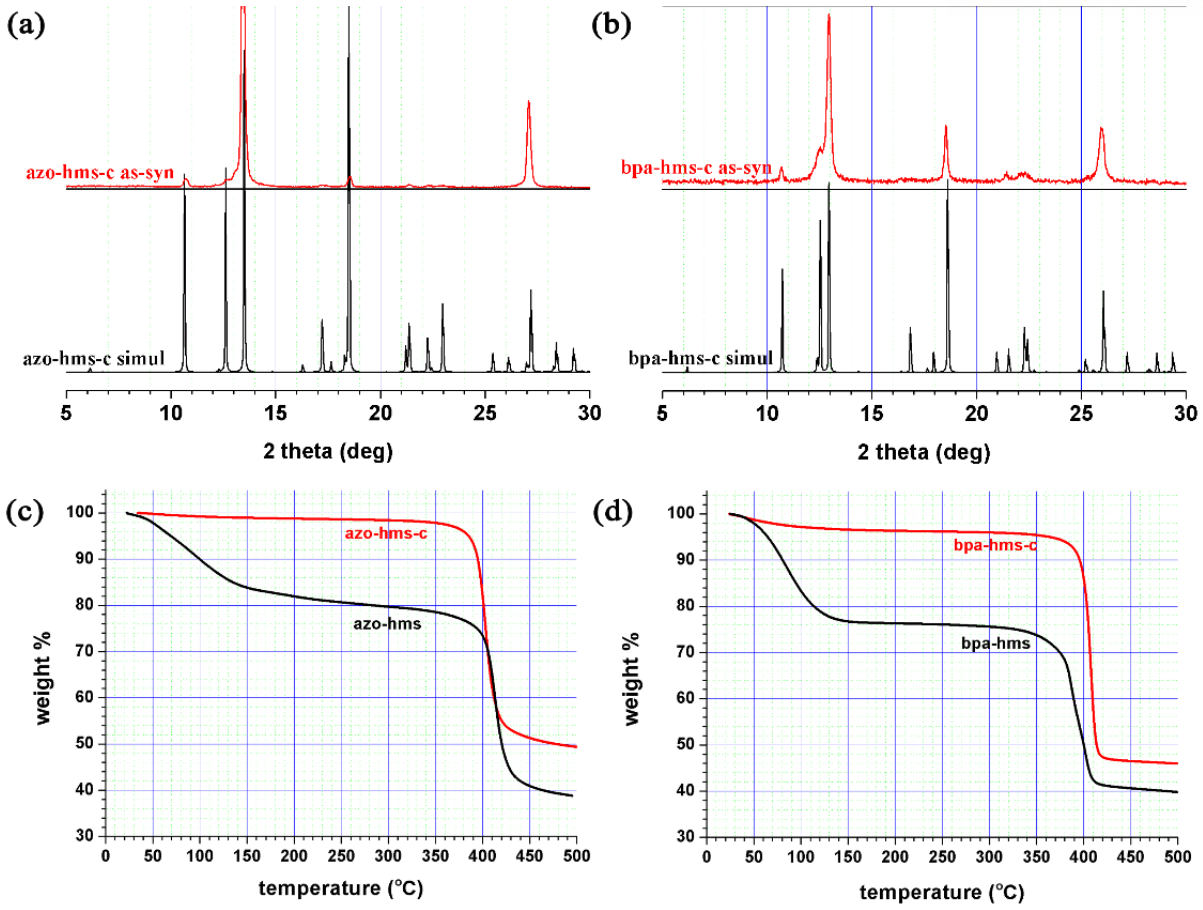

Figure 3-11. (a) PXRD patterns of **azo-hms-c** (red) and the simulated PXRD patterns from the corresponding single-crystal structure models (black), (b) PXRD patterns of **bpa-hms-c** (red) and the simulated PXRD patterns from the corresponding single-crystal structure models (black), (c) TGA traces of **azo-hms-c** (red) and **azo-hms** (black), (d) TGA traces of **bpa-hms-c** (red) and **bpa-hms** (black).

During interpenetrating process, the defects can be generated by missing pillaring linkers due to the heat treatment to the frameworks. To confirm the remained ligands in frameworks, the proton NMR was used. According to the ^{1}H NMR spectroscopy result, figure 3-12a, the proton ratio of azopy to BTC is 3.9 : 3 and the result identifies a maintenance of azopy linker in frameworks. Also the figure 3-12b shows bpa-hms-c have a proton ratio of bpa to BTC, 4 : 3, and the data explains the neutral bpa pillar is not evaporated during thermal treatment.

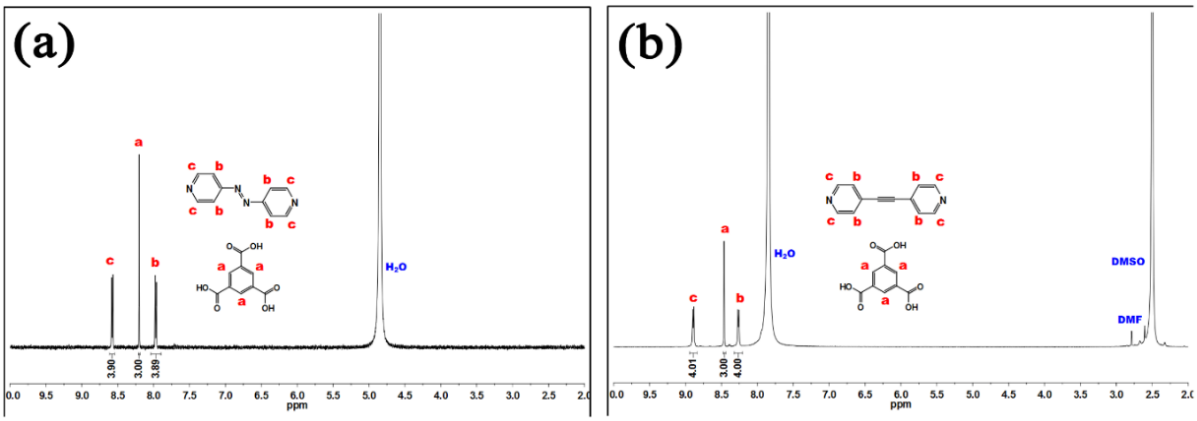

Figure 3-12. NMR analysis of **azo-hms-c** and **bpa-hms-c**.

To characterize the pore size of interpenetrated structure precisely, N_2 gas sorption and pore size distribution analysis by DFT and PSD fitting was used. In a study of gas sorption, the N_2 uptake amount reduced from 500 cm^3/g, **azo-hms** to 120 cm^3/g, **azo-hms-c**. And the sorption amount of **bpa-hms-c** was 110 cm^3/g from 630 cm^3/g, **bpa-hms** (Figure 3-13). The flat sorption behaviors after the microporous sorption region indicate that there are any notable mesopores in the structures according to a sorption behavior type I. The surface area of interpenetrated structures are 431.88 cm^3/g for **azo-hms-c** and 449.28 cm^3/g for **bpa-hms-c**. The pore size distribution also guarantees the pores were formed homogeneously by solvent-assisted complete interpenetration process. The pore size of **azo-hms-c** is 5.5 Å from that of **azo-hms**, 7.0 Å. The pore size of **bpa-hms-c** is 5.6 Å from that of **bpa-hms**, 7.2 Å (Figure 3-14).

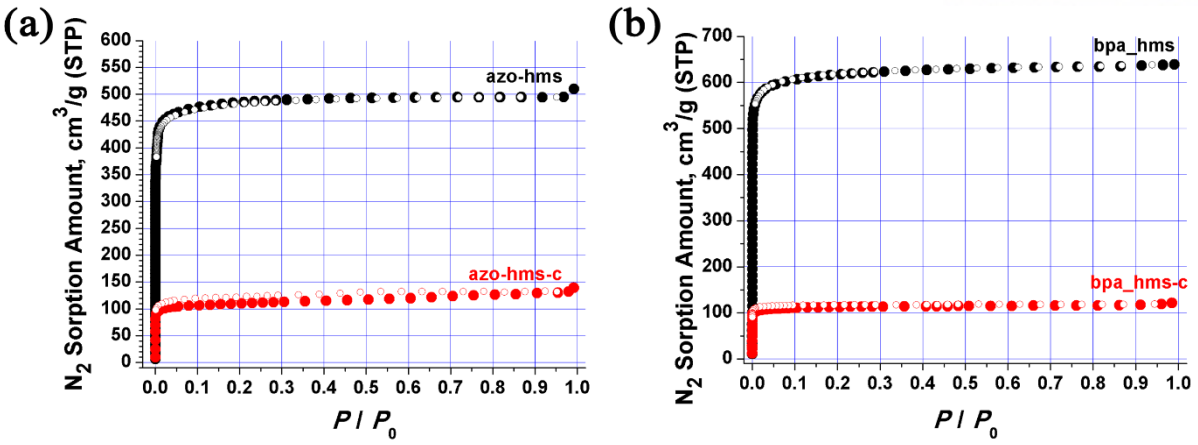

Figure 3-13. N_2 sorption behavior (77K) of (a) **azo-hms** (black), **azo-hms-c** (red) and (b) **bpa-hms** (black), **bpa-hms-c** (red).

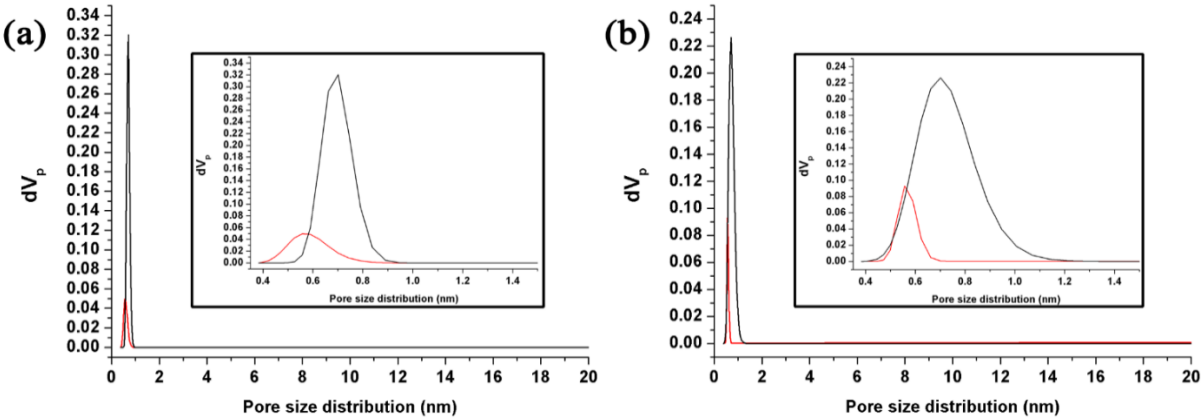

Figure 3-14. Pore size distribution of (a) **azo-hms** (black), **azo-hms-c** (red) and (b) **bpa-hms** (black), **bpa-hms-c** (red).

Table 3-1. The crystal density, Q_{st} for CO_2, thermodynamic CO_2 and N_2 uptake for activated **azo-hms, azo-hms-c, bpa-hms, and bpa-hms-c**.

MOF	Crystal density ($cm^3\ g^{-1}$)	Q_{st} for CO_2 (KJ mol^{-1})	CO_2 uptake at 273 K ($cm^3\ cm^{-1}$)	CO_2 uptake at 298 K ($cm^3\ cm^{-1}$)	N_2 uptake ($cm^3\ g^{-1}$)
azo-hms	0.743	22.61	135.74	70.744	510.14
azo-hms-c	1.432	33.08	49.848	36.432	139.38
bpa-hms	0.677	23.70	86.055	45.816	638.75
bpa-hms-c	1.379	34.37	53.711	37.5	121.37

In the case of CO_2 gas sorption, the amount of uptakes are about 49.85 cm^3/g for **azo-hms-c** and 53.71 cm^3/g for **bpa-hms-c** at 273 K, respectively. At 298 K, the amounts of uptake CO_2 are 36.43 cm^3/g for **azo-hms-c** and 37.50 cm^3/g, respectively (Figure 3-15). The interesting experimental results are the adsorption curves of interpenetrated structures. Although the saturated gas uptake amounts due to the limited porosity, the adsorption amounts at low pressures (~ 0.2 P/P_0) are increased extremely comparing to the non-interpenetrated hms-MOFs. Since the CO_2 gas molecules is significantly related with the attraction between framework and gas molecules which is affected with the size of accessible pore size. Therefore, the results indicate that the pore size of interpenetrated structures is more predominant than that of non-interpenetrated structures. Also the adsorption heat enthalpy supports the experimental results (Figure 3-16).

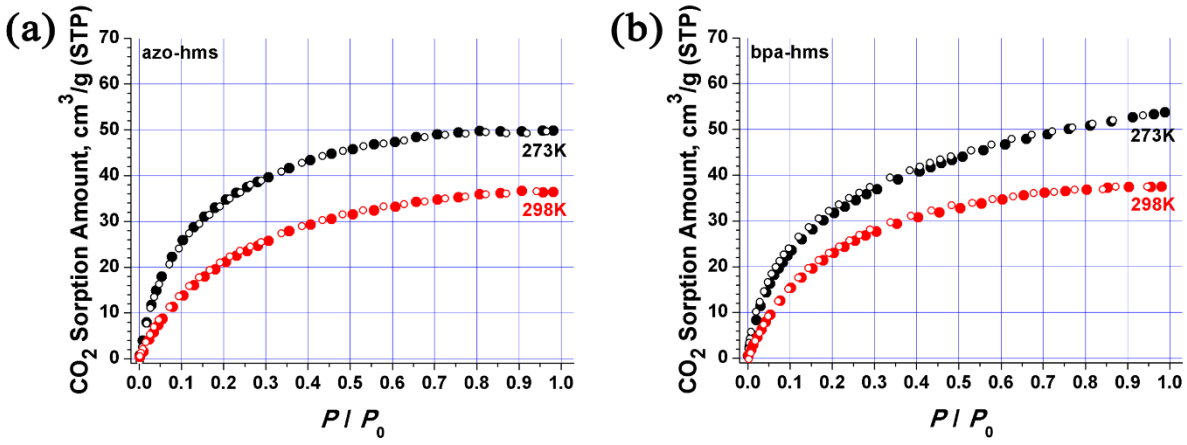

Figure 3-15. CO_2 sorption behavior (273K & 298K) of (a) **azo-hms-c** and (b) **bpa-hms-c.**

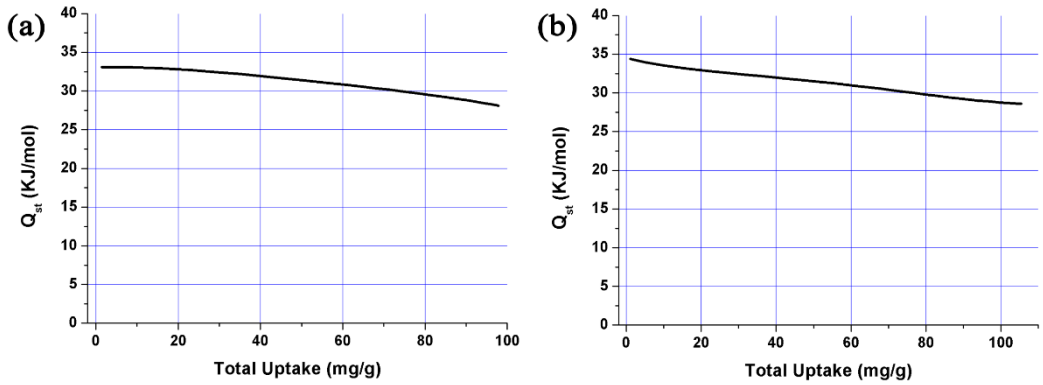

Figure 3-16. Adsorption enthalpy of **azo-hms-c** and **bpa-hms-c**.

According to the several reported results, interpenetrated structures could enhance the stability and tune the pore size for selectivity of specific molecules. On the other hands, the interpenetrated MOFs are not suitable for commercialization. They could not take the most attractions of MOFs such as large surface area and porosity. To compensate the weakness of interpenetrated MOFs, we attempt to take defect-engineering strategy to generate the intended defects of MOFs.

Attempt To generate defect at MOFs by the Conventional Approach.

While the solvothermal reaction of H_3BTC with ~ 1.2 equivalent of Ni (II) ion in DMF at 60 ºC or 70 ºC for 3 days in the presence of an equivalent amount of pillaring linkers of azopy and bpa, respectively, it led to form the 3-D MOFs with a 3,5-connected **hms** net topology.[73] A similar solvothermal reaction with 0.3 ~ 0.7 equivalent of pillaring linkers produced a mixture of the **hms** net topology and the reported 2-D MOFs, $[Ni(HBTC)(DMF)_2]$ (2D-simul), where the 2D sheets of the MOFs made of Ni (II) ion and HBTC ligand are the same as those of **hms**, but the 3-connected nickel centers of an **hcb** net topology are ligated with two additional monodentate DMF molecules (Figure 3-17).

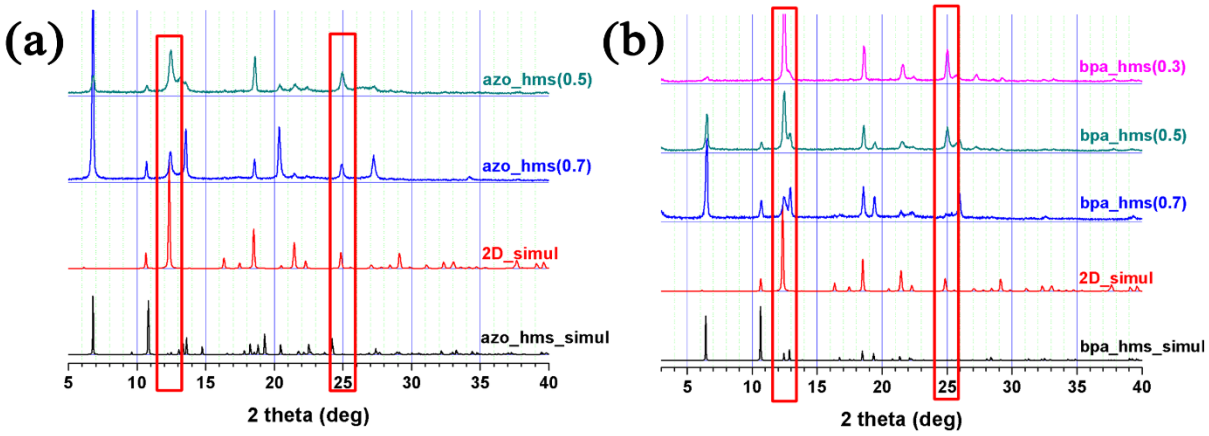

Figure 3-17. PXRD pattern of **azo-hms** and **bpa-hms** synthesized with controlled linker ratio (0.7, 0.5 and 0.3 equivalents).

III.3. Defect Engineered MOFs *via* Linker Extraction

Recently, hierarchical porous MOFs are researched interestingly for utilizing various pore sizes in MOFs. According to already reported papers, there are several methods to explore hierarchical pores using mixed components with fragments [74], controlled acid amounts [75], or PSM [53].

Herein, we used an opposite way of a solvent-assisted interpenetration phenomena of **hms** topology. As mentioned earlier, the hms-MOFs generate defects by extraction of neutral pillaring linkers between 2D sheets under the high temperature conditions in the non-coordinative solvent environment. Furthermore, we are able to modify the amounts of defects systematically by control the heating temperature and aging time. It will encourage us to introduce suitable defects depending on the aimed porosity.

The most difference with interpenetration is the environmental condition whether the free solvent can coordinate to metal ions. Therefore first of all, the **hms** frameworks exchange solvent with MC (**A**) until remove the DMF solvent completely because MC is not coordinative to metal ions in frameworks. After then, the crystals were heated in the thermal vacuum system at a specific temperature and time. The heated samples were washed with fresh MC solvent several times and sonicated sufficiently to remove resident linkers in pores (**B**). The resident amount of pillaring linkers coordinated with metal is confirmed by ^{1}H NMR spectroscopy; the proton ratio of pyridine ligand ratio to BTC ligand. Based on these results in various conditions, we identified an extraction tendency of neutral pillaring linker depending on the different kinds of linkers (Figure 3-18. **A** → **B**).

After generating DEMOFs by pillaring linker extraction, the DEMOFs were soaked in DMF for a day (**B'**) and air-dried at ambient condition for an hour to promote solvent-assist interpenetration. Then, crystals were heated under N_2 environment to prepare interpenetration. The prepared crystals are defect-engineered interpenetrated **hms** (**hms-d**, **C**). It is important to guarantee no missing pillaring linkers in this second process to prevent unexpected defects. Therefore, we confirm pyridine proton ratio to BTC proton in ^{1}H NMR of results again by ^{1}H NMR spectroscopy. The crystallinity of **hms-d** with defects maintains, and there is no difference with the simulated pattern of **hms-c** single data (Figure 3-18. **B'** → **C**).

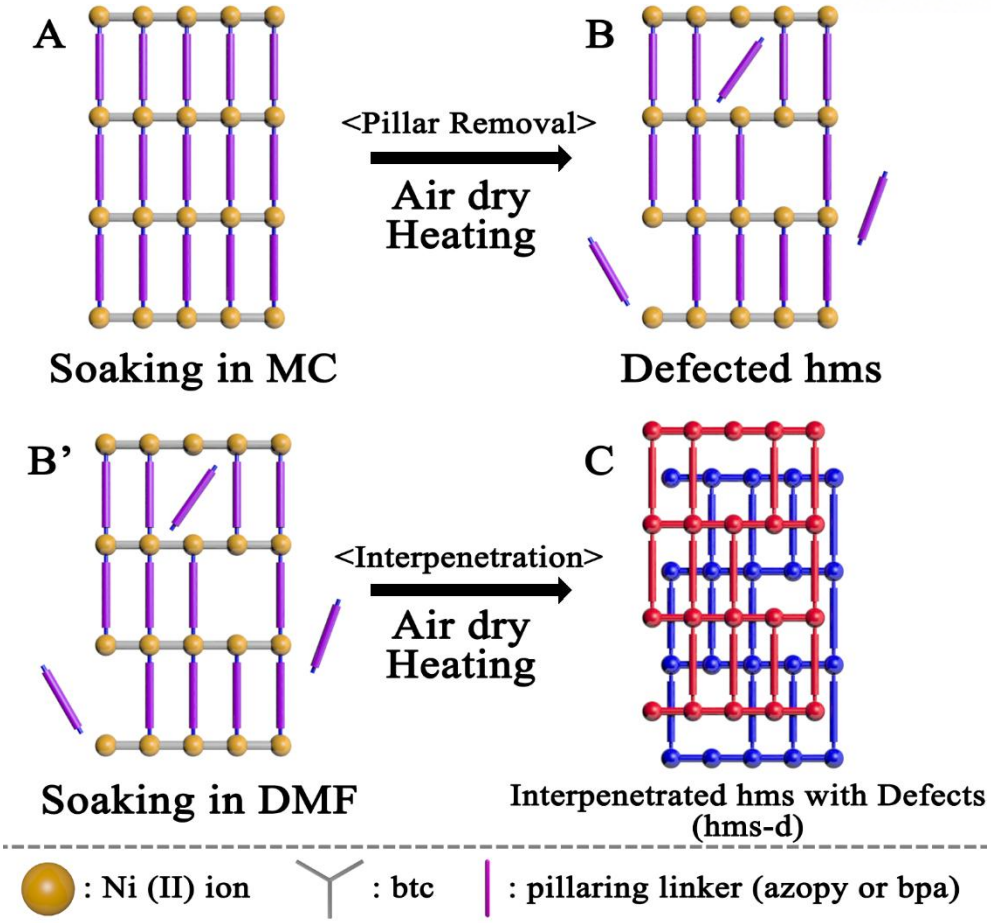

Figure 3-18. Scheme of interpenetration MOF with defect. **A** → **B** → **B'** → **C**.

Description of defect-engineered interpenetrated structure (hms-d)

We applied various thermal temperature from 170 ºC to 250 ºC to extract neutral pillaring linkers, azopy and bpa. The temperature below 200 ºC is not enough to extract linkers, and in that above 250 ºC, the crystals cannot maintain the crystallinity. Although the range from 220 ºC to 250 ºC is acceptable for extracting pillaring linker, however crystallinity of frameworks decompose rapidly as keeping temperature time. Since the tunability of amount of resident linkers and the crystallinity of samples in enough mild thermal condition, we adopt the 220 ºC as an appropriate evaporating linker temperature for both of the **azo-hms** and the **bpa-hms**. After removing pillaring linkers in hms-MOFs, the crystals are soaked in fresh DMF solvents to dilute resident linkers in pores of frameworks and interpenetrate the defected samples. The defected crystals can interpenetrate in the same manner of interpenetration method of **azo-hms-c** and **bpa-hms-c**. The prepared crystals are the **hms-d**.

In both of the **azo-hms-d** and the **bpa-hms-d**, the defects are generated as crystals are heated at 220 ºC for various time. The hms-MOFs with extracted pillaring linkers are analyzed from an hour to a day. The amount of resident neutral pillaring linkers are investigated by the ^{1}H NMR spectroscopy analysis, comparing with BTC ligand which consists the robust 2-D sheets above 300 ºC. As mentioned before, the ratio of conventional pillaring linker; azopy or bpa to BTC is 4 to 3. According to the ^{1}H NMR spectroscopy analysis, the amount of resident azopy linker in network is decreased for several times and saturated after maintaining 3 hours under the thermal vacuum system. On the other hand, the resident amount of bpa pillaring linkers in framework is decreased; the decreasing pace is first rapid, then slowed in activity during heating crystal samples in vacuum condition (Figure 3-19). Also the PXRD patterns as the heating time indicates the crystallinity of the defected MOF. The structure of **azo-hms-d** maintains the crystallinity despite heating for 1 day under the harsh condition. However, the crystallinity of **bpa-hms-d** get worse rapidly as aging the time in thermal condition (Figure 3-20).

(a)

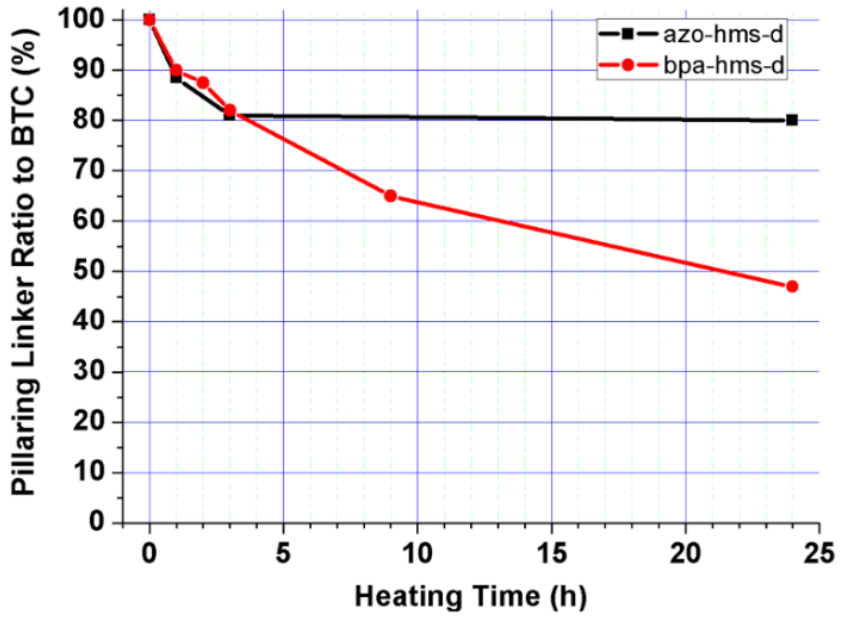

(b)

Heating 220 °C	1 h		3 h	24 h	
BTC : azopy	3 : 3.54		3 : 3.23	3 : 3.21	
azopy (%)	88.5		81	80	
Heating 220 °C	1 h	2 h	3 h	9 h	24 h
BTC : bpa	3 : 3.6	3 : 3.5	3 : 3.29	3 : 2.6	3 : 1.88
bpa (%)	90	87.5	82	65	47

Figure 3-19. (a) The pillaring linker ratio comparing to BTC depending on the various heating temperatures of **azo-hms-d** (black) and **bpa-hms-d** (red); (b) The table of pillaring linker ratio comparing to BTC depending on the various heating temperatures; **azo-hms-d** at 220 ºC and **bpa-hms-d** at 220 ºC determined by NMR spectroscopy

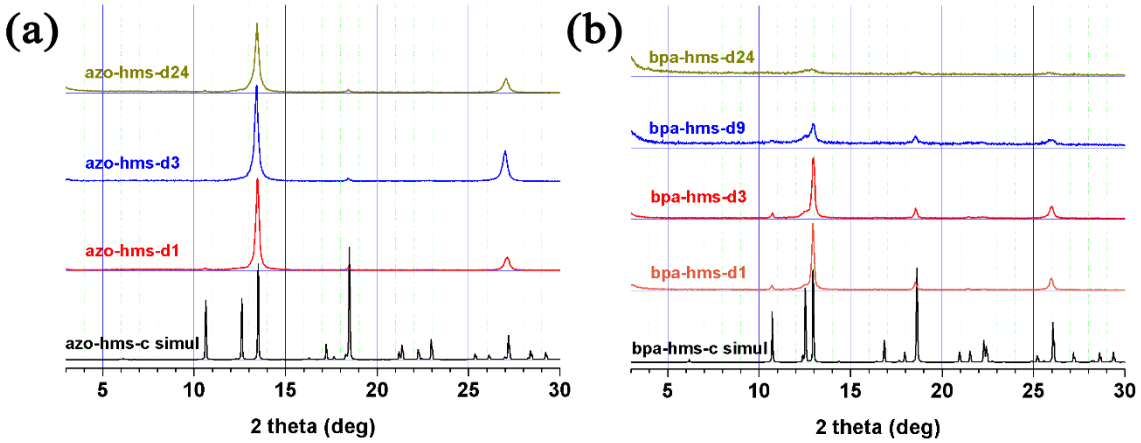

Figure 3-20. PXRD pattern of (a) **azo-hms-d** and (b) **bpa-hms-d** depending on thermal aging time; **azo-hms-da** (a : aging time; 1, 3, 24 hours) **bpa-hms-db** (b : aging time; 1, 3, 9, and 24 hours)

Both of the **azo-hms-d** and **bpa-hms-d** are investigated depending on the thermal aging time, respectively. The thermal aging time is marked behind of the samples name; **azo-hms-d1**, **azo-hms-d3**, **azo-hms-d24**, **bpa-hms-d3**, **bpa-hms d9**, and **bpa-hms-d24**. The **hms-d** MOFs shows interesting adsorption behaviors in N_2 sorption uptakes and the pore size distribution was calculated using NLDFT pore size distribution. In the series of **azo-hms-d**, the microporosity is almost maintaining and the additional porosities are generated easily. The lasting micropores indicates that the stability of azo-MOFs and it is confirmed as the PXRD patterns of **azo-hms-d** (Figure 3-20a). In the case of the mesopores, the pores are distributed around 35 Å. Moreover, the **azo-hms-d24** has exceedingly various size pores in its structure derived from extraction of pillaring linkers even though the amount of linker is similar with the **azo-hms-d3** (Figure 3-21b). Meanwhile, the **bpa-hms-d3** generates mesopores with considerable micropores as shown in Figure 3-22. Red line. As the aging time gets longer; **bpa-hms-d9** and **bpa-hms-d24**, the total amount of fragment is increased and the size of defect also increased. While the mean value of pore size distribution is not significantly affected depending on the variables of aging time. It seems to be that there is not any other defects except the empty pillaring linker place and the defects are well-dispersed in whole bpa-MOFs structures (Figure 3-22b).

The results indicates that the **hms-d** MOFs can control the amounts of various pores with different size; micro-, meso-, and macropores systematically which is called the hierarchical porous frameworks. The MOFs with hierarchical porosity are expected with potential application such as catalysts or selective adsorbent based on their pore size selectivity and superior transportation of molecules. Furthermore, the PSM method of preparing MOFs can be investigated valuably and introduced into other MOFs to improve their properties.

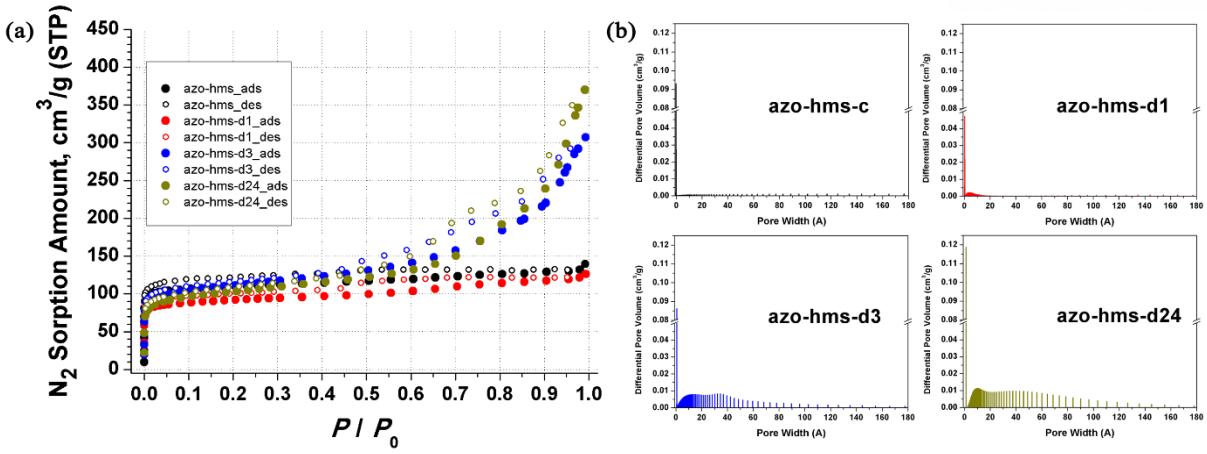

Figure 3-21. (a) Sorption behavior of **azo-hms-d**; (b) Pore size distribution of **azo-hms-d**; **azo-hms-c**, **azo-hms-d1**, **azo-hms-d3**, **azo-hms-d24**

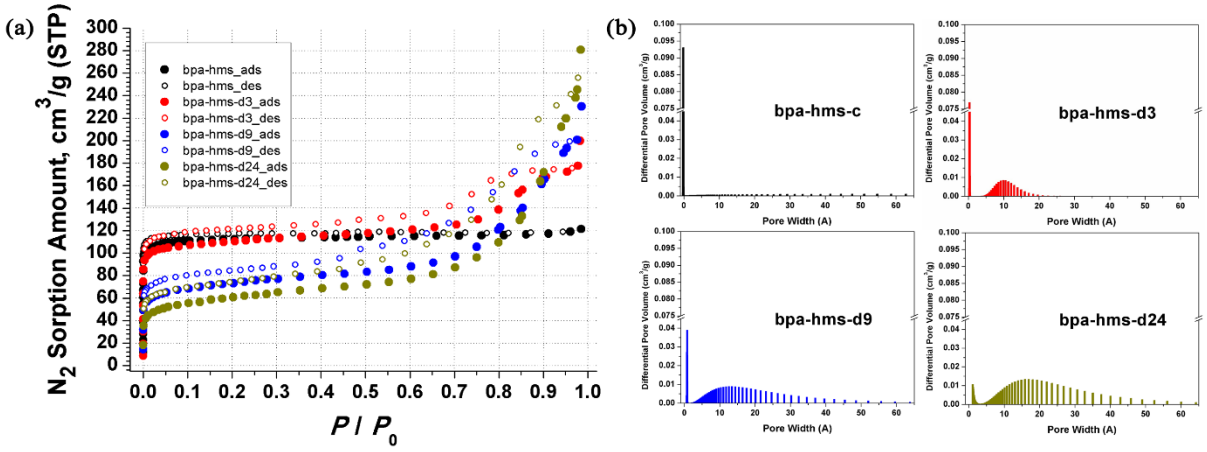

Figure 3-22. (a) Sorption behavior of **bpa-hms-d**; (b) Pore size distribution of **bpa-hms-d**; **bpa-hms-c**, **bpa-hms-d3**, **bpa-hms-d9**, **bpa-hms-d24**

Table 3-4. Amount of N_2 gas uptake of **azo-hms-d** and **bpa-hms-d** depending on thermal aging time; **azo-hms-da** (a : aging time; 1, 3, 24 hours), **bpa-hms-db** (b : aging time; 3, 9, 24 hours)

N_2 uptake (cm^3 g^{-1})	**hms-c**	**hms-d1**	**hms-d3**	**hms-d24**
azopy	139.38	126.27	307.12	369.89
N_2 uptake (cm^3 g^{-1})	**hms-c**	**hms-d3**	**hms-d9**	**hms-d24**
bpa	121.37	199.81	230.27	280.66

IV. Conclusion

The isoreticular MOFs with **hms** topology are synthesized with longer neutral pillaring linkers, azopy and bpa. The structures of **azo-hms** and **bpa-hms** were determined using single-crystal XRD, confirming that two MOFs have the same structure. In the case of **azo-hms**, the metal nodes of frameworks are not aligned due to the shape of ligand. Both of the crystals have larger porosity than other hms-MOFs reported before, due to the ligand length. Meanwhile, the **azo-hms** MOFs show the larger amount of CO_2 uptake than **bpa-hms** MOFs at room temperature even though the length of azopy is shorter than bpa. The result of sorption experiment is well fitted with the effect of amino groups for CO_2 adsorption which is related with the chemical interaction between the amino group and CO_2.

The thermogravimetric trace of hms-MOFs with longer neutral pillaring linkers indicates the transition of peak place slightly, and we found the interpenetrated frameworks with **hms** topology is found after the suitable heat treatments; for **azo-hms-c** at maintaining 250 ºC for 2 hours, and for **bpa-hms-c**, maintaining at 300 ºC for an hour. The structures of interpenetrated hms-MOFs were also determined using single-crystal XRD, confirming that two MOFs have the same structure. The porosity of **hms-c** MOFs is significantly reduced and the N_2 adsorption amount supports this results. However, the CO_2 adsorption behaviors of interpenetrated frameworks show unexpected results; adsorption amount of CO_2 molecules at low pressure (~ 0.15 P/P_0) is considerably increased than it of **azo-hms** and **bpa-hms** since reducing the pore size led the faster and greater CO_2 adsorption with frameworks under the same sorption condition.

According to the several reported results, interpenetrated structures were able to enhance the stability and tune the pore size for selectivity of specific molecules. On the other hand, the interpenetrated MOFs are not suitable for guest molecule storage and separation due to their low porosity. Therefore the defect-engineering strategy is applied to generate the intended defects of MOFs. Herein, an opposite way of a solvent-assisted interpenetration phenomenon of **hms** topology was used. The hms-MOFs generate defects by extraction of neutral pillaring linkers between 2D sheets under the high temperature conditions in non-coordinative solvent environment. Furthermore, it was possible to modify the amounts of defects systematically by control the heating temperature and aging time. It encourages to generate various pores; micro-, meso-, and macropores, and introduce suitable defects, depending on the aimed purpose.

In the hms-MOFs with non-coordinative solvent environment, the pillaring linker removal leads the point defect in porous networks under the thermal vacuum condition. Based on the controllability of resident linkers and maintaining crystallinity, temperature of 220 ºC was selected as an appropriate

evaporating linker temperature for both of **azo-hms** and **bpa-hms**. After removing pillaring linkers from hms-MOFs, the crystals are soaked in fresh DMF solvents to dilute resident linkers in pores of frameworks, and interpenetrate the defected samples as well. The defected crystals can interpenetrate in the same manner of interpenetration method of **azo-hms-c** and **bpa-hms-c**. The prepared crystals are **hms-d**.

The **hms-d** MOFs show interesting adsorption behaviors in N_2 sorption uptakes. Both of the **azo-hms-d** and **bpa-hms-d** are investigated, depending on the thermal aging time. In the series of **azo-hms-d**, the microporosity of **azo-hms-d** is almost maintaining and the additional porosities are generated easily. The lasting micropores indicates that the stability of azo-MOFs and it is confirmed as the PXRD patterns of **azo-hms-d**. In the case of the mesopores, two different pores are distributed around 10 Å and 35 Å. Also the macropores, which have pore width over 50 Å, are generated for heating 3 hours under the vacuum condition. Moreover, the **azo-hms-d24** has exceedingly various size pores in its MOFs structure. Meanwhile, the **bpa-hms-d3** generates mesopores with considerable micropores. As the aging time gets longer; **bpa-hms-d9** and **bpa-hms-d24**, the total amount of fragment is increased and the size of defect also increased. While the mean value of pore size distribution is not significantly affected depending on the variables of aging time. It seems to be that there is not any other defects except the empty pillaring linker place and the defects are well-dispersed in whole **bpa-MOF** structures.

The results indicate that the **hms-d** MOFs can control the amount of various pores with different size; micro-, meso-, and macropores, systematically which is called the hierarchical porous frameworks. The MOFs with hierarchical porosity are expected with potential application, such as catalysts, selective adsorbent based on their pore size selectivity, and superior transportation of molecules. Furthermore, the post-synthetic method of preparing MOFs can be investigated valuably, and it would be introduced into other MOFs to improve their properties.

V. Supporting Information

At the table of X-ray crystallographic data (Table 4-1 and Table 4-2),

[a]R = $\sum||Fo| - |Fc||/\sum|Fo|$, $P = \frac{Fo^2+2Fc^2}{3}$.

[b]$wR(F^2) = \left[\frac{\sum w(Fo^2-Fc^2)^2}{\sum w(Fo^2)^2}\right]^{\frac{1}{2}}$ $where\ w = 1/[\sigma^2(Fo^2) + (0.1653P)^2 + (7.425)P]$, $P = \frac{Fo^2+2Fc^2}{3}$

[c]$wR(F^0) = \left[\sum \frac{w(Fo^2-Fc^2)^2}{\sum w(Fo^2)^2}\right]^{\frac{1}{2}}$ $where\ w = \frac{1}{[\sigma^2(Fo^2)+(0.0728P)^2+(16.1542)P]}$, $P = (Fo^2 + 2Fc^2)$,

Surface area by the BET method

BET equation: $$v = \frac{cv_m x}{(1-x)[1+(c-1)x]}$$ eqn. 1

Where $x = P/P_0$, v is the volume of nitrogen adsorbed per gram of MOF at STP, v_m is the monolayer capacity, and c is related to the heat of adsorption. And the slope and y-intercept of the line yield c and vm. The surface area is then calculated from:

Surface area: $$A = v_m \sigma_0 N_{av}$$ eqn. 2

Where σ_0 is the cross-sectional area of nitrogen at liquid density (16.2 Å) and N_{av} is Avogadro's number.[76]

Table S1. The values resulted from virial-fitting of hms-MOFs; correlation coefficient, *c*; related to the heat adsorption, v_m; the monolayer capacity, and surface area of respective MOFs.

	Correlation coefficient	*c*	v_m (cm^3(STP) g^{-1})	Surface area (m^2 g^{-1})
azo-hms	0.9999	14804	438.87	1910.2
bpa-hms	1.0000	15509	565.40	2460.9
azo-hms-c	1.0000	5685.5	99.227	431.88
bpa-hms-c	1.0000	66240	103.22	449.28

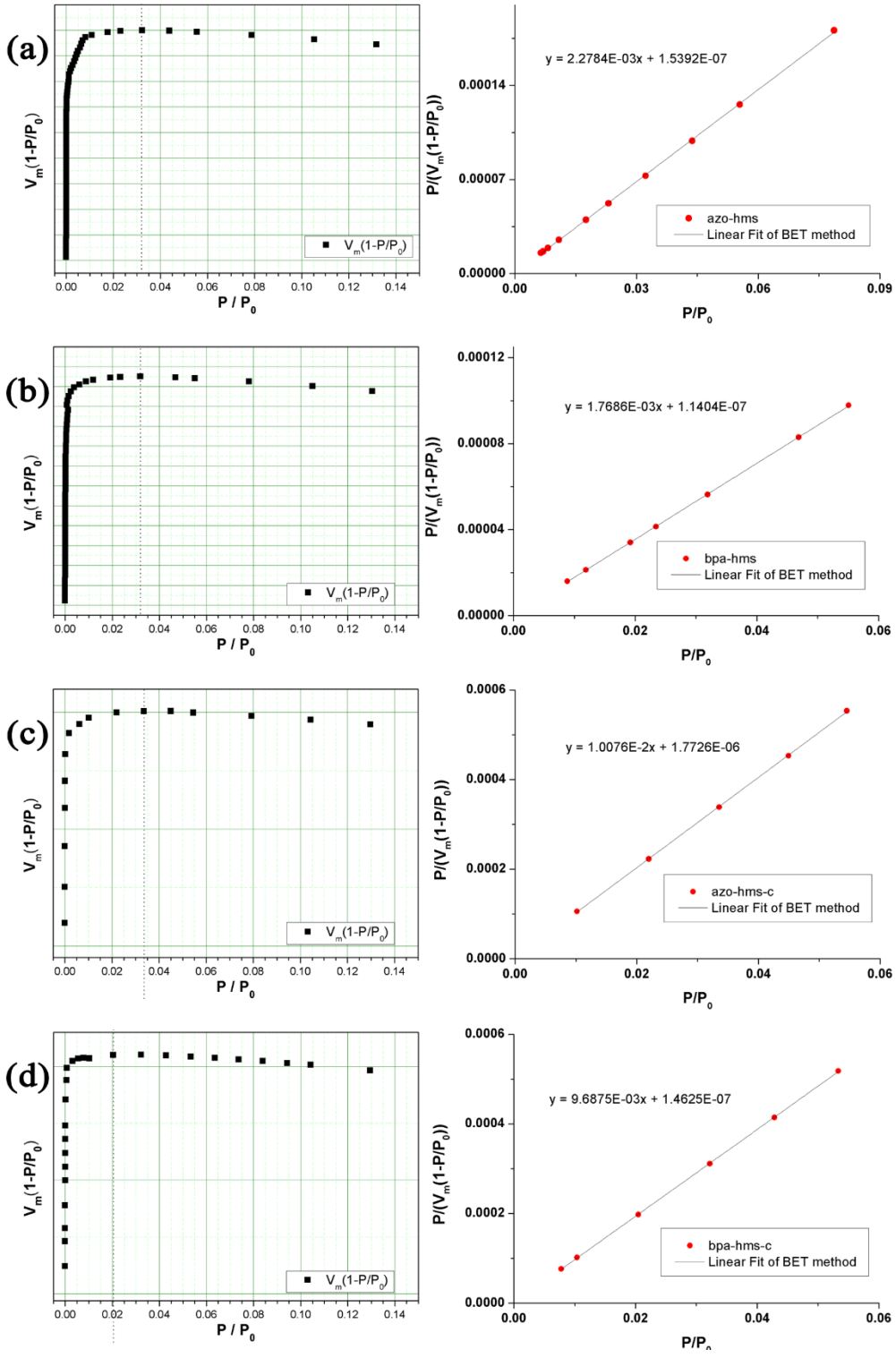

Figure S1. $V_m(P-P_0)$ vs P/P_0 for hms-MOFs. Only the range below dot point of P/P_0 in respective graphs satisfies the first consistency criterion for applying the BET theory. (Left) And the comparison of $P/(V_m(1-(P-P_0))$ calculated from the standard range, BET linear fit calculated from the range identified through the consistency criteria. (Right); (a) **azo-hms**; (b) **bpa-hms**; (c) **azo-hms-c**; (d) **bpa-hms-c**.

Calculation of isosteric heat of adsorption (Q_{st})

To extract the coverage-dependent isosteric heat of adsorption, the data were modeled with a virial-type expression composed of parameters a_i and b_i that are independent of temperature.

$$\ln P = \ln N + \frac{1}{T}\sum_{i=0}^{m} a_i N^i + \sum_{i=0}^{n} b_i N^i \qquad \text{eqn. 1}$$

Where *P* is pressure, *N* is the amount adsorbed (or uptake), *T* is temperature, and m and n determine the number of terms required to adequately describe the isotherm. From these results, the isosteric heat of adsorption is calculated according to:

$$Q_{st} = -R\sum_{i=0}^{m} a_i N^i \qquad \text{eqn. 2}$$

Where *R* is the universal gas constant. The coverage dependencies of Q_{st} calculated from the 273 K and 298 K CO_2 data are presented graphically in Figure 4-7 and Figure 4-16. Errors were propagated by taking into account the covariance of the fitting parameters.[77]

Table S2. The parameters a_i and b_i that are independent of temperature and fitting correlation between the virial-type expression of experimental CO_2 pressure in hms-MOFs at 0 ºC and 25 ºC, and corresponding virial-fitting.

	correlation	a_0	a_1	a_2	a_3	a_4	b_0
azo-hms	0.995	-15718.08	1.55954	-0.01086	5.0617E-5	-8.8826E-8	56.01962
bpa-hms	0.995	-2851.621	2.06513	-0.00648	-2.7065E-6	5.3687E-8	9.20108
azo-hms-c	0.996	-3979.114	-1.62362	0.1963	-0.00219	1.0107E-5	12.23451
bpa-hms-c	0.979	-4147.922	13.52387	-0.27219	0.00373	-1.6718E-5	12.50564

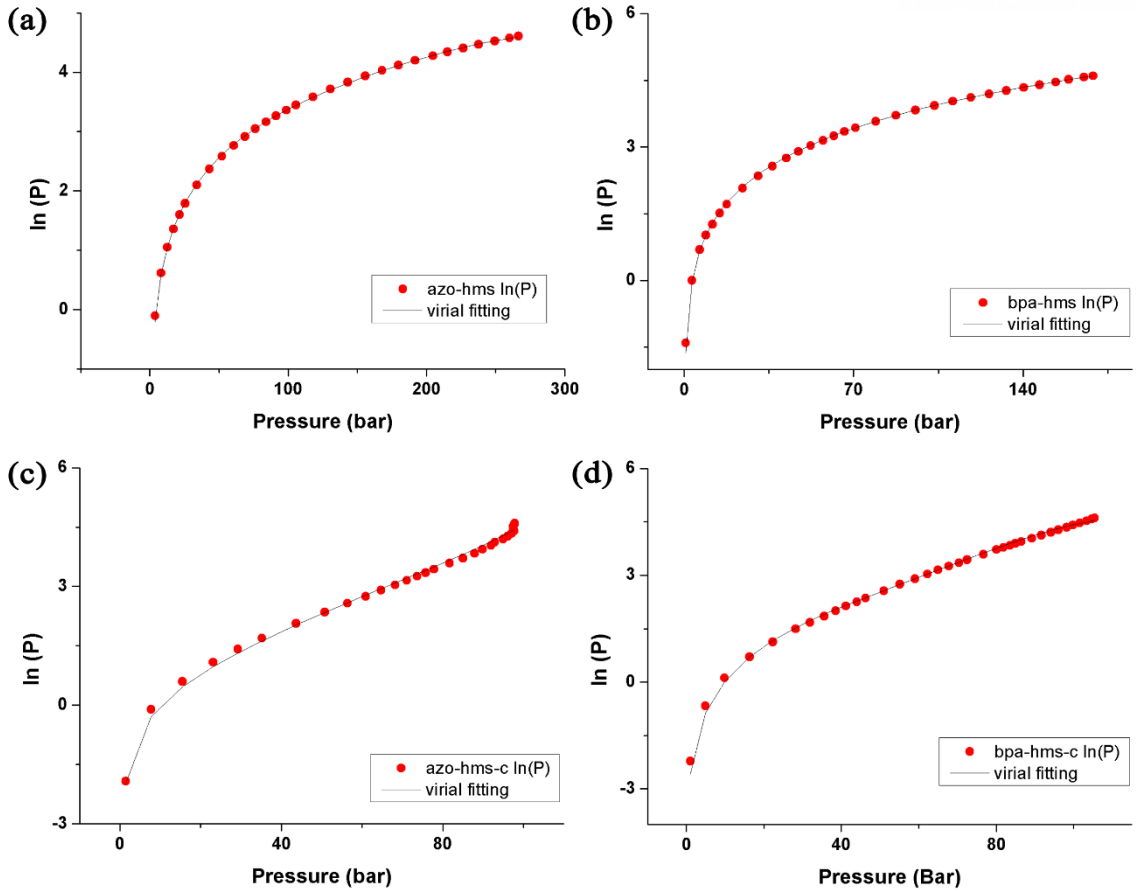

Figure S2. The virial-type expression of experimental CO_2 pressure in hms-MOFs at 0 ºC and 25 ºC, and corresponding virial fitting. (a) **azo-hms**; (b) **bpa-hms**; (c) **azo-hms-c**; (d) **bpa-hms-c**

NMR spectroscopy analysis

In the procedure of generating defects on hms-MOFs, the resident amounts of neutral pillaring linkers are determined by the integral of NMR spectroscopic analysis.

azo-hms-d

The crystals are digested in deuterium choloride (DCl) and deuterium water (D_2O) mix solution. The plot in Figure S3d demonstrates that the neutral ligand amount in the crystals is gradually decreased and saturated as increasing the aging time under the thermal vacuum condition. The peak place can be shifted depending on the feeding amount of DCl.

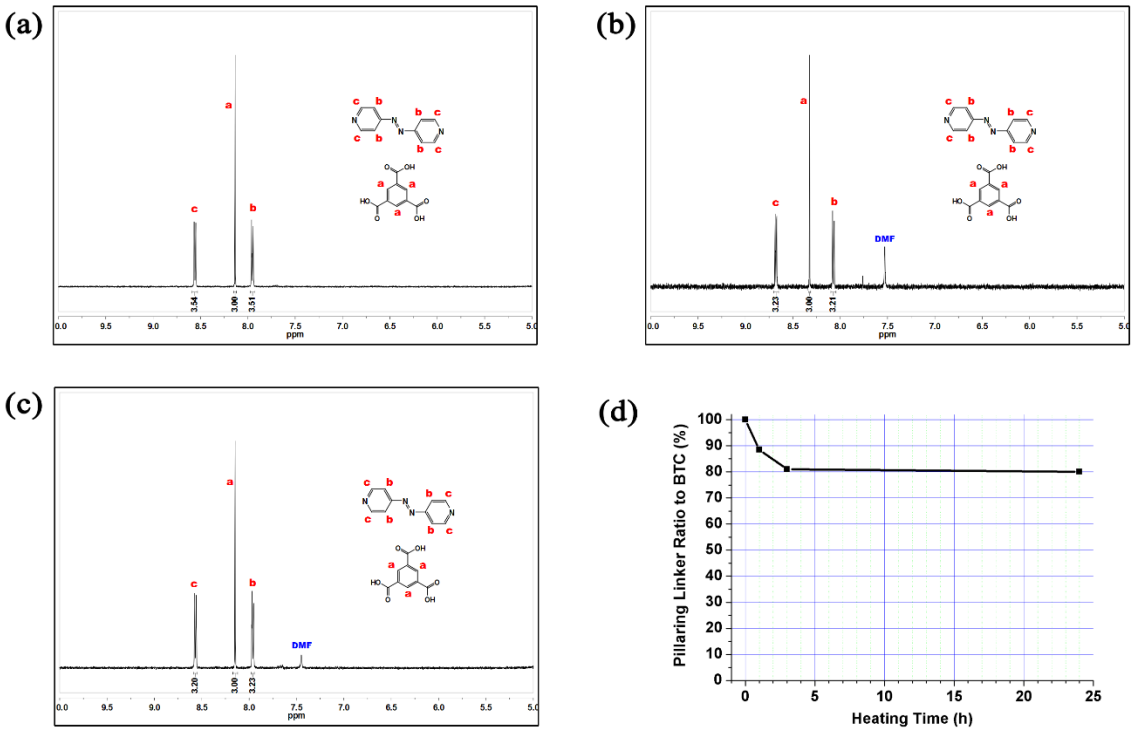

Figure S3. (a-c) ^{1}H NMR spectra of crystals digested in DCl/D_2O. The ratios of resident linker azopy and BTC in the resulting extraction of neutral linkers are determined using the integrations of the peaks; (a) **azo-hms-d1**; (b) **azo-hms-d3**; (c) **azo-hms-d24**; (d) The plot demonstrates the increasing incorporation of fragment into the crystals as aging time is increased under the thermal vacuum condition.

bpa-hms-d

The crystals are digested in DCl and dimethyl sulfoxide (DMSO-d_6) mix solution. The plot in Figure. S4f demonstrates that the neutral ligand amount in the crystals is gradually decreased as increasing the aging time under the thermal vacuum condition. The peak place can be shifted depending on the feeding amount of DCl.

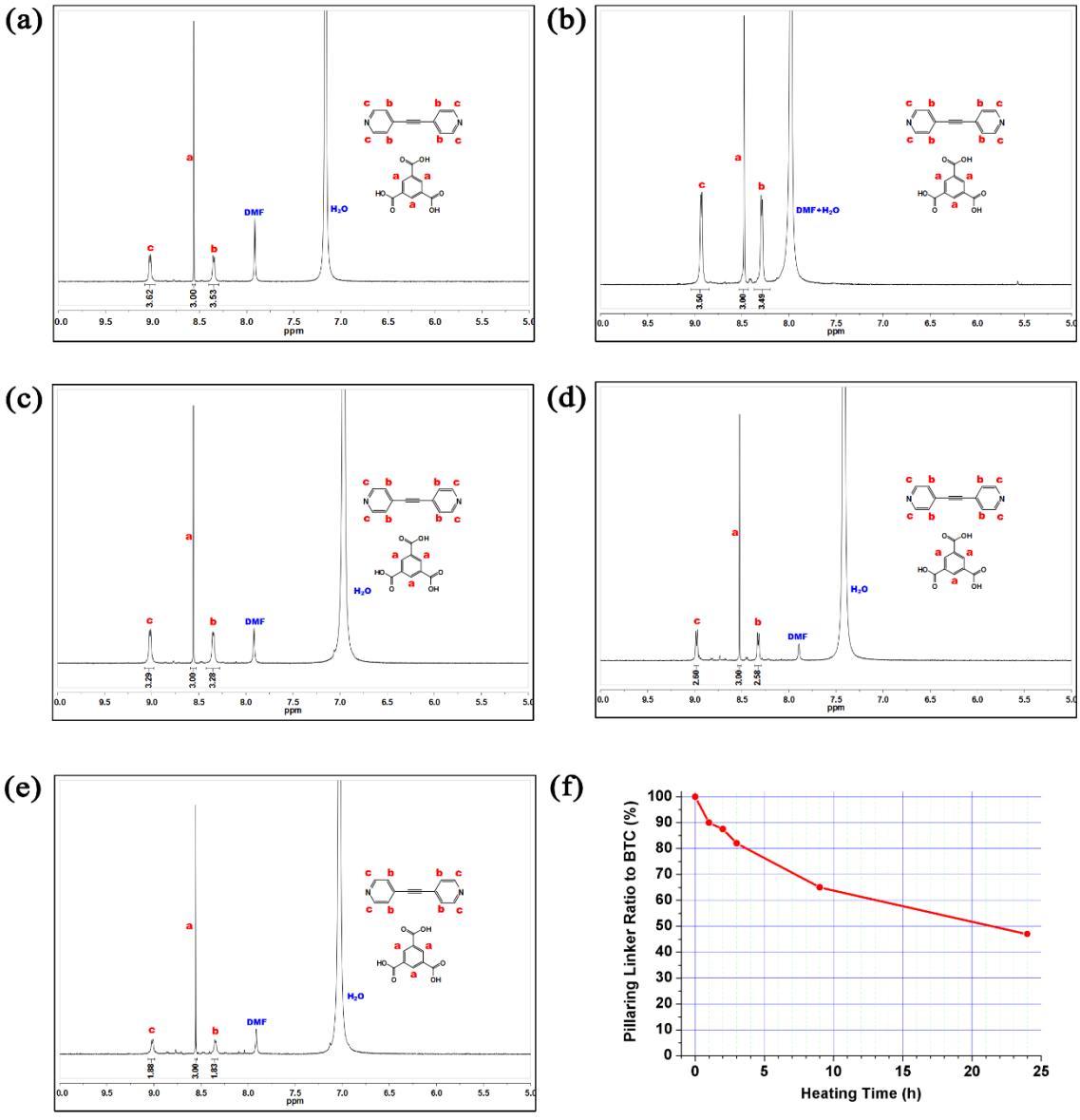

Figure S4. (a-e) ^{1}H NMR spectra of crystals digested in DCl/DMSO-d_6. The ratios of resident linker bpa and BTC in the resulting extraction of neutral linkers are determined using the integrations of the peaks; (a) **bpa-hms-d1**; (b) **bpa-hms-d2**; (c) **bpa-hms-d3**; (d) **bpa-hms-d9**; (e) **bpa-hms-d24**; (f) The plot demonstrates the increasing incorporation of fragment into the crystals as aging time is increased under the thermal vacuum condition.

NLDFT pore size distribution

This particular approach allows the calculation of theoretical adsorption-desorption isotherms in pores of given shape. Moreover, the pore size distribution (PSD) Fitting of model porous materials constituted, for instance, of cylindrical capillaries or slit-shaped pores, can be approximated from the deconvolution of the generalized adsorption equation, which assumes the experimental isotherm to be a weighted sum of the theoretical isotherms in pores of different diameters:

$$N_{exp}\left(\frac{\mathrm{p}}{\mathrm{p}^0}\right) = \int_{Dmin}^{Dmax} Ns(D,\frac{p}{p^0})\varphi_s(D)dD \qquad \text{eqn.}$$

Here, $N_{exp}(p/p^0)$ represents the experimental isotherm; $N_s(D,p/p^0)$ corresponds to individual theoretical isotherms in pores of diameter D; $\phi s(D)$ is the PSD fitting to be determined. The resolution algorithm of eqn. allows us to obtain the best sets of pore sizes of a given shape that better fits the experimental data.[78]

The NLDFT treatment, when applied to the log-normal of the experimental isotherm of MOFs with **hms** topology, is in good agreement with some other independent methods such as X-ray diffraction.

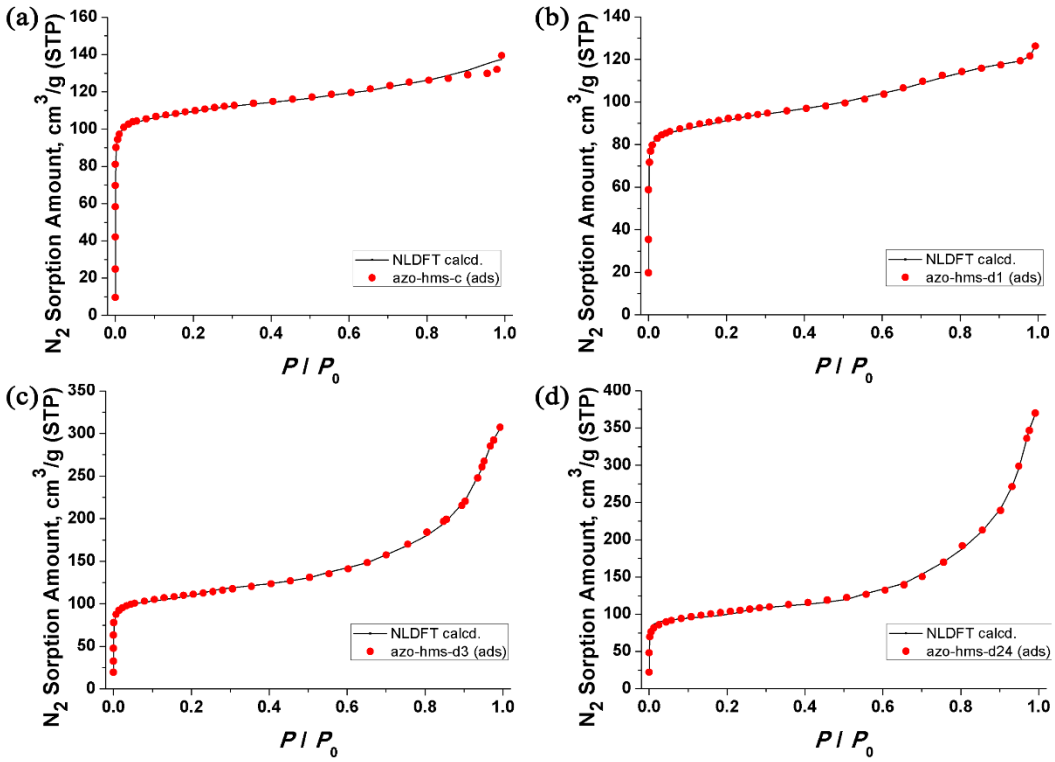

Figure S5. Experimental N_2 adsorption data in **azo-hms-d** at 77 K, and corresponding NLDFT theoretical isotherms fits in pore of different diameters depending on the aging time under the thermal vacuum condition; (a) **azo-hms-c**; (b) **azo-hms-d1**; (c) **azo-hms-d3**; (d) **azo-hms-d24**.

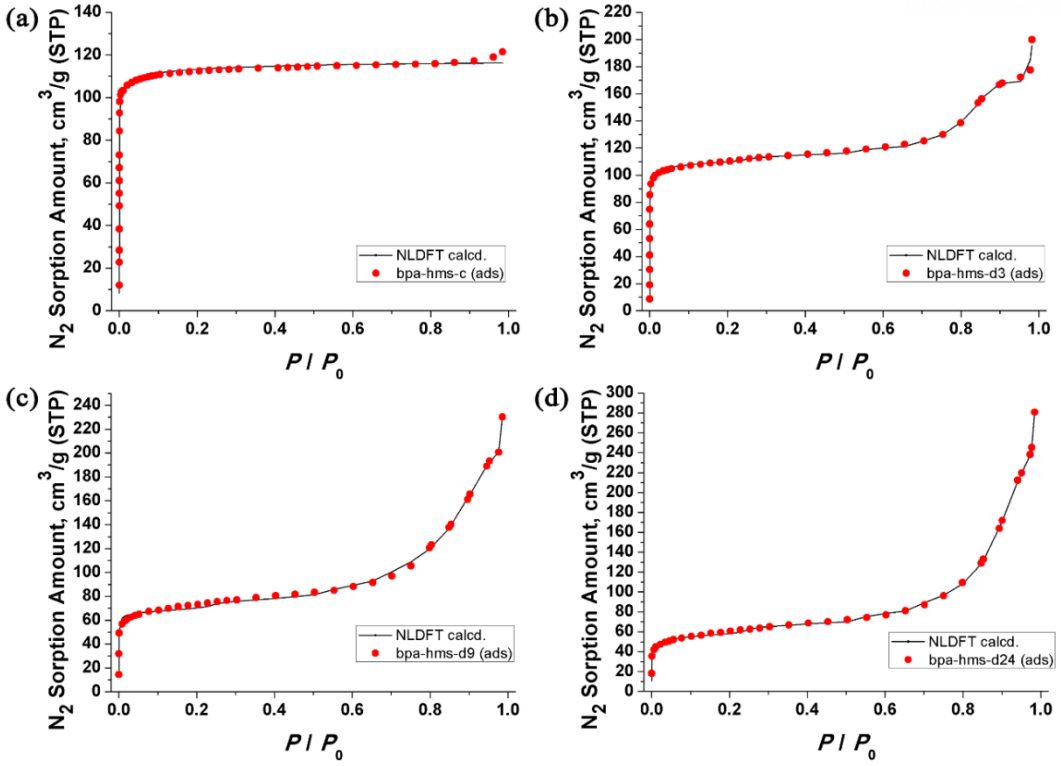

Figure S6. Experimental N_2 adsorption data in **bpa-hms-d** at 77 K, and corresponding NLDFT theoretical isotherms fits in pore of different diameters depending on the aging time under the thermal vacuum condition; (a) **bpa-hms-c**; (b) **bpa-hms-d3**; (c) **bpa-hms-d9**; (d) **bpa-hms-d24**.

REFERENCES

[1] Davis M. E., Nature, 2002, 417, 813-821.

[2] a) J. Cejka, Surface Science and Catalysis, 2005, 157, 111-134; b) A. Corma, Chem. Rev., 1997, 97, 2373; c) J.Cejka and B. Wichterlova, Catal. Rev., 2002, 44, 375; d) J., Cejka, Encyclopedia of Supramolecular Chemistry, 2004, 1623.

[3] Vijaykumar S.Marakatti, Mesoporous Materials – Synthesis and Applications, PPISR, Bangalore.

[4] Estermann, M., McCusker, L. B., Baerlocher, Ch., Merrouche, A. and Kessler, H., Nature, 1991, 352, 320-323.

[5] Davis, M. E, Saladarriaga, C., Montes, C., Graces, J. and Crowder, C. Nature, 1988, 331, 698-699.

[6] Kresge, C. T., Leonowicz, M. E., Roth, W. J., Vartuli, J. C. and Beck, J. S., Nature, 1992, 359, 710-712.

[7] a) A. Corma, Chem. Rev., 1995, 95, 559; b) C. S. Cundy, P. A. Cox, Chem. Rev., 2003, 103, 163.

[8] a) A. E. W. Beers, T. A. Nijhuis, F. Kapteijin, J. A. Moulijin, Micropor. Mesopor. Mater., 2001, 48, 279; b) Ma. A. den Hollander, M. Wissink, M. Makkee, J. A. Moulijin, Appl. Catal. A: Gen. 2002, 223, 85; c) F. Collignon, G. Poncelet, J. Catal., 2001, 202, 68; d) J. Perez-Ramirez, F. Kapteijin, G. Mul, J. A. Moulijin, Chem. Commun., 2001, 693; e) J. Perez-Ramirez, F. Kapteijin, G. Mul, J. A. Moulijin, J. Catal., 2002, 208, 211.

[9] Chester, A. W., Clement, P and Han, S., Faujasite zeolitic materials, 2000, 6, 136, 291A.

[10] a) M. Ogura, S. Y. Shinomiya, J. Tateno, Y. Nara, M. Nomura, E. Kikuchi, M. Matsukata, Appl. Catal. A: Gen, 2001, 219, 33; b) J. Perez-Ramirez, F. Kapteijin, J. C. Groen, A. Domenech, G. Mul, J. A. Moulijin, J. Catal., 2003, 214, 33; c) A. Corma, A. Martinez, V. Martinez-Soria, J. Catal., 2001, 200, 259; d) X. Zhao, G. Q. Lu, G. J. Millar, Ind. Eng. Chem. Res., 1996, 35, 2075.

[11] Hiroyasu Furukawa, Kyle E. Cordova, Michael O'Keeffe, Omar M. Yaghi, sicence, 2013, 341, 1230444.

[12] a) Li, H, Eddaoudi, M, O'Keeffe, M. and Yaghi, O. M., Nature, 1999, 276-279;b) Chen, B., Eddaoudi, M., Hyde, S. T., O'Keeffe, M and Yaghi, O. M., Science, 2001, 291, 1021-1023; c) Eddaoudi, M. *et al.* Science, 2002, 295, 469-472.

[13] a) Hong-Cai Zhou, Susumu Kitagawa, *Chem. Soc. Rev.*, **2014**, *43*, 5415-5418; b) *Chem. Rev*., **2012**, *112*, 673-674; c) Paolo Falcaro, Raffaele Ricco, C. M. Doherty, K. Liang, A. J. Hill and M. J. Styles, *Chem. Soc. Rev.*, **2014**, *43*, 5513-5560.

[14] ISI Web of Science, research performed during April 2014 using the following key words: MOFs (orange), MOFs AND (Device OR Pattern OR Positioning OR Fabrication) (blue).

[15] a) K. Sumida, D. L. Rogow, J. A. Mason, T. M. McDonald, E. D. Bloch, Z. R. Herm, T.-H. Bae and J. R. Long, *Chem. Rev*., **2012**, *112*, 724-781; b) M. P. Suh, H. J. Park, T. K. Prasad and D.-W. Lim, *Chem. Rev*., **2012**, *112*, 782-835.

[16] J.-R. Li, J. Sculley and H. –C. Zhou, *Chem. Rev*., **2012**, *112*, 869-932.

[17] M. Yoon, R. Srirambalaji and K. Kim, *Chem. Rev*., **2012**, *112*, 1196-1231.

[18] L. E. Kreno, K. Leong, O. K. Farha, M. Allendorf, R. P. Van Duyne and J. T. Hupp, *Chem. Rev*., **2012**, *112*, 1105-1125.

[19] a) C, M. Doherty, E. Knystautas, D. Buso, L. Villanova, K. Konstas, A. J. Hill, M. Takahashi and P. Falcaro, *J. Mater. Chem*., **2012**, *22*, 11470-11474; b) C. M. Doherty, G. Grenci, R. Ricco, J. I. Mardel, J. Reboul, S. Furukawa, S. Kitagawa, A. J. Hill and P. Falcaro, *Adv. Mater*., **2013**, *25*, 4701-4705; c) S.-H. Huo and X.-P. Yan, *Analyst.*, **2012**, *137*, 3445-3451.

[20] a) P. Horcajada, R. Gref, T. Baati, P. K. Allan, G. Maurin, P. Couvreur, G. Ferey, R. E. Morris and C. Serre, *Chem. Rev*., **2012**, *112*, 1232-1268; b) S. Keskin and S. Kizilel, *Ind, Eng. Chem. Res*., **2011**, *50*, 1799-1812.

[21] Weigang Lu, Zhangwen Wei, Zhi-Yuan Gu, Tian-Fu Liu, Jinhee Park, Jihye Park, Jian Tian, Muwei Zhan, Qiang Zhang, Thomas Gentle III, Mathieu Bosch and Hong-Cai Zhou, Chem. Soc. Rev., 2014, 5561-5593.

[22] B. F. Hosins and R. Robson, J. Am. Chem. Soc, 1990, 112, 1546-1554.

[23] S. S.-Y. Chui, S. M.-F. Lo, J. P. H. Charmant, A. G. orpen and I. D. Williams, Science, 1999, 283, 1148-1150.

[24] D. Feng, Z. –Y. Gu, J. –R. Li, H. –L. Jiang, Z. Wei and H. C. Zhou, Angew, Chem. Int. Ed., 2012, 51, 10307-10310.

[25] S. S. Kaye, A. Dailly, O. M. Yaghi and J. R. Long, J. Am. Chem. Soc., 2007, 129, 14176-14177.

[26] N. W. Ockwig, O. Delgado-Freidrichs, M. O'Keeffe and O. M. Yaghi, Acc. Chem. Res., 2005, 38, 176-182.

[27] A. G. Wong-Foy, A. J. Matzger and O. M. Yaghi, J. Am. Chem. Soc., 2006, 128, 3494-3495.

[28] J. J. Low, A. I. Benin, P. Jakubczak, J. F. Abrahamian, S. A. Faheem and R. R. Willies, J. Am. Chem. Soc., 2009, 131, 15834-15842.

[29] S. R. Caskey, A. G. Wong-Foy and A. J. Matzger, J. Am. Chem. Soc., 2008, 130, 10870-10871.

[30] T. M. McDonald, W. R. Lee, J. A. Mason, B. M. Wiers, C. S. Hong and J. R. Long, J. Am. Chem. Soc., 2012, 134, 7056-7065.

[31] H. Deng, S. Grunder, K. E. Cordova, C. Valente, H. Furukawa, M. Hmadeh, F. Gandara, A. C. Whalley, Z. Liu, S. Asahina, H. Kazumori, M. O'Keeffe, O. Terasaki, J. F. Stoddart and O. M. Yaghi, Science, 2012, 336, 1018-1023.

[32] J. H. Cavka, S. Jakobsen, U. Olsbye, N. Guillou, C. Lamberti, S. Bordiga and K. P. Lillerud, J. Am. Chem. Soc., 2008, 130, 13850-13851.

[33] A. Schaate, P. Roy, T. Preube, S. J. Lohmeier, A. Godt and P. Behrens, Chem. –Eur. J., 2011, 17, 9320-9325.

[34] Seth. M. Cohen, *Chem. Rev*., **2012**, *112*, 970-1000.

[35] B. Chen *et al*., J. Am. Chem. Soc., 2000, 122, 11559-11560.

[36] a) B. Chen, N. W. Ockwig, A. R. Millward, D. S. Contreras, O. M. Yaghi, Angew. Chem. Int. Ed. 2005, 44, 4745-4749; b) S. Horike, M. Dinca, K. Tamaki, J. R. Long, J. Am. Chem. Soc., 2008,

130, 5854-5855; c) D. Britt, H. Furukawa, B. Wang, T. G. Glover, O. M. Yaghi, Proc. Natl. Acad. Sci. U. S. A., 2009, 106, 20637-20640.

[37] J. S. Seo *et al*., Nature, 2000, 404, 982-986.

[38] a) Seok Jeong, *Chem. Mater*., **2013**, *25*, 1047-1054; b) Seok Jeong, D. Kim, S. Shin, D. Moon, S. J. Cho, M. S. Lah, *Chem. Mater*., **2014**, *26*, 1711-1719.

[39] Yonghwi Kim, Tao Yang, Gyeongwon Yun, Mohammad Bagher Ghasemian, Jaehyoung Koo, Eunsung Lee, Sung June Cho, and Kimoon Kim, Angew. Chem., 2015, 127, 1-7.

[40] Choi, K. M. Jeon, H. J. Kang, J. K. and Yaghi, O. M., J. Am. Chem. Soc., 2011, 133, 11920-11923.

[41] a) Chun, H. Dybtsev, D. N. Kim, H. Kim, K., Chem. Eur. J., 2005, 11, 3521; b) Kleist, W. Jutz, F. Maciejewski, M. Baiker, A., Eur. J. Inorg. Chem., 2009, 2009, 3552; c) Deng, H. Doonan, C. J. Furukawa, H. Ferreira, R. B. Towne, J. Knobler, C. B. Wang, B. Yaghi, O. M., Science 2010, 327, 846; d) Fukushima, T. Horike, S. Inubushi, Y. Nakagawa, K. Kubota, Y. Takata, M. Kitagawa, S., Angeew. Chem. Int. Ed., 2010, 49, 4820.

[42] Burrows, A. D., CrystEngComnm 2011, 13, 3623.

[43] Tao Le, Jeanne E. Sullivan, and Nathaniel L. Rosi, J. Am. Chem. Soc., 2013, 135, 9984-9987.

[44] Srinivas Gadipelli and Zhengxiao Guo, Chem. Mater., 2014, 26, 6333-6338.

[45] a) H. Kim,. M. P. Suh, Inorg. Chem., 2005, 44, 810-812; b) D. J. Tranchemontagne, J. R. Hunt, O. M. Yaghi, Tetrahedron, 2008, 64, 8553-8557; c) H. Kim, S. Das, M. G. Kim, D. N. Dybtsev, Y. Kim, K. Kim, Inorg. Chem., 2011, 50, 3691-3696; d) J. Yang, J. –F. Ma, S. R. Batten, S. W. Ng. Y. –Y. Liu, CrystEngComm., 2011, 13, 5296-5298.

[46] S. Bureekaew, H. Sato, R. Matsuda, Y. Kubota, R. Hirose, J. Kim, K. Kato, M. Takata, S. Kitagawa, Angew. Chem., 2010, 122, 7826-7830; Angew. Chem. In. Ed. 2010, 49, 7660-7664.

[47] L. Ma, W. Lin, Angew, Chem. 2009, 121, 3691-3694; Angew. Chem. Int. Ed., 2009, 48, 3637-3640.

[48] Y. Takashima, V. M. Martinz, S. Furukawa, M. Kondo, S. Shimomura, H. Uehara, M. Nakahama, K. Sugimoto, S. Kitagawa, Nat.Commun., 2011, 2, 168.

[49] T. K. Maji, R. Matsuda, S. Kitagaawa, Nat. Mater. 2007, 6, 142-148.

[50] Sang Beom Choi, Hiroyasu Furukawa, Hye Jin Nam, Duk-Young Jung, Young Ho Jhon, Allan Walton, David Book, Michael O'Keeffe, Omar M. Yaghi, and Jaheon Kim, Angew. Chem. Int. Ed., 2012, 51, 8791-8795.

[51] Megumi Mukoyoshi, Hirokazu Kobayashi, Kohei Kusada, Mikihiro Hayashi, Teppi Yamada, Mitsuhiko Maesato, Jared M. Talyor, Yoshiki Kubota, Kenichi Kato, Masaki Takata, Tomokazu Yamamoto, Syo Matsumura, and Hiroshi Kitagawa, Chem. Commun., 2015, 51, 12463-12466.

[52] a) Yang, S. J. Park, C. R., Adv. Mater., 2012, 24, 4010; b) Yang, S. J. Kim, T. Im, J. H. Kim, Y. S. Lee, K. Jung, H. Park, C. R., Chem. Mater., 2012, 24, 464.; c) Hu, J. Wang, H. Gao, Q. Guo, H. Carbon, 2010, 48, 3599; d) Chaikittisilp, W. Hu, M. Wang, H. Huang, H. –S. Fujita, T. Wu, K. C. –W. Chen, L. –C. Yamauchi, Y. Ariga, K., Chem. Commun., 2012, 48, 7259; e) Lim, S. Suh, K. Kim, Y. Yoon, M. Park, H. Dybtsev, D. N. Kim, K., Chem. Commun., 2012, 48, 7447; f) Jiang, H. –L. Liu, B. Lan, Y. –Q. Kuratani, K. Akita, T. Shioyama, H. Zong, F. Xu, Q., J. Am. Chem. Soc., 2011, 133, 11854.

[53] Tae Kyung Kim, Kyung Joo Lee, Jae Yeong Cheon, Jae Hwa Lee, Sang Hoon Joo, and Hoi Ri Moon, J. Am. Chem. Soc., 2013, 135, 8940-8946.

[54] a) Velev, O. D. Jede, T. A. Lobo, R. F. and Lenhoff, A. M., Nature, 1997, 389, 447-448; b) Stein, A., Microporous Mesoporous Mater., 2001, 44-45, 227-239.

[55] Yu Li, Zheng-Yi Fu, and Bao-Lian Su, Adv, Funct. Mater., 2012, 22, 4634-4667.

[56] Christopher M. A. Parlett, Karen, Wilson and Adam F. Lee, Chem. Soc. Rev., 2013, 42, 3876-3893.

[57] P. Yang, T. Deng, D. Zhao, P. Feng, D. Pine, B. F. Chmelka, G. M. Whitesides and G. D. Stuchky, Science, 1998, 282, 2244-2246.

[58] a) B. –L. Su, A. Leonard and Z. –Y. Yuan, C. R. Chim., 2005, 8, 713-726; b) Z. –Y. Yuan and B. –L. Su, J. Mater. Chem., 2006, 16, 663-677; c) X. Y. Yang, Y. Li, A. Lemaire, J. G. Yu and B. L. Su,. Pure Appl. Chem., 2009, 81, 2265-2307; d) C. Boissiere, D. Grosso, A. Chaumonnot, L.

Nicole and C. Sanchez, Adv. Mater., 2010, 23, 599-623; e) X. –Y. Yang, A Leonard, A. Lemaire, G. Tian and B. –L. Su, Chem. Commun., 2011, 47, 2763-2786.

[59] a) Suzuki, H. US Patent 4, 1987, 699, 892; b) Haag, W. O. and Tsikoyiann, J. G., US Patent 5, 1991, 019, 263.

[60] G. Ferey, *Chem. Mater*., **2001**, *13*, 3084.

[61] Chaoying Gao, *CrystEngComm.*, **2007**, *9*, 545-547.

[62] a) Nimmermark, A. Ohrstrom, L. Reedijk, J. Z. Kristallogr., 2013, 228, 311; b) Hu, Y. H. Zhang, L. Phys. Rev. B, 2010, 81, 174103; c) Tranchemontagne, D. J. Mendoza-Cortes, J. L. O'Keeffe, M. Yaghi, O. M., Chem. Soc. Rev., 2009 38, 1257; d) Zhou, W. Wu, H. Yildirim, T. Simpson, J. R. Walker, A. R. H. Phys. Rev. B, 2008, 78, 054114.

[63] a) Du, N. Dal-Cin, M. M. Robertson, G. P. Guiver, M. D. Macromolcules, 2012, 45, 5134; b) Kumagai, S. Grause, G. Kameda, T. Kakano, T. Horiuchi, H. Yoshioka, T. Ind. Eng. Chem. Res., 2011, 50, 1831.

[64] Feng Luo, Yun-xia Che, Ji-min Zheng, Microporous and Mesoporous Materials, 2009, 117, 486-489.

[65] J. Canivet, M. Vandichel and D. Farrusseng, Origin of highly active metal-organic framework catalysts: defects? Defects! Dalton Trans. Perspective, 2015.

[66] *Materials Studio*, version 4.3; Accelrys; San Diego, 2008.

[67] Arvai, A. J.; Nielsen, C. ADSC Quantum-210 ADX Program, Area Detector System Corporation; Poway, CA, USA, **1983**.

[68] Otwinowski, Z.; Minor, W.; in *Methods in Enzymology*, ed. Carter, Jr., C. W.; Sweet, R. M. Academic Press, New York, **1997**, vol. 276, part A, pp. 307.

[69] Rapid Auto software, R-Axis series, Cat. No. 9220B101, Rigaku Corporation.

[70] SHELX program: Sheldrick, G. M. *Acta Crystallogr. Sect. C.*, **2015**, 71, 3-8.

[71] PLATON program: A. L. Spek, *Acta Crystallogr. Sect. C.*, **2015**, 71, 9-18.

[72] a) R. Vaidhyanathan, S. S. Iremonger,G. K. H. Shimizu, P. G. Boyd, S. Alavi, T. K. Woo, *Science*, **2010**, *330*, 650; b) R. Vaidhyanathan, S. S. Iremonger, K. W. Dawson, G. K. H. Shimizu, *Chem. Commun*., **2009**, 5230.

[73] v Blatov, V. A. IUCr *CompComm. Newsletter*, **2006**, 7, 4. TOPOS is available at http://www.topos.ssu.samara.ru/.

[74] Fang, Z. J. P. Dürholt, M Kauer, W. Zhang, C. Lochenie, B. Jee, B. Albada, N. Metzler-Nolte, A. Pöppl, B. Weber, M. Muhler, Y. Wang, R. Schmid, R. A. Fischer. *J. Am. Chem. Soc*., **2014,** *136*, 9627-9636.

[75] Wu, H. Y. S. Chua, V. Krungleviciute, M. Tyagi, P. Chen, T. Yildirim, W. Zhou. *J. Am. Chem. Soc*., **2013**, *135*, 10525-10532.

[76] K. S. Walton and R. Q. Snurr. *J. Am. Chem. Soc*., **2007**, *129*, 27.

[77] J. L. C. Rowsell and O. M. Yaghi, *J. Am. Chem. Soc*., 2006, *128*, 1304-1315.

[78] M. L. Ojeda, J. M. Esparza, A. Campero, S. Cordero, I. Kornhauser, and F. Rojas, *Phys. Chem. Chem. Phys.*, **2003**, *5*, 1859-1866.

Appendix

ChemComm

COMMUNICATION

View Article Online
View Journal | View Issue

CrossMark click for updates

Cite this: *Chem. Commun.*, 2015, **51**, 3678

Received 17th December 2014,
Accepted 26th January 2015

DOI: 10.1039/c4cc10051d

www.rsc.org/chemcomm

Single crystalline hollow metal–organic frameworks: a metal–organic polyhedron single crystal as a sacrificial template†

Hyehyun Kim,[a] Minhak Oh,[a] Dongwook Kim,[a] Jeongin Park,[a] Junmo Seong,[a] Sang Kyu Kwak[b] and Myoung Soo Lah*[a]

Single crystalline hollow metal–organic frameworks (MOFs) with cavity dimensions on the order of several micrometers and hundreds of micrometers were prepared using a metal–organic polyhedron single crystal as a sacrificial hard template. The hollow nature of the MOF crystal was confirmed by scanning electron microscopy of the crystal sliced using a focused ion beam.

Hollow structures with cavities of nano-/micrometer dimensions at the center of the particles are of great importance because of their fascinating characteristics such as low density, high surface-to-volume ratio, low thermal expansion coefficient and refractive index, and high loading capacity.[1–3] So far, various fabrication methods have been developed to synthesize the hollow metal/metal oxide nano-/microstructures.[4]

Metal–organic frameworks (MOFs) have received enormous attention from researchers during the past couple of decades as a new class of porous materials, not only because of their high surface areas, but also because of their diversity and tunability.[5–7] Porous MOFs are usually crystalline materials and their pore dimensions can be modulated by the length of their organic building units.[8,9] However, it remains extremely difficult to synthesize MOFs with pore dimensions much larger than several nanometers. The largest pore dimension for MOFs reported to date is about 10 nm for IRMOF-74-XI.[10]

Several hollow MOF structures have also been prepared *via* synthetic strategies similar to those employed for the preparation of the hollow metal/metal oxide nano-/microstructures. Hollow MOF microspheres can be prepared using surface-modified polystyrene (PS) microspheres as a hard solid template,[11,12] emulsion droplets of PS membrane[13] and Tween-85[14] as soft liquid templates, and CO_2 bubbles[15] as a soft gas template. The droplets of aqueous metal solution injected into the flowing ligand-containing organic solution serve as a sacrificial template and hollow MOF capsules can be produced at the interface of the aqueous droplet and the organic solution.[16] As inorganic hollow nano-/microstructures, hollow MOF nano-/microspheres can be obtained *via* template-free approaches such as Ostwald ripening[17] and a spray-drying strategy.[18] Not all of the reported hollow MOF nano-/microstructures are single crystalline materials. The shell of the hollow MOFs is either an aggregate of smaller non-hollow MOF crystals or a composite of the polymer and the smaller non-hollow MOF crystals. Selective chemical etching of the core of a surface-protected MOF single crystal is a template-free approach to a hollow MOF structure.[19] However, the hollow MOF structure from a single crystalline MOF template is not a single crystalline hollow MOF because the shell of a hollow MOF will be significantly deteriorated during the etching process. Very recently, a hollow MOF with well-defined surface morphology was prepared using a solvothermal reaction without a template and the formation of a hollow cage was proposed through a surface-energy-driven mechanism.[20] However, the identity of the hollow MOF proposed as Fe-substituted MOF-5 is not certain. While the molar ratio of Fe to Zn in the proposed MOF is ~3.4, it is well known that the maximum molar ratio of M to Zn in M-substituted MOF-5 is ~0.33.[21]

Here, we report for the first time the preparation of single crystalline hollow MOFs with a shell pore of nanometer dimension and hollow cavity of micrometer dimension *via* a stepwise synthetic approach using a metal–organic polyhedron (MOP) single crystal as a hard sacrificial template (Scheme 1). First, we prepared cub-octahedral Cu–MOP single crystals with dimensions of either several micrometers or several hundred micrometers made of approximately 3 nm MOP building units, $[Cu_{24}(hip)_{24}S_{24}]$ (where hip = 5-hydroxyisophthalate). Single MOP crystals were used as hard sacrificial templates. The cuboctahedral Cu–MOP building units of the MOP single crystal as one type of reactant could be interlinked

[a] *Department of Chemistry, Ulsan National Institute of Science and Technology, Ulsan, 689-798, Korea. E-mail: mslah@unist.ac.kr; Fax: +82 52 217 2019; Tel: +82 52 217 2931*

[b] *Department of Chemical Engineering, Ulsan National Institute of Science and Technology, Ulsan, 689-798, Korea*

† Electronic supplementary information (ESI) available: Preparation of MOP and MOFs; CIF file and crystallographic data of **MOP-macro**; PXRD patterns of MOP and MOFs; ^{1}H NMR spectra of **MOP-macro**; SEM and FIB-SEM images of MOP and MOFs. CCDC 985419. For ESI and crystallographic data in CIF or other electronic format see DOI: 10.1039/c4cc10051d

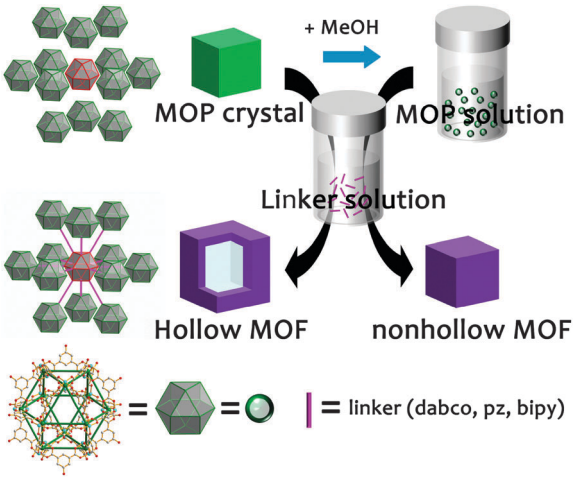

Scheme 1 A MOP single crystal as a sacrificial template for a hollow MOF single crystal.

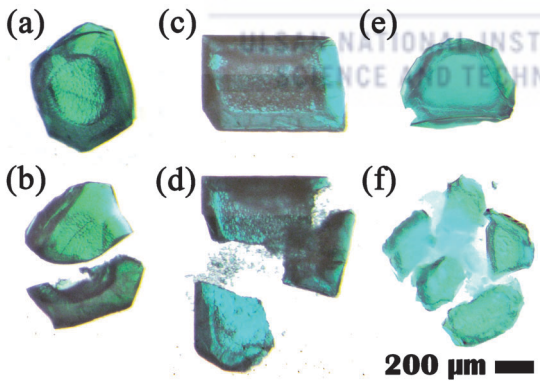

Fig. 1 Optical photomicrographs of **1-macro-h**, **2-macro-h**, **3-macro-h** crystals. (a) A **1-macro-h** crystal and (b) the **1-macro-h** crystal fragmented in two with one piece showing the inner cavity in side view. (c) A **2-macro-h** crystal and (d) the **2-macro-h** crystal fragmented in three in MeOH. (e) A **3-macro-h** crystal and (f) the **3-macro-h** crystal fragmented into several pieces in MeOH.

using linear ditopic linkers (1,4-diazabicyclo[2.2.2]octane (dabco), pyrazine (pz), and 4,4′-bipyridine (bipy)) as another type of reactant.

The cuboctahedral Cu–MOP crystals, **MOP-micro** and **MOP-macro**, are obtained from the reactions of Cu(II) ions with H_2hip as a bent ditopic dicarboxylate ligand in DMF (Fig. S1–S5, ESI†). While a solvothermal reaction without stirring resulted in single crystals of several hundred micrometers of **MOP-macro**, a similar reaction at ambient temperature with stirring produced single crystals of **MOP-micro** with dimensions of several micrometers.

Single crystalline hollow MOFs of several hundred micrometer dimensions could be prepared by reacting **MOP-macro** crystals of several hundred micrometer dimensions with ditopic linkers in MeOH, where the **MOP-macro** crystal serves as a sacrificial template. The MOP crystal serves both as a crystalline template and as a reactant for the hollow MOF crystal. The addition of the ditopic linker in MeOH into single crystals of **MOP-macro** produced corresponding hollow single crystals of a $[Cu_{24}(hip)_{24}L_6(H_2O)_{12}]$ formula unit (where L = dabco (**1-macro-h**), pz (**2-macro-h**), and bipy (**3-macro-h**)) (Fig. S6 and S7, ESI†).

Optical photomicrographs of the MOF crystals produced from **MOP-macro** crystal both as a reactant and as a crystalline template indicate that all the MOF crystals are hollow (Fig. 1). When a **1-macro-h** crystal produced from a **MOP-macro** crystal in a MeOH solution of dabco was fragmented, the inner surface of the hollow crystal was exposed in the fragments (Fig. 1a and b).

When hollow crystals of **2-macro-h** and **3-macro-h** in MeOH solutions of pz and bipy, respectively, were fragmented, the release of small crystalline/fine particles encapsulated in the cavity of the hollow crystals was observed (Fig. 1d and f). The encapsulation of the crystalline/fine particles in the inner cavity of the hollow crystal indicates that the size of the particles is larger than the portal dimensions of the corresponding shell MOFs. The particles in the inner cavity are not **MOP-macro** crystals, which are soluble in MeOH, but are probably MOF crystals, which are not soluble in MeOH.

The crystal produced in the process of the transformation from a single crystal of **MOP-macro** to a hollowed single crystal of **1-macro-h** shows that the MOP-to-MOF transformation occurs from the surface to the core of the crystal. The transformation intermediate of a single crystal of **MOP-macro** changes color from cyan to green and from the surface of the crystal to the core while maintaining the core of the crystal as cyan (Fig. 2). In addition, a reactive interface is generated between the shell of the crystalline MOF and the core of the crystalline MOP. While the crystalline MOP core in the fragmented intermediate is immediately dissolved in MeOH (Fig. 2c), the components at the shell interface become small crystalline particles in DMF (Fig. 2d).

A series of isoreticular MOFs of micrometer dimensions, $[Cu_{24}(hip)_{24}L_6(H_2O)_{12}]$ (where L = dabco (**1-micro**), pz (**2-micro**), and bipy (**3-micro**)), with solvent cavities of nanometer dimensions could be prepared *via* stepwise reactions in MeOH using **MOP-macro** as a cuboctahedral MOP precursor (Fig. 3 and Fig. S8, ESI†). The addition of a dabco linker to a MeOH solution of cuboctahedral MOP precursor immediately produced a crystalline powder of **1-micro**. The PXRD pattern of **1-micro** is very similar to that of the reported $[Zn_{24}(mip)_{24}(dabco)_6(H_2O)_{12}]$ MOF (where mip = 5-methylisophthalate) of **ubt** topology (Fig. 3).[22] Similar reactions using pz and bipy, respectively, as linkers between the MOP building blocks also produced corresponding isoreticular MOFs of the same **ubt** topology. The PXRD pattern of **2-micro** with pz as a linker is very similar to that of the reported MOF, $[Zn_{24}(mip)_{24}(dabco)_6(H_2O)_{12}]$, because the linker dimension of pz in **2-micro** is almost the same as

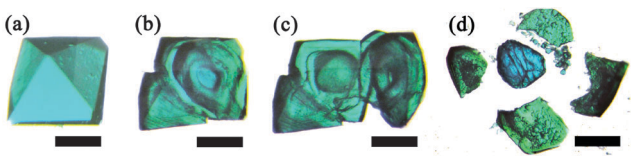

Fig. 2 The optical photomicrographs of a **MOP-macro** crystal and its intermediate in a transformation process to the **1-macro-h** crystal ((a)–(c) scale bar 200 μm, (d) scale bar 500 μm). (a) A **MOP-macro** crystal in DMF, (b) its intermediate, the **MOP-macro** crystal soaked for 20 s in a MeOH solution of dabco, (c) fragments of the intermediate crystal in MeOH, and (d) fragments of another intermediate crystal in DMF.

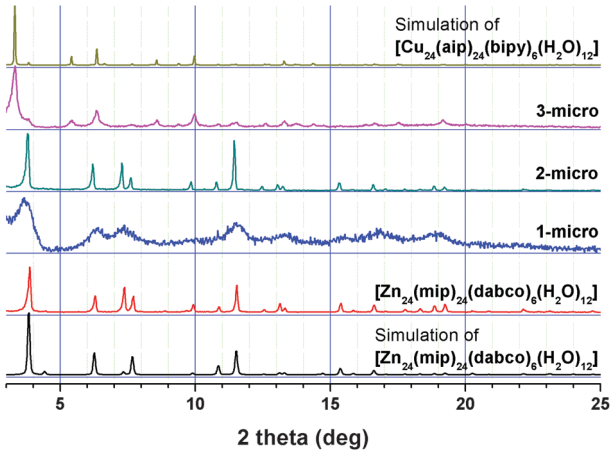

Fig. 3 Comparison of the PXRD patterns of **1-micro**, **2-micro** and **3-micro** with those of $[Zn_{24}(mip)_{24}(dabco)_6(H_2O)_{12}]$[22] and $[Cu_{24}(aip)_{24}(bipy)_6(H_2O)_{12}]$.[23]

that of dabco in $[Zn_{24}(mip)_{24}(dabco)_6(H_2O)_{12}]$ (Fig. 3), and the same MOPs in the two MOFs are interconnected *via* similar lengths of linkers in the same fashion. The strongest reflection peak at about 3.8° in the PXRD pattern of $[Zn_{24}(mip)_{24}(dabco)_6(H_2O)_{12}]$ is shifted to about 3.3° for **3-micro**, which indicates an increase of the unit cell dimension with the longer bipy linker between the MOP building blocks (Fig. 3). The PXRD pattern of **3-micro** matches well with that of the reported $[Cu_{24}(aip)_{24}(bipy)_6(H_2O)_{12}]$ (where aip = 5-aminoisophthalate) of the same **ubt** topology with the same bipy linker.[23]

Hollow single crystalline MOFs of micrometer dimensions could be prepared by reacting **MOP-micro** crystals of micrometer dimensions with ditopic linkers in MeOH (Fig. S9, ESI†). Quick addition of a MeOH solution of dabco to **MOP-micro** crystals wet with a trace amount of DMF produced micro-sized hollow MOF crystals, **1-micro-h** (Fig. S10, ESI†). The shell of a hollow MOF is not an aggregate of small non-hollow single crystals, but is a single crystalline MOF. SEM images of the hollow **1-micro-h** crystals show that most have the appearance of ordinary non-hollow crystals (Fig. S10c and d, ESI†) while some have holes at their surface (Fig. S11b, ESI†). By contrast, more fragmented hollow MOFs are observed in hollow **2-micro-h** crystals (Fig. S10e and S11c, ESI†). The inner surface of the fragmented hollow MOF is rougher than the outer surface. While the outer surface is part of the single crystalline MOF, the inner surface appears to be an aggregate of the smaller crystalline particles. Most hollow **3-micro-h** crystals also have the appearance of ordinary non-hollow crystals (Fig. S10g and h, ESI†), while a few have holes at their surface (Fig. S11d, ESI†). The crystals have octahedral morphology and have smooth and clean outer surfaces. The **3-micro-h** crystals are quite rigid. Even after sonication, most **3-micro-h** crystals maintain their morphology and have clean outer surfaces (Fig. S12, ESI†). The shell of the hollow **3-micro-h** is not an aggregate of smaller crystalline particles, but is a single crystalline particle. Sonication of hollow **3-micro-h** single crystals produced more fragmented hollow crystals and showed some interesting characteristics of the hollow MOFs, such as roughness of their inner surface and the approximate thickness of the fragmented shell MOF crystals (Fig. S12c, ESI†).

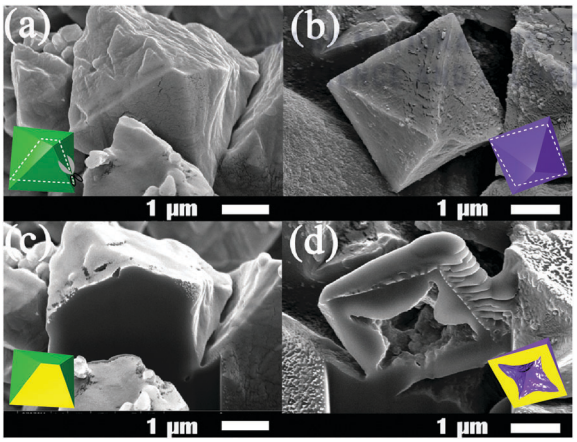

Fig. 4 SEM images of (a) a nonhollow **MOP-micro** crystal and (b) a hollow **3-micro-h** MOF crystal obtained from nonhollow **MOP-micro** crystal. FIB-SEM images of (c) the **MOP-micro** crystal sliced by using FIB milling and (d) the **3-micro-h** crystal sliced by using FIB milling after carbon coating.

The hollow nature of the micro-h crystals was confirmed by using focused ion beam-scanning electron microscopy (FIB-SEM) (Fig. 4 and Fig. S13, ESI†). To see the inner cavity of a hollow MOF crystal, the crystal was sliced using Ga ion milling. In contrast to the FIB-SEM image of the sliced non-hollow **MOP-micro** crystal (Fig. 4c), that of the sliced hollow **3-micro-h** MOF crystal (Fig. 4d) clearly shows its inner cavity and confirms the hollow nature of the seemingly non-hollow-like MOF crystal.

The total volume of the **3-micro-h** product is much larger than that of the starting **MOP-micro** reactant (Fig. 5). The volume increase in the **3-micro-h** crystals is not only the result of expansion of the unit cell volume of the **3-micro** crystal compared with that of the **MOP-micro** crystals, but is also because of the formation of a hollowed cavity of micrometer dimensions (Fig. 5).

Unlike other approaches for hollow MOFs, single crystalline hollow MOFs could be obtained by using a MOP single crystal as a sacrificial template. The MOP crystal serves not only as a hard template, but also as a reactant for single crystalline hollow MOFs (Scheme 2). At the initial stage, the MOP building units weakly interacting with each other at the surface of a MOP crystal diffuse outward into the methanol solution containing ditopic linkers and generate a reactive interface containing both the MOP building units and the ditopic linkers. The reaction at the

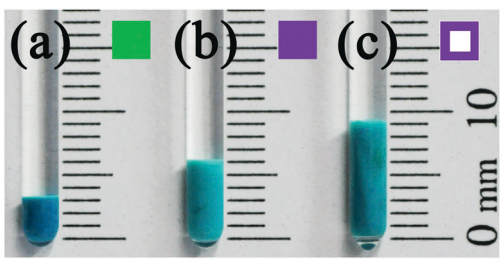

Fig. 5 (a) The volume of **MOP-micro** crystals, (b) the volume of the **3-micro** crystals obtained from the **MOP-micro** crystals, and (c) the corresponding volume of the **3-micro-h** crystals obtained from the same amount of the **MOP-micro** crystals.

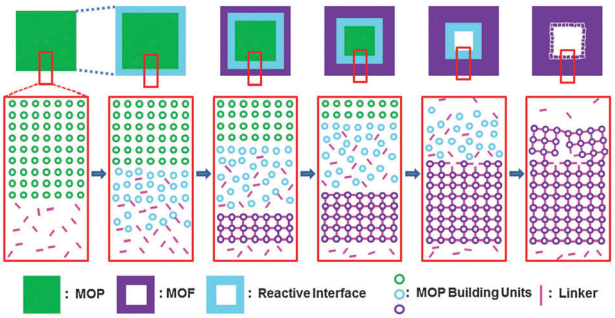

Scheme 2 The proposed formation mechanism for a single crystalline hollow MOF using a MOP single crystal as a sacrificial hard template.

reactive interface generates a thin crystalline microporous MOF shell, which accompanies the expansion of the overall dimension of the crystal and the subsequent formation of a new reactive interface. Because the small ditopic linkers in the MeOH solvent can still interpenetrate the microporous shell of the crystalline MOF, a new reactive interface with loosely bound MOP building units and the ditopic linkers can be generated between the crystalline MOF shell and the crystalline MOP core.

The microporosity of the crystalline MOF shell results in a difference in the diffusion rates of the ditopic linkers and the MOP building units. While the ditopic linkers are sufficiently small enough to diffuse into the crystal through the microporous crystalline MOF shell, the MOP building units are too large to diffuse out of the crystal through the microporous crystalline MOF shell. Consequently, the growth of the crystalline MOF shell only proceeds inward with the progressive movement of the reactive interface from the surface to the core of the crystal. As the formation of the crystalline MOF shell proceeds, the thickness of the MOF shell increases and the size of the crystalline MOP decreases. When all the MOP units at the core of the crystal are expended, single crystalline hollow MOFs with hollow cavity dimensions of several micrometers and several hundred micrometers are generated depending on the size of the MOP single crystals. The formation of the hollow structure and its dimensions are dependent on several factors such as the size of the MOP single crystal, the kind of ditopic linker and its concentration, and the solvent employed. Those factors also affect the formation of small microcrystals with varying dimensions at the microscopic/macroscopic pore of the single crystalline hollow MOF.

In summary, single crystalline hollow MOF structures were obtained by using a MOP single crystal as a sacrificial hard template. The formation of the microporous MOF shell in the hollow MOF occurs *via* the diffusion of the cuboctahedral Cu–MOP building units at the surface of the templating MOP single crystal outward to the MeOH solution containing the linker. While cuboctahedral Cu–MOP building units larger than the pore dimensions of the microporous MOF shell could not diffuse outward through the micropores of the MOF shell from the sacrificial MOP single crystal, linkers smaller than the pore dimension can diffuse inward through the micropores of the MOF shell to the cuboctahedral Cu–MOP building unit, which leads to the formation of the crystalline hollow MOFs. The dimensions of the hollow MOFs can be controlled by the dimensions of the sacrificial MOP single crystals. Not only hollow MOFs of the order of hundred micrometer dimensions, but also those of the order of micrometer dimensions could be obtained.

This work was supported by NRF-2010-0019408 and NRF-2012R1A2A2A01003077 through the National Research Foundation of Korea. The authors acknowledge PAL for beam line use (2013-3rd-2D-006).

Notes and references

1 M. Chen, C. Ye, S. Zhou and L. Wu, *Adv. Mater.*, 2013, **25**, 5343.
2 Z. Wang, L. Zhou and X. W. Lou, *Adv. Mater.*, 2012, **24**, 1903.
3 X. Lai, J. E. Halpert and D. Wang, *Energy Environ. Sci.*, 2012, **5**, 5604.
4 X. W. Lou, L. A. Archer and Z. Yang, *Adv. Mater.*, 2008, **20**, 3987.
5 H. Furukawa, K. E. Cordova, M. O'Keeffe and O. M. Yaghi, *Science*, 2013, **341**, 1230444.
6 H. C. Zhou, J. R. Long and O. M. Yaghi, *Chem. Rev.*, 2012, **112**, 673.
7 J. R. Long and O. M. Yaghi, *Chem. Soc. Rev.*, 2009, **38**, 1213.
8 M. Eddaoudi, J. Kim, N. Rosi, D. Vodak, J. Wachter, M. O'Keeffe and O. M. Yaghi, *Science*, 2002, **295**, 469.
9 D. Yuan, D. Zhao, D. Sun and H. C. Zhou, *Angew. Chem., Int. Ed.*, 2010, **49**, 5357.
10 H. Deng, S. Grunder, K. E. Cordoba, C. Valente, H. Furukawa, M. Hmadeh, F. Gándara, A. C. Whalley, Z. Liu, S. Asahina, H. Kazumori, M. O'Keeffe, O. Terasaki, J. F. Stoddart and O. M. Yaghi, *Science*, 2012, **336**, 1018.
11 H. J. Lee, W. Cho and M. Oh, *Chem. Commun.*, 2012, **48**, 221.
12 A. L. Li, F. Ke, L. G. Qiu, X. Jiang, Y. M. Wang and X. Y. Tian, *CrystEngComm*, 2013, **15**, 3554.
13 J. Huo, M. Marcello, A. Garai and D. Bradshaw, *Adv. Mater.*, 2013, **25**, 2717.
14 M. Pang, A. J. Cairns, Y. Liu, Y. Belmabkhout, H. C. Zeng and M. Eddaoudi, *J. Am. Chem. Soc.*, 2013, **135**, 10234.
15 L. Peng, J. Zhang, J. Li, B. Han, Z. Xue, B. Zhang, J. Shi and G. Yang, *J. Colloid Interface Sci.*, 2014, **416**, 198.
16 R. Ameloot, F. Vermoortele, W. Vanhove, M. B. J. Roeffaers, B. F. Sels and D. E. De Vos, *Nat. Chem.*, 2011, **3**, 382.
17 J. Huo, L. Wang, E. Irran, H. Yu, J. Gao, D. Fan, B. Li, J. Wang, W. Ding, A. M. Amin, C. Li and L. Ma, *Angew. Chem., Int. Ed.*, 2010, **49**, 9237.
18 A. Carné-Sánchez, I. Imaz, M. Cano-Sarabia and D. Maspoch, *Nat. Chem.*, 2013, **5**, 203.
19 M. Hu, S. Furukawa, R. Ohtani, H. Sukegawa, Y. Nemoto, J. Reboul, S. Kitagawa and Y. Yamauchi, *Angew. Chem., Int. Ed.*, 2012, **51**, 984.
20 Z. Zhang, Y. Chen, X. Xu, J. Zhang, G. Xiang, W. He and X. Wang, *Angew. Chem., Int. Ed.*, 2014, **53**, 429.
21 C. K. Brozek and M. Dincă, *J. Am. Chem. Soc.*, 2013, **135**, 12886.
22 H. Chun, *J. Am. Chem. Soc.*, 2008, **130**, 800.
23 H. N. Wang, X. Meng, G. S. Yang, X. L. Wang, K. Z. Shao, Z. M. Su and C. G. Wang, *Chem. Commun.*, 2011, **47**, 7128.